Investigation of Physical and Chemical Effects in Sonicated Small Flow Channels

Dissertation
for the award of the degree
"Doctor rerum naturalium" (Dr.rer.nat.)
of the Georg-August-Universität Göttingen

within the doctoral program Physik
of the Georg-August University School of Science (GAUSS)

submitted by
Ekim Sarac
from Ankara, Turkey

Göttingen, 2023

Thesis Committee:

Prof. Dr. Jörg Enderlein, *Drittes Physikalisches Institut, Universität Göttingen*
Dr. Robert Mettin, *Drittes Physikalisches Institut, Universität Göttingen*
Prof. Dr. Ulrich Parlitz, *Max Planck Institute for Dynamics and Self-Organization Göttingen*

Members of the Examination Board:

Reviewers:

Prof. Dr. Jörg Enderlein, *Drittes Physikalisches Institut, Universität Göttingen*
Prof. Dr. Ulrich Parlitz, *Max Planck Institute for Dynamics and Self-Organization Göttingen*

Further members of the Examination Board:

Dr. Robert Mettin, *Drittes Physikalisches Institut, Universität Göttingen*
Prof. Dr. Martin Rein, *Institut für Aeordynamik und Strömungstechnik (IAS), Deutsches Zentrum für Luft- und Raumfahrt e.V. (DLR) Göttingen*
Prof. Dr. Wolfram Kollatschny, *Institut für Astrophysik, Universität Göttingen*
Prof. Dr. Florentin Wörgöter, *Drittes Physikalisches Institut, Universität Göttingen*

Date of the oral examination: 20.07.2023

Contents

Abstract **1**

1 Introduction **3**

2 Theory **7**

2.1 Acoustic cavitation 8

2.1.1 Bubble dynamics 10

2.1.2 Bubble oscillations 11

2.1.3 Collapse of a spherical bubble 12

2.1.4 Bubble nucleation 17

2.1.5 The Blake threshold 17

2.1.6 Bjerknes forces 20

2.2 Sonochemistry 24

2.2.1 Sonoluminescence 26

2.2.1.1 Theories of sonoluminescence 27

2.2.1.2 Single and multibubble sonoluminescence 30

2.2.1.3 Sonochemiluminescence 31

2.3 Ultrasonic reactors 32

2.3.1 Batch type 32

2.3.2 Contiuous (Flow) ultrasonic reactors 36

2.3.2.1 Continuous reactors with emitting walls 36

2.3.2.2 Continuous reactors equipped with sonotrodes 37

2.3.2.3 Continuous ultrasonic microreactors 37

2.3.2.4 Fundamentals of Laminar Flow 40

2.3.2.5 Effect of cavitation on continuous microreactors 44

3 Materials and Methods **47**

3.1 Experimental Setups 47

3.1.1 Channels on top of transducer 47

3.1.2 Submerged flow channels 48

3.1.2.1 Submerged loop tubes . . . 48
3.1.2.2 Submerged stacked tubes . . . 50
3.2 Sonochemiluminescence measurements . . . 51
3.2.1 Preparation of the luminol solution . . . 51
3.2.2 Enhancement of luminescence intensity . . . 52

4 Results **55**
4.1 Channels on top of transducer . . . 55
4.2 Channels in bath reactor . . . 59
4.2.1 Sonicated submerged flow tubes . . . 59
4.2.1.1 Sound field inside an ultrasonic bath . . . 60
4.2.1.2 Sonochemiluminescence from channels . . . 64
4.2.1.3 Bubble structures . . . 65
4.2.1.4 Bubble dynamics reconstruction . . . 67
4.2.2 Sonicated stacked flow tubes . . . 69
4.2.2.1 Sound field inside an ultrasonic bath . . . 69
4.2.2.2 Sonochemiluminescence from an ultrasonic bath . . . 71
4.2.2.3 Sonochemiluminescence from stacked channels . . . 77
4.2.2.4 Phase shift between bubbles oscillating inside channels and an ultrasonic bath . . . 82
4.2.2.5 Bubble structures inside flow tubes . . . 90
4.2.2.6 Bubble nucleation and two phase boundary . . . 95

5 Conclusion **101**

Bibliography **105**

List of Figures **119**

Acknowledgements **129**

I'm forever blowing bubbles,
Pretty bubbles in the air,
They fly so high,
Nearly reach the sky,
Then like my dreams,
They fade and die.
Fortune's always hiding,
I've looked everywhere,
I'm forever blowing bubbles,
Pretty bubbles in the air.

Kendis, Brockman & Vincent, 1918

Abstract

In the framework of intensification of chemical processes, miniature continuous flow reactors have come into focus in recent time. As a specific way of "non-classical" energy supply to the liquid in such a flow reactor, an intense ultrasonic field can be employed to enable sonochemistry. This type of chemistry is typically mediated by cavitation bubbles which emerge in the strong sound field, and which can trigger chemical reactions during their collapse. The present work investigates ultrasonic cavitation conditions in small flow channels to gain a better understanding of the physical background of sonicated flow reactors. In prototypical experimental setups with sub-millimeter diameter flow tubes submerged in an ultrasonic bath, cavitation inception, cavitation bubble structures, and bubble dynamics are studied. The methods comprise high-speed imaging, acoustic pressure mappings, and sono-chemiluminescence measurements. Additionally, sound fields and bubble oscillations are partly simulated numerically. The main results show that a sonicated small diameter flow tube differs in several aspects from a larger volume of liquid that is exposed to ultrasound. This concerns bubble nucleation, bubble dynamics, and bubble activity. For nucleation to take place at all, usually gas slugs have to be introduced to form a Taylor flow, which leads to bubble nuclei being entrained into the liquid via the acoustically agitated interface between gas and liquid slugs. Cavitation bubbles in the tube appear in several typical structures, like streamers, clusters, and "plugs" that develop a peculiar sharp boundary of regions populated with cavitation bubbles. The bubbles in the channel are observed to show a modified oscillation behavior as compared to the unbound liquid. In particular, a certain phase shift appears, i.e., bubble expansion starts earlier, and maximum expansion can be restricted. Chemical activity of bubbles in the tubes can emerge in zones of high acoustic pressure, while in batch reactors, high pressure zones might be void of active bubbles which are driven away by acoustic forces. Taking into account these findings, sonicated submerged channels can be employed successfully for intensified sonochemical processing in miniature flow reactors.

Chapter 1

Introduction

Continuous reactors, also known as flow reactors, are utilized in *process intensification (PI)* which has been an innovative technology in fine-chemicals and pharmaceutical industries in the last decades. PI aims to increase the product quality, lower the waste and energy consumption, increase the efficient use of raw materials and improve control over the process [1]. As long as the chemical reaction conditions allow, using continuous reactors are very advantageous over their batch counterparts. *Sonication* as an additional means of PI by delivery of "nonclassical" energy via ultrasound to the liquid has emerged more recently in an attempt to combine flow reactors with *sonochemistry*. Sonochemistry is the influence, control, or enhancement of chemical reactions in the liquid phase by application of ultrasound. It turned out that in nearly all sonochemical processing, a crucial aspect for its functionality is *acoustic cavitation*, i.e. the emergence of bubbles and their oscillation dynamics due to the high acoustic field intensity. In the meantime, there are various flow reactor designs equipped with ultrasonic transducers, depending on the feasibility of the processing. However, many factors of sonicated flow reactors are not fully understood yet, which impedes efficiency, optimisation, and upscaling. The present thesis studies several aspects of ultrasound delivery towards and acoustic cavitation inside small channels or tubes, also known as milli-flow-reactors.

The 18^{th} century often refers to *The Industrial Revolution*, since the developments in science and technology had changed the agrarian economy to the one that is industrial and machine dominated, particularly in Europe and North America. During that period, a huge transformation took place from agrarian and rural societies into urban and industrial ones. This transformation has consequently led to increase in demand for goods as the increment in population from 50 to 100 % in Europe. Moreover, wealth has become widespread which has resulted in improvement in life standard and change in socioeconomic structure of the population. Eventually consumerism has started and the population has increased further. The United Nation has reported that the world population increased from 2.5 billion in 1950 to 7.8 billion in 2021. The growth of population is naturally followed by an increasing rate in demand for goods which results in expansion of industrialization even further. While the industrial facilities are spreading to produce more to meet up the demand for goods, resources and space are not increasing. On the other hand, expansion of industries has brought the concern of pollution which is an increasing threat for any living organism on earth. Hence, a need for treatment and/or change of the existing manufacturing processes has been arisen. The researches showed that the manufacturing processes in the chemical industry can be intensified in

order to reduce the chemical waste and utilize environmentally friendly energy sources.

The name of PI was previously described as a decrease in chemical plant size while keeping the product quality the same, and the first conference on PI took place in 1995 [1]. Over the course of years, both the description and methodology have been interpreted and discussed many times in different ways [2]. A more structured definition of PI based on fundamentals was proposed by Van Gerven and Stankiewicz in 2009 [3]. According to their study, the aim of intensification should target the molecular level, by using one or more of four fundamental approaches: structure (spatial domain), energy (thermodynamic domain), synergy (functional domain) and time (temporal domain). Moreover, scaling is also divided into three categories as the molecular scale (molecular collisions, molecular diffusion), mesoscale (particles, bubbles, films, phases), and macroscale (processing units, processing plants). The PI is limited by the number of devices offering all the ideal conditions for structural and fundamental approaches. However, researches on microstructural devices, often referred to as microreactors, microstructured devices or microstructured reactors, have been very promising [4, 5]. These are small-structured devices which are mostly integrated with the function of flow.

Microstructured devices are known for their low cost, less energy consumption, easy and safe handling of hazardous chemicals, and the precise control ability of reaction parameters [6]. However, they might suffer from various problems related to clogging and fouling due to their small volumes, potentially resulting in low efficiency and poor quality of production. Invasive techniques are definitely not the solution for cleaning of microstructured reactors. At this point, ultrasound has been involved into processing via microstructures [4, 5, 7, 8]. Ultrasound is an alternative energy source which is not only a solution for clogging and fouling problems, but also differs from conventional energy sources by being non-contact, sustainable and environmentally friendly. Ultrasound provides also micromixing which contributes to the effective turbulent mixing and enhances mass and heat transfer in the flow [9]. Apart from the physical effects, ultrasonic cavitation initiates and/or contributes to chemical activity by introducing extremely high pressure and temperature spots into the reaction medium of microstructed reactors [10, 11, 12].

In order to achieve an efficient combination of the physical and chemical effects of ultrasound and its integration into microstructured devices, a variety of designs have been reported targeting certain chemical reactions in the last decades [4, 5]. Some of these reactions and designs are the following: liquid-liquid extraction [13] and intensification of gas-liquid mass transfer [14] by a direct contact method of flow tube merging with Langevin transducer, OH radical formation in a polydimethylsiloxane(PDMS)-based microfluidic reactor in contact with the driving piezo ceramic [11], handling solid forming reactions by a teflon stack microreactor with an integrated piezoelectric actuator [7] or in a microchannel on top of a Langevin transducer [15], crystallization through sonication of a flow cell by an integrated piezo ceramic [16], fabrication of nanoparticle-coated microbubbles through microfluidic channels irradiated by an ultrasonic horn [17], crystallization of acetylsalicyclic acid through millichannels sonicated by an ultrasonic horn [18]. Apart from different transducer types and assembling techniques as they are exemplified here, microstructured flow reactor designs can also be classified by the material composition and dimensions of channels. Glass channels attached to a microscope slide [11], PE/5 channels integrated to an ultrasonic horn [17], PDMS channels via lithog-

raphy [19], silicon channels via micromachining [5], or polytetrafluoroethylene(PTFE) channels in a teflon microreactor [7].

All recent developments in microfluidic reactors have been showing a great improvement in reaction yield, less energy consumption, high purity. However, in contrast to such big achievements in small scale flow chemistry processes, there are only few numbers of processes adapted to industry [6]. The reason is due to the difference in scales between laboratories (*i.e.* g/h or g/min) and production sites (*i.e.* kg/h or more). Moreover, there are missing links when it comes to the fundamentals of chemical reactions performed by ultrasound. In molecular level, interaction between ultrasound and matter has not been understood well yet. The *European Training Network for Continuous Sonication and Microwave Reactors (COSMIC)* has been funded by the *EU Framework Programme for Research and Innovation Horizon 2020* (under Grant Agreement No. 721290) in order to improve the current knowledge and technological developments on process intensification. The project targeted to fill the gaps in fundamental research, scale the laboratory production up to the industrial level, investigate new flow chemistry processes and improve the existing ones by being a bridge between research in universities and production in industries. As one part of this effort, the present thesis has been supported by COSMIC MSCA-ETN. Its overall aim is to investigate the correlation between the acoustics and the flow in terms of cavitation characteristics, to analyze the relationship between physical and chemical effects in small sonicated flow channels, and to examine the sonochemical activity in such systems.

Chapter 2

Theory

Cavitation occurs when an external force exceeds the tensile strength of a liquid. Then voids appear that immediately fill with vapor and also non-condensable gas that might be dissolved in the liquid. Thus bubbles are created. The occurrence and further dynamics of the bubbles caused by tensile stress is termed as cavitation. It has to be distinguished from *boiling*, where the phase transition and the bubbles appear through heating of the liquid beyond the boiling point.

The demand on better understanding of cavitation has been constantly increasing, as the diversity of its application areas grows. Cavitation finds itself a place in a wide range of applications in various disciplines of science and engineering. One typically separates *hydrodynamic cavitation* in systems such as pumps [20], ship propellers [21], or cooling systems [22], where the tensile stress is created in a bulk liquid flow, and *acoustic cavitation*, where the tensile stress appears in a strong sound field. The latter has applications, for instance, in cleaning [23], chemistry [23], nanoparticle synthesis [24], or wastewater/sewage treatment [25]. Also in the medical ultrasound, acoustic cavitation can play an important role, e.g. for the breaking of kidney stones [26].

Cavitation was first noticed by the erosion problems of ship propellers in the late 19^{th} century, and it became clear that the rupture of the liquid, appearance of bubbles and their action on solid surfaces could have tremendous results. To approach the phenomenon in more detail, bubble dynamics was theoretically described through the collapse (implosion) of a single, spherical, empty bubble by Rayleigh [27]. His result that the imploding bubble wall would reach infinite speed for this idealized case was already pointing to the fact that bubbles can amplify energy density enormously [28], and that the collapse is often the most interesting phase of a bubble life.

After World War I, interest in experimental and theoretical aspects of high intensity sound field propagation in liquids had continuously increased [29, 30]. However, back then, technical limitations in capturing, controlling and observing bubbles, and their exceedingly fast non-linear behavior had restricted the further investigations of cavitation bubbles. In the course of time, most of these difficulties have ceased within the advancements in modern computers and imaging technologies; thereby, researches have become fast at a pace.

2.1 Acoustic cavitation

Sound is a form of an energy that propagates as an acoustic wave through any medium (except vacuum), by transferring energy from one particle to another [Fig. 2.1]. Depending on the frequency of pressure oscillations, sound waves are divided into three main ranges as *infra-sound, audible sound* and *ultrasound*. The frequency range of 20 Hz to 20,000 Hz is audible by human hearing. Frequencies below the audible range are called infra-sound, whereas those higher than the upper audible limit are named ultrasound.

Acoustic cavitation is the rupture of a liquid as a result of tension applied by intense sound field. This leads the formation of negative pressure pockets in the liquid, namely *cavitation bubbles*. Life of a bubble comprises several aspects, namely formation, growth, oscillation, and potentially collapse, which is denoting a violent implosion in this context. Finally, a bubble can split into fragments, dissolve, or merge with other bubbles. It turns out that each such incident throughout the lifetime of a bubble is another challenging research topic for itself due to the complex nature of cavitating liquids.

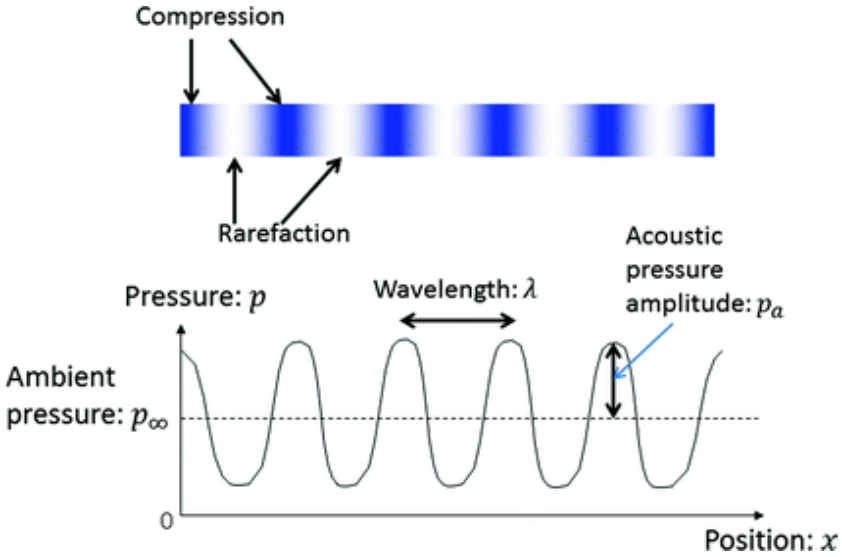

Figure 2.1. Sound wave [31]

A typical sound field is illustrated in Fig. 2.1. As sound propagates in a liquid, and if the pressure amplitude (acoustic amplitude) of the sonic wave is higher than the ambient pressure, the instantaneous pressure in the liquid becomes negative (rarefaction phase). This can tear apart the liquid molecules directly, if the cohesive forces are overcome by the tension – like solids break under sufficient tension. However, since the tension values of pure liquid breakage (molecule separation) are typically quite high (order of kbar [32]), cavitation in so-called real liquids appears at weaker spots, so-called *nuclei*. These might be floating dust particles, walls, pre-existent bubbles that are somehow stabilised against dissolution, or other contaminants of the liquid. Furthermore, since the solubility of gas content (*i.e.* air) in the liquid is proportional to the pressure, gas no longer be dissolved in equilibrium at the negative local pressure regions. Thus the negative pressure can cause the evaporation of liquid if a sufficient amount of nuclei are present. In many technical applications where real liquids (e.g. tap water or sea

water) are used, nuclei are abundant, and one can approximate the pressure threshold where cavitation starts with the vapor pressure. In the case of hydrodynamic cavitation, rapid liquid flow causes formation of bubbles filled with vapor of the liquid (*e.g.* flow in a Venturi tube [33]), and it is generally assumed that this happens when the local pressure eventually becomes lower than the saturated vapor pressure.

However, *cavitation threshold* depends strongly on the number and type of nuclei present, and thus in acoustic problems, the sonicated volume of liquid and the irradiation time (which translates into a dependency on the sound frequency) play an important role. Therefore, in many practical problems, the cavitation threshold lies somewhere between (positive) vapor pressure and several bars acoustic driving pressure amplitude (causing an corresponding negative pressure during the tension phase of the sound wave).

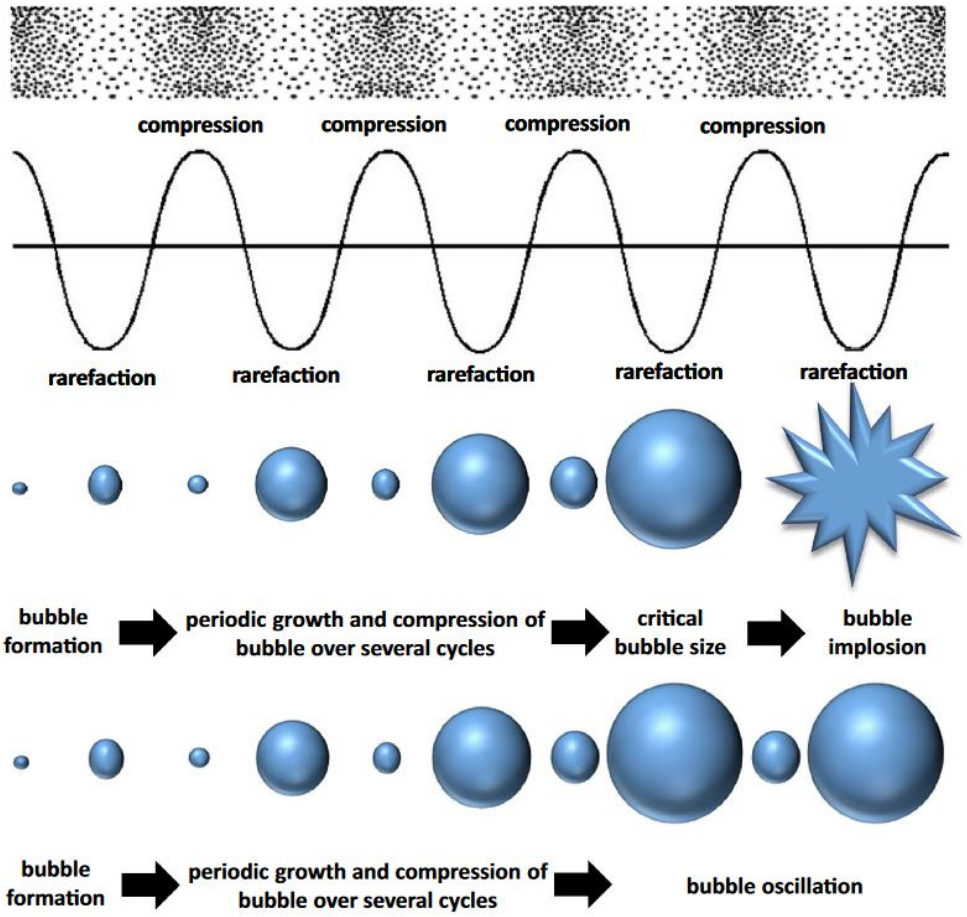

Figure 2.2. Schematic image of acoustic cavitation process [34]

Due to the tensile stress, the bubble volume further expands in the rarefaction phase (See Fig. 2.2). In later stages of the flow or the sound wave, a positive pressure applies an inward force onto the bubble wall, and this results in volume shrinking and compression. This can ultimately lead to a strong collapse with extreme conditions in and nearby the bubble, which is the key event of cavitation. Bubble collapse is a quasi-adiabatic process, which causes a dramatic change in pressure and temperature inside the bubble,

results in formation of shock waves in the surrounding liquid, turbulence, generation of chemical reactions, erosion of materials interacted with collapsing bubbles, or emission of light [35].

2.1.1 Bubble dynamics

Let us imagine a spherical bubble in liquid. In such a free boundary problem, in order to analyze the bubble dynamics, the mechanical and thermal properties of the liquid should be described by conservation equations. Additionally, laws of mass, momentum and energy conservation should be applied to a gas filled bubble in an infinite liquid. The fundamental equations needed to investigate the dynamics of a bubble can be given in spherical symmetry as [36, 37]:

$$Continuity: \frac{\partial \rho}{\partial t} + \frac{\partial}{\partial t}(\rho u) + \frac{2\rho u}{r} = 0, \tag{2.1}$$

$$Momentum: \frac{\partial u}{\partial t} + u\frac{\partial u}{\partial r} = -\frac{1}{\rho}\frac{\partial P}{\partial r} \tag{2.2}$$

$$Energy: \rho S_v(\frac{\partial T}{\partial r} + u\frac{\partial T}{\partial r}) = -P(\frac{\partial u}{\partial r} + \frac{2u}{r}) + \frac{4\mu}{3}(\frac{\partial u}{\partial r} + \frac{u}{r})^2 + K(\frac{\partial^2 T}{\partial r^2} + \frac{2}{r}\frac{\partial T}{\partial r}) + \rho q \tag{2.3}$$

where ρ, u, P are the density, particle velocity, and particle pressure of the liquid, respectively. S_v is the specific heat capacity at constant volume of liquid, T is the temperature and q is the heat flux in the liquid. μ and K is the viscosity and thermal conductivity of liquid, respectively.

The equation for the gas diffusion in liquid can be written as:

$$\frac{\partial C}{\partial t} + u\frac{\partial C}{\partial r} = D(\frac{\partial^2 C}{\partial r^2} + \frac{2}{r}\frac{\partial C}{\partial r}) \tag{2.4}$$

where, C is the concentration of diffused gas in the liquid and D is the diffusivity of the gas. At the bubble wall, where r=R(r), the equations for boundary conditions are:

$$D\frac{\partial C}{\partial r} = \frac{1}{4\pi R^2}\frac{d}{dt}(\frac{4}{3}\pi R^3 \rho_g) \tag{2.5}$$

$$P + \frac{2\sigma}{R} = P_T + \frac{4\mu}{3}(\frac{\partial u}{\partial r} - \frac{u}{r}) \tag{2.6}$$

where, ρ_g and P_T are density and pressure of the gas content of the bubble interior, respectively and σ is the surface tension of liquid.

Mass and thermal diffusion in the liquid can be written as [36]:

$$K\frac{\partial T}{\partial r} = \frac{1}{4\pi R^2}\frac{d}{dt}(\frac{4}{3}\pi R^3 \rho_T)\left[L + \frac{4\mu}{3\rho}(\frac{\partial u}{\partial r} - \frac{u}{r})\right] + \rho_T\frac{RC_v}{3}\frac{\partial T}{\partial t} + P_T u \tag{2.7}$$

where, ρ_T is the density of the total gas content, and C_v is the specific heat of gas at constant volume.

The acoustic pressure at $r = \infty$ is given as:

$$P = P_0(t) = P_0 - P_A sin(\omega t) \tag{2.8}$$

The simplest case of the equation of state for incompressible liquid is ρ=constant, whereas that of gas refers to the perfect gas equation,

$$PV = R_g T \tag{2.9}$$

with the molar volume V. These equations (*Eq:2.1- Eq:2.9*) are the fundamental equations used to analyze bubble dynamics.

2.1.2 Bubble oscillations

A small change in pressure of the bubble interior leads the bubble to oscillate gently around its equilibrium radius (R_0). Expansion decreases the pressure inside, and the bubble tends to maintain R_0, whereas compression increases the pressure resulting in a rebound. The consecutive volume changes induce bubble radius (or volume) oscillations around R_0 with its own resonance frequency f_{res} which is called *Minnaert frequency* [32, 38] or *linear resonance frequency*, and which is given as:

$$f_{res} = \frac{1}{2\pi R_0}(\frac{3\gamma p_0}{\rho})^{1/2} \tag{2.10}$$

The Minnaert frequency depends on the density of liquid ρ, the ambient pressure P_0, and the effective polytropic exponent γ. Inversion of the resonance frequency formula gives the linear resonant radius in dependence of the applied (single) frequency f in monofrequent acoustic fields: $R_{res} = 1/(2\pi f)[(3\gamma p_0)/\rho]^{1/2}$. Resonance parameters of bubbles or fields are important to take into account for different types of applications of ultrasound, and they particularly have an impact on sonochemistry.

For very small pressure amplitudes, the bubble oscillates linearly, and for each damping the amplitude vs. frequency response can be normalized to one curve, i.e. a harmonic oscillator. However, if the oscillation amplitude becomes higher, the bubble experiences a large expansion. And in return, there must be a compression potentially resulting in a radius below zero; but, negative radii are not physical anymore. Hence, the restoring forces behind the collapse and rebound of a bubble are not symmetric, the bubble oscillates nonlinearly. Bubble oscillations turn out to be even more anharmonic, if the oscillation amplitude increases. Hence, for each damping, the response of a bubble oscillator differs, and the frequency dependency can no longer be normalized to a single curve. In this case, the equation of linear resonance frequency (2.10) has to be modified [39]. Nonlinear resonances occur at rational multiples of the linear resonance frequency, and the resonance curves become tilted, which develops into hysteresis. Finally, period doubling and chaotic oscillations can develop for certain parameter ranges at elevated driving pressure [40].

2.1.3 Collapse of a spherical bubble

During the course of a strong anharmonic oscillation, the bubble interior can rapidly shrink to a small volume minumum. The rapid compression is termed implosion or collapse since it is guided by the inertia of the inrushing water mass. Typically, the bubble wall motion is inverted to a rebound by the compressed gas inside which develops a counter pressure. Indeed, the collapse of an *empty* bubble would be the most extreme case of a collapse; since there is no gas or vapor pressure inside to interact with the inflowing liquid, no deceleration of the wall and no rebound would occur.

Assume a spherical collapsing empty bubble in an incompressible liquid. Since the bubble interior is empty, inward motion of liquid would not interact with any gas or vapor pressure during collapse. This means that there will be no cushioning in order to stop and reverse the liquid motion (hence no regrowth). In such a case, most extreme conditions of a collapse are achieved.

The inertial collapse of an spherical empty cavity was first formulated by Rayleigh, and named after its pioneer as *Rayleigh collapse* [27]. As such collapse comes to closing, speed and pressure at the bubble wall are calculated theoretically as infinite. However, this is not a realistic hypothesis. There must be something in order to prevent the divergence; which is the addition of gas. If the bubble is gas-filled, the pressure inside the bubble increases drastically throughout the implosion, as the density inside the bubble increases almost up to the condensed phase in which the bubble reaches its minimum radius. Then, bubble collapse stops and the enclosed gas reveals a dramatic increase in temperature and pressure, which can originate chemical reactions in the gas and vapor (sonochemistry) and a flash of light (sonoluminescence).

A spherical empty bubble oscillating in an infinite incompressible liquid is sketched in Fig. 2.3. If the radius of the bubble is R, then the spherically symmetric radial velocity and acceleration at the bubble wall become $\dot{R}$ and $\ddot{R}$, respectively. At any arbitrary distance r in the liquid, the radial velocity of the bubble will be $\dot{r}$ which is expressed as $\dot{r} = R^2\dot{R}/r^2$.

Then, the velocity potential ϕ is derived as [41]:

$$\phi = -\int_r^\infty \dot{r}\, dr \tag{2.11}$$

The equation of motion of liquid can be written by Bernoulli's equation:

$$\frac{p - p_\infty}{\rho} = -\frac{\partial\phi}{\partial t} - \frac{1}{2}u^2 = \frac{2R\dot{R}^2 + R^2\ddot{R}}{r} - \frac{1}{2}\frac{R^4\dot{R}^2}{r^4} \tag{2.12}$$

where, p and ρ are the pressure and the density of the liquid, respectively, at distance r, and p_∞ is the pressure in the liquid far from the bubble. The radial velocity at the bubble wall (r=R) is:

$$\frac{p_b - p_\infty}{\rho} = R\ddot{R} + \frac{3}{2}\dot{R}^2 \tag{2.13}$$

where, p_b is the pressure of the liquid at the bubble wall. For $p_b = 0$, Eq. 2.13 is the

basic model for an empty spherical bubble unbounded to the surrounding liquid, often called *Rayleigh model* [27]. Actually, this equation then simply expresses *the collapse of a void*, since only the liquid inertia is taken into consideration, and no other factors are included.

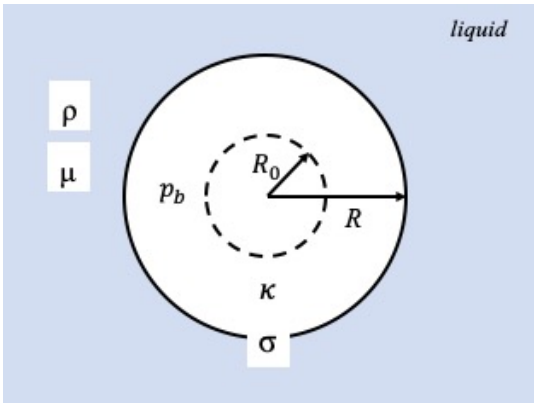

Figure 2.3. Bubble parameters

According to the right hand side of the Eq. 2.13, the equation of the bubble wall motion is $R\ddot{R} + (3/2)\dot{R}^2 = p_\infty/\rho$ which has a solution in the form of $R(t) = R_0[(t_* - t)/t_*]^{2/5}$. According to this solution, the speed of the bubble wall diverges when the closing time of collapse is being reached ($t = t_*$). This singularity of the solution is considered the main hydrodynamic reason of a strong implosion which facilitates sonochemical reactions [27].

The divergence of the bubble wall velocity can be prevented by taking some other factors into account. The viscosity of the liquid and surface tension of the bubble wall are considered possible effects acting as a cushion to stop the inward liquid motion [42]. However, these forces are not strong enough to prevent the divergence alone [1].

Another effect is the existence of gas content inside the bubble. The simplest case is that the enclosed gas undergoes a compression, obeying the adiabatic equation of state [2]. According to this assumption, heat cannot escape from the bubble interior and it is eventually captured due to the speed of collapse, or the exchanged heat must be negligible with respect to the variations in the internal energy. The pressure of compressed gas tends to infinity stronger than the acceleration of the inward liquid motion [44]. Hence, divergence of the velocity of the bubble wall is avoided, although it is still very high. At that moment, the minimum bubble size of the collapse is reached, and the elastic nature of gas might also lead the bubble to regrow by reversing the motion of liquid moving inwards.

Now, let's consider the case of a gas-filled spherical cavity. It is assumed that the pressure p inside the bubble is comprised of both gas and vapor pressure, and which

[1] Viscosity of the liquid (μ)and the surface tension (σ) of the bubble wall have also singularities as $4\mu\dot{R}/R \propto (t_* - t)^{-1}$ and $\sigma/R \propto (t_* - t)^{-2/5}$, respectively. However they do not diverge as fast as inertial acceleration.

[2] The assumption of adiabatic bubble motion neglects heat conduction, *i.e.* the rate of heat transfer across the bubble wall. The Péclet number, a dimensionless parameter comprising the thermal diffusivity of gas and the bubble wall speed, shows that the bubble oscillations are mostly isothermal. In order to prevent the unrestricted heat exchange for adiabatic motion, the Péclet number has to be of order unity [42, 43]).

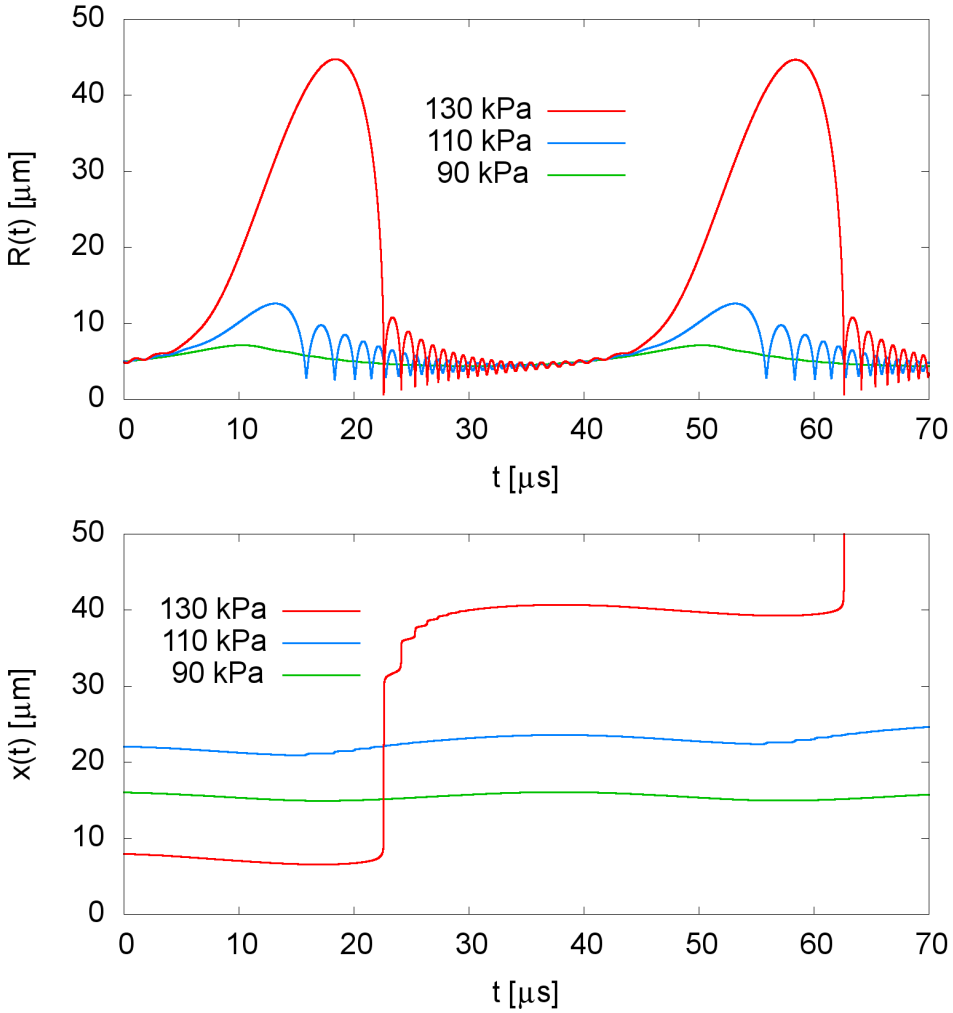

Figure 2.4. Transition to strong collapse oscillation around the Blake threshold (calculated with the Keller-Miksis model). Top: Bubble radius vs time curve for a bubble sinusoidally driven by 25 kHz, and with rest radius of 5 µm. The bubble oscillation remains nearly sinusoidal up to about 90 kPa. At 110 kPa, first collapse oscillations take place with a typical peak around the minimum radius. As the pressure increases to 130 kPa, the bubble expands up to nearly ten-fold of its rest size, and one very strong collapse follows (here at 22.5 µs). Such collapse profiles result in extreme heat and temperature conditions which facilitate chemical reactions (see Section 2.2). Bottom: Translation of the same bubble as it is driven by a plane travelling wave in +x direction. For lower driven pressures (90 and 110 kPa), the bubble merely moves back and forth with a small displacement in the direction of wave propagation. As the driving pressure is increased to 130 kPa, the bubble moves and jumps in +x direction during the collapse phase around 22.5 µs. The displacement is of the order of the fully expanded bubble size (R_{max}).

obeys $p(4\pi R^3/3) = R_g T$. If the compression is adiabatic, there will be no heat and mass transfer between the cavity and the liquid; then $p(4\pi R^3/3)^\gamma$ will be constant where γ is the ratio of specific heats of the gas inside the bubble at constant pressure and constant volume ($\gamma = c_p/c_v$). On the other hand, if γ equals to 1, the compression is isothermal. Then, let's assume the rest radius of the bubble is R_0 and the pressure inside the bubble is initially $p_0 + 2\sigma/R_0 - p_v$ at R=R_0, where σ is the surface tension at the bubble wall, p_v is the vapor pressure and p_0 is the ambient pressure. If the bubble radius changes to R at constant temperature, the gas pressure inside the bubble becomes;

$$p_b = (p_0 + \frac{2\sigma}{R_0} - p_v)(\frac{R_0}{R})^{3\gamma} + p_v \tag{2.14}$$

Substituting Equation 2.14 into Equation 2.13 results [45, 46]:

$$R\ddot{R} + \frac{3}{2}\dot{R}^2 = \frac{1}{\rho}[-\frac{2\sigma}{R} + p_b(R) - p_\infty(t)] \tag{2.15}$$

This equation and its variants were initially derived by Noltingk and Neppiras [46, 47]. The effect of viscosity of a liquid (μ) in the bubble oscillation was taken into account by Poritsky in 1952, and the viscosity term was included:

$$R\ddot{R} + \frac{3}{2}\dot{R}^2 = \frac{1}{\rho}[-\frac{2\sigma}{R} - \frac{4\mu\dot{R}}{R} + p_b(R) - p_\infty(t)] \tag{2.16}$$

Eq. 2.13, 2.15, 2.16, and their different variants, called *Rayleigh-Plesset equation*, provide a pretty good approximation for the dynamics of a gas-filled spherical cavity in an incompressible liquid [48]. As a special case of the Navier-Stokes equation, the Rayleigh-Plesset equation is also usually solved numerically and it has no known analytical solution, apart from special cases [27]. The Fig. 2.4 depicts the numerically simulated radius profile of a bubble driven at different amplitudes.

In this model, $p_\infty(t)$ is composed of the ambient pressure p_0 and the acoustic pressure p_{ac}. The acoustic pressure, an additional external pressure applied to the bubble wall, is assumed as a single frequency sinusoidal ultrasonic wave with $p_{ac} = -p_a sin(2\pi f t)$, where p_a is the pressure amplitude. Then $p_\infty(t)$ becomes;

$$p_\infty(t) = p_0 + p_{ac} = p_0 - p_a sin(2\pi f t) \tag{2.17}$$

According to the Rayleigh-Plesset equation, the acceleration of the bubble wall is $\ddot{R} = -\dot{R}^2/2R$. This means that the magnitude of the bubble wall acceleration increases, so the collapse of the bubble becomes faster by time. However, the assumption of incompressibility of the liquid is not longer valid if the velocity of the collapsing bubble wall comes into the range of the sound speed c in the liquid. To obtain more accurate and realistic bubble collapse dynamics, the liquid compressibility can be taken into account by the Keller-Miksis equation, which reads [49]:

$$(1 - \frac{\dot{R}}{c})R\ddot{R} + \frac{3}{2}(1 - \frac{\dot{R}}{3c})\dot{R}^2 = (1 + \frac{\dot{R}}{c})\frac{p_l}{\rho} + \frac{R}{\rho c}\frac{dp_l}{dt} \tag{2.18}$$

with the liquid pressure at the bubble wall;

$$p_l = (p_0 + \frac{2\sigma}{R_0} - p_v)(\frac{R_0}{R})^{3\gamma} + p_v - \frac{2\sigma}{R} - \frac{4\mu\dot{R}}{R} - p_0 - p_{ac}(t) \tag{2.19}$$

This equation is an approximation to first order in the bubble wall Mach number $Ma = \dot{R}/c$, and the sound speed is taken as a constant. Even better approximations to higher order in Ma can be derived, but turn out to be of minor accuracy gain in comparison to the higher programming effort [50]. A slight improvement can be achieved by treating the speed of sound as pressure dependent, which is expressed via the Tait equation of state as $c_{L,b} = \sqrt{n(p_b + B)/\rho_{L,b}}$, where $c_{L,b}$ and $\rho_{L,b}$ are the speed and density of liquid at the bubble wall, respectively. The parameter n is 7.15 and B equals to $3.049 \cdot 10^8$ Pa, for a good fit to the experimental pressure-density relation of water [51, 52]. Including this into the bubble model, one obtains the Gilmore-Akulichev equation [53, 54]. However, since it is not employed here, we do not give the full equations here but refer to Leighton [48] as a further reference.

In addition to compressibility corrections for the liquid, one can also include corrections for the gas. Since the bubble is excessively compressed during the closing moment of a catastrophic collapse, the density of the gas and vapor content inside the bubble converges almost to the condensed phase, and the finite sizes of the molecules become important. This can be modeled by an excluded volume in the framework of a Van-der-Waals equation of state. Further, heat conduction can be coupled to the radial dynamics as well; for both model extensions see for instance [44]. Because these models are not used here, the equations are not given explicitly.

However, an important geometrical aspect comes into play in the framework of the present study: The cavitation bubbles are usually contained within a tube of small diameter. This constriction in form of the nearly rigid tube walls hinders the free three-dimensional liquid flow around the bubble, and actually the assumption of spherical symmetry breaks down. In an attempt to conserve the purely radial description of the bubble dynamics, geometry corrections of the RP-like models between plates or within tubes have been introduced by various authors [55, 56]. In the scope of this study, Zudin's model [57, 58] for bubbles inside a rigid tube is employed. It introduces an additional term to the *Keller-Miksis equation*, assuming a spherical bubble in a horizontal circular rigid tube with the radius of R_T, and the length of L:

$$(1 - \frac{\dot{R}}{c} + \frac{RL}{{R_T}^2})R\ddot{R} + \frac{3}{2}(1 - \frac{\dot{R}}{3c} + \frac{4RL}{3{R_T}^2})\dot{R}^2 = (1 - \frac{\dot{R}}{c})\frac{p_l}{\rho} + \frac{R}{\rho c}\frac{dp_l}{dt} \tag{2.20}$$

As can be seen from the equation, tube radius and tube length appear only in the combination L/R_T^2 as a prefactor to the momentary bubble radius R, forming two correction terms. These terms represent an effectively higher inertia of the liquid, since the liquid velocity around the bubble cannot decay as fast as in a free liquid. This means that "more" liquid has to be pushed away by the bubble oscillation than in a free situation. The main effects are that the eigenfrequency of the bubble is reduced, and that the expansion of driven bubbles is less than in unrestricted geometry. It should be mentioned that this "corrected" model is of course still an approximation, since the dynamics cannot be truly radial. Further, the viscous damping via the boundary layers at the tube walls is neglected, as well as sound wave reflections from the walls and from the tube

endings. Attempts to investigate bubble dynamics in a tube using a full Navier-Stokes formulation can be found, for instance, in [59].

2.1.4 Bubble nucleation

Even in silent conditions, liquids have micron-sized (or smaller) entities of non-condensable gas which are small pre-existing bubbles called *nuclei*. Temperature, gas content and treatments applied to the liquid are the parameters determining the density and size distribution of nuclei population in liquid [60]. The first occurrence of cavitation bubbles with the excitation of tensile stress is called *nucleation* and the minimum tensile stress required to initiate nucleation in a liquid is termed *cavitation threshold*. Within the alternating pattern of acoustic pressure, bubbles undergo some complex events and subsequently new bubbles are created in each cycle. The global transformation of a liquid from silent to cavitating is called *cavitation inception*.

There are different sources and mechanisms for bubble nucleation in acoustic cavitation, and they are important for the characterization of spatial cavitation pattern. For liquid, which is subjected to no special treatment (*i.e.* not degassed) or not exceptionally clean, cavitation might be initiated by *activation* of pre-existing (passive) nuclei rather than "real" *nucleation* in the sense of a tensile rupture of the cohesive bonds between adjacent liquid molecules. Bubbles can be originated from stabilized gas pockets at solid surfaces floating in the bulk, such as some particles or motes in the liquid, or at crevices of the liquid container wall. These nuclei expand due to the high tensile stress by the acoustic wave and develop into acoustic cavitation bubbles. They can also be nucleated from cosmic rays absorbed in the liquid, or by some pre-existing bubbles stabilized by surfactant contaminations in the bulk liquid. Sometimes, surface instabilities of an active bubble induces fragmentation and that gives rise to the nucleation of daughter bubbles and initiates or sustains acoustic cavitation.

Cavitation in pure liquids occurs by *homogeneous nucleation* which requires a much high acoustic pressure amplitude to attain tensile rupture due to the absence of pre-existing nuclei [32]. On the other hand, *heterogeneous nucleation* is a typical case for the experimental research. Contribution of pre-existing (passive) nuclei into cavitation in 'real' liquids lowers the required threshold of tensile stress to achieve cavitation. Some parameters, affecting the cavitation threshold such as liquid impurities, container walls, or dissolved gas, are not always easy to control. Consequently, such factors lead to the fact that cavitation conditions are sensitive and variable to some extent, and give a certain amount of randomness to the cavitating system. Moreover, concentration of nuclei changes during cavitation by gas diffusion (*i.e.* degassing) as a result of bubble oscillations and coalescence or splitting events. This means that the bubble numbers and bubble equilibrium radii can change during sonication, and it is not a straightforward task to analyze bubble populations.

2.1.5 The Blake threshold

Once an external pressure is applied to a liquid, cavitation happens quickly, so that buoyancy and dissolution can be neglected at first hand. The following analysis considers the pressure required to keep a bubble in static equilibrium, and this depends on its

radius [61, 47]. The Blake threshold pressure is a measure of "static acoustic cavitation" in the sense that a given bubble expands when exposed to a certain tensile (negative) pressure. The equilibrium radius of a bubble (R_0) is a crucial parameter for the bubble response.

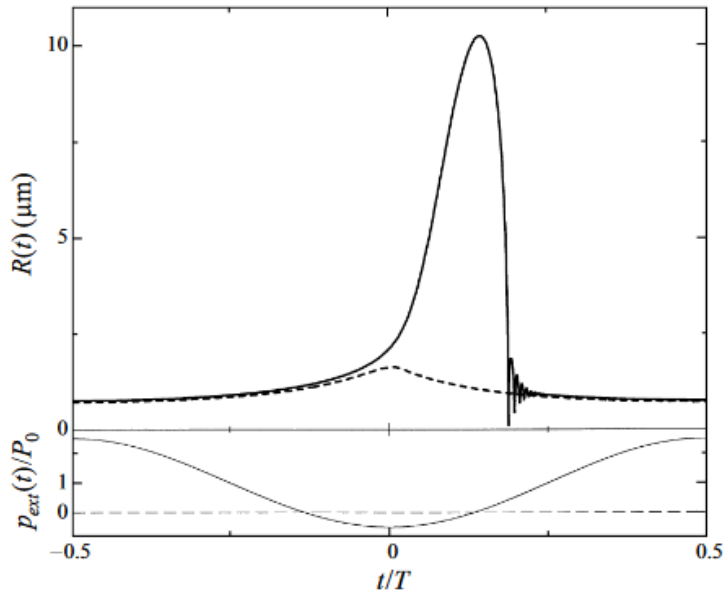

Figure 2.5. Radius vs time (normalized by the driving period) for two bubbles which are sinusoidally driven with a driving pressure amplitude of p_a=1.5 atm. One period of the oscillation is shown, and in the lower part, the net pressure (includig static pressure of 1 bar) is depicted. The bubbles have the equilibrium radii $R_0 = 0.85\,\mu m$ (dashed) and $R_0 = 0.90\,\mu m$ (solid). The smaller bubble oscillates only weakly, whereas the larger bubble expands to about tenfold equilibrium radius, and afterwards collapses strongly.

In order to transform a nucleus into a transient cavitation bubble, surface tension has to be cancelled out by the tensile part of the acoustic pressure p_{ac} which forms a pressure p_∞ at very large distances from the bubble together with the static pressure p_0. When a quasistatic acoustic pressure $p_{ac} = -p^* < 0$ is applied, the bubble undergoes a shift in size, and conditions for the new equilibrium size R_0^* require that $p_b(R_0^*) + p_v = p_s(R_0^*) + p_0 - p^*$. Here, p_0 is the static pressure in the liquid, and $p_s(R) = 2\sigma/R$ is the Laplace pressure by surface tension. Closer analysis reveals that a bubble exceeding a certain critical tension $-p^* = -p_{cr}^*$ can no longer find a stable expanded equilibrium size R_0^*, and it would expand within the quasistatic tensile pressure without bound. This criterion is called the *Blake threshold*. The critical tensile pressure p_{cr}^* is called the *Blake pressure* p_{Blake}. If expressed for a bubble with rest radius R_0 and neglecting vapor pressure, it reads [62]:

$$p_{Blake} = p_{cr}^* = p_0 \left[1 + \left(\frac{4}{27} \frac{\alpha_s^3}{(1+\alpha_s)} \right)^{1/2} \right], \qquad \alpha_s = \frac{2\sigma}{p_0 R_0} \tag{2.21}$$

Of course, in realistic situations, a static tension cannot be applied for a long duration, and the bubbles cannot grow indefinitely. Still, the Blake threshold is a standard measure of cavitation inception in oscillating (acoustic) fields and a crucial criterion for the

expansion and compression characteristics of bubbles of different rest sizes. For higher driving pressures, very small bubbles oscillate weakly and remain "passive", while larger ones expand considerably and collapse strongly, behaving "active". The transition between these two behaviours takes place rather suddenly at a relatively sharp defined bubble size. The Blake threshold is the key factor for understanding the transition between two different dynamics. In short, it marks the transition where the surface tension (Laplace) pressure of small bubbles can be overcome by the negative sound field pressure.

As an example of the sharply increasing R_{max}/R_0 expansion ratio for R_0 passing the Blake threshold, the response of two bubbles of different equilibrium sizes and driven at p_a=1.5 atm is given in Fig. 2.5. It is clearly visible that the smaller bubble oscillates weakly and reaches an expansion ratio of $R_{max}/R_0 \approx 2$, and no rapid collapse is observed. The time series of the larger bubble behaves the same as that of the smaller one until almost $t/T \approx 0$. Then it exhibits the high expansion rate $R_{max}/R_0 \approx 10$ which is followed by a strong collapse.

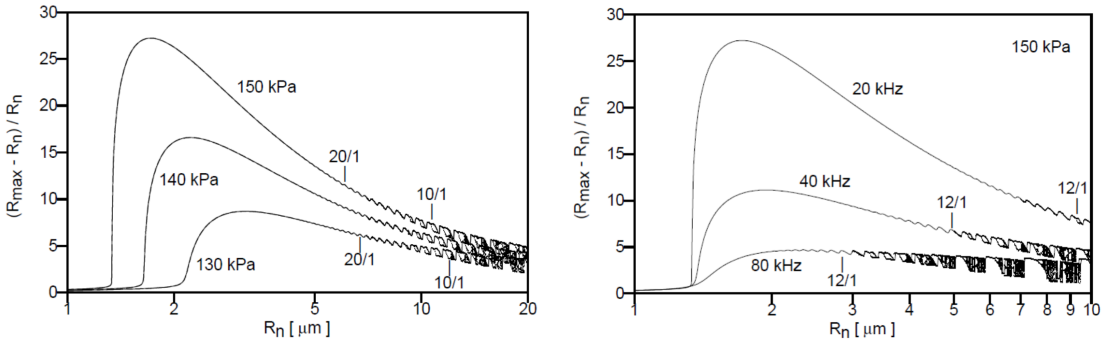

(a) Response of bubbles driven at 20 kHz and for different pressure amplitudes.

(b) Response of bubbles driven at 150 kPa and for different driving frequencies.

Figure 2.6. Bubble response curves: Normalized maximum expansion ratio $(R_{max}-R_n)/R_n$ vs bubble equilibrium radius (here named R_n, on logarithmic scale). The "jump" at the Blake threshold between about 1 and 2 μm is apparent. Images from [63].

The sharp transition is also illustrated in the response curves of Fig. 2.6, where the normalized expansion is shown in dependence of the equilibrium radius. It can also be seen that the phenomenon depends somehow on the driving frequency. This happens since the negative going acoustic pressure lasts shorter at higher frequency (remember that the derivation of the Blake threshold relies on quasistatic negative pressure, lasting "inifinitely" long). Thus, the pressure amplitude for significant expansion (and thus for this type of "cavitation activation threshold") needs to be higher at higher driving frequency. Still, the bubble sizes where the transition occurs vary only weakly with driving frequency and are generally around approximately 1 μm.

Fig. 2.7 shows the compression ratio R_{min}/R_0 of the minimum radius as a function of P_a and R_0. Similar to the expansion ratio, it is clearly seen that there is a sharp transition in compression ratio at the same R_0. For small values of R_0 and P_a, R_{min}/R_0 is near one and the bubbles oscillate weakly. On the other hand, for larger values of R_0 and P_a, a horizontal plane at $R_{max}/R_0 \approx h/R_0$ implies a collapse to a hard-core radius which is a strong collapse.

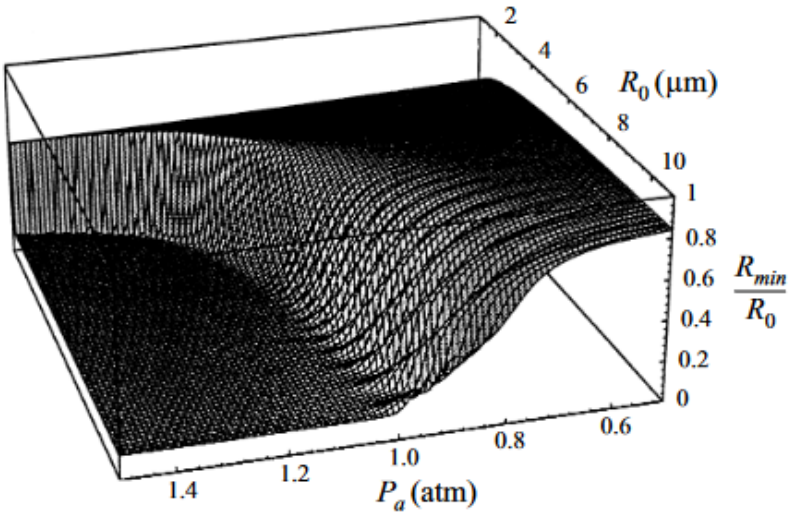

Figure 2.7. The compression ratio R_{min}/R_0 of the minimum radius as a function of P_a and R_0. For smaller R_0 and P_a, bubbles oscillate weakly, and for larger R_0 and P_a, bubbles undergo strong collapse. Retrieved from [62].

2.1.6 Bjerknes forces

Bubbles not oscillate only, they also move in space due to the forces exerted on them. For instance, even bubbles in silent liquid move from the bottom to the top of the container, since the hydrostatic pressure applies stronger force on the bottom than the top of the bubble resulting in bubble to be pushed to the surface of the liquid.

Acoustic radiation pressure is a force exerted on a body. An object in an acoustic field, roughly speaking, feels a force depending on its volume, and it is pushed from higher pressure zones to lower pressure zones. Analyses about such forces date back to the research of Lord Rayleigh in 1902 [27]. The acoustic radiation pressure on rigid spheres has been solved by King in 1934 [65]. Later on, compressibility of the sphere has also been taken into account by Yosioka and Kawasima [66]. In order to express the acoustic radiation pressure, standing waves are considered since they are used to enhance the sound pressure in the sound field. The acoustic radiation force $\langle P \rangle$ acting on a bubble in shape of a sphere whose radius is a and smaller than the acoustic wavelength can be calculated by integrating the radiation pressure over the surface of the bubble and taking the time average as follows:

$$\langle P \rangle = -\frac{4\pi}{k^2} \bar{E} \sin(2kh) F(\lambda, \sigma, k^* a) \tag{2.22}$$

where, k is the wave number of the medium, $\bar{E}$ is the mean total energy density in standing wave field, h is the distance of the center of sphere the anti-nodal plane of sound pressure, and angled brackets stand for time-averaging. F is a function of the density ratio $\lambda = \rho^*/\rho_0$ and the sound speed ratio $\sigma = c^*/c_0$. Here, * refers to a bubble, and 0 corresponds to a liquid medium. And the force is written as:

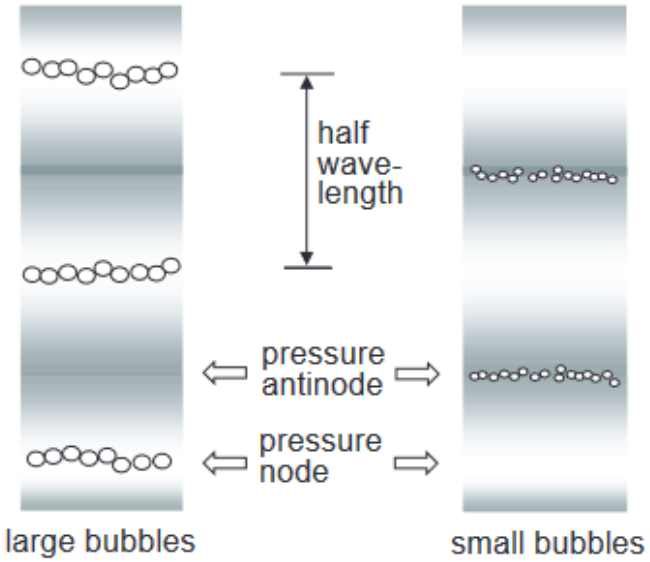

Figure 2.8. Bubbles larger and smaller than their resonant sizes in standing wave field. Retrieved from [64].

$$F(\lambda, \sigma, k^*a) = \frac{\sigma(k^*a)[3\lambda - (k^*a)^2]}{\sigma^2(k^*a)^6 + [3\lambda - (k^*a)^2]^2} \tag{2.23}$$

The direction of the bubble motion in a standing wave is determined by the force F. Since the sign of Equation 2.22 is negative, it follows that if F is positive, bubbles move toward the pressure antinode. In case of F being negative, bubbles are pushed towards the node. The force changes the sign at $k^*a/\sqrt{3\lambda} = 1$ which refers to resonant bubbles. It means that bubbles smaller than their resonant size move towards the pressure antinode, whereas larger ones move toward pressure node (see Fig. 2.8). The resonant frequency of a bubble has been previously given in Eq. 2.10.

While the analysis of sound pressure above is mainly based on a mismatch of acoustic impedance (sound speed c and density ρ) between fluid and contained particles, the main characteristic of oscillating bubbles is their compressibility and accordingly strong volume changes during their pulsation, along with their very low density. Therefore one can formulate the acoustic force on a bubble by an averaged "buoyancy" force caused by the local sound pressure gradient, and such forces are termed Bjerknes forces.

Bjerknes forces are a type of acoustic radiation forces explaining quite well the observed fast translational motion of bubbles in the ultrasonic field. Bjerknes forces are divided into two categories. *The primary Bjerknes force* acts on a bubble due to an external sound field that drives the bubble oscillations. On the other hand, *the secondary Bjerknes force* is exerted on an oscillating bubble due to the sound oscillations emitted from other bubbles nearby.

The bubble is assumed to be much smaller than the acoustic wavelength and having a time varying volume of $V(t)$. Then the momentary pressure force in an acoustic field which induces a time varying pressure gradient $\nabla P(x_0, t)$ at the bubble position x_0 is

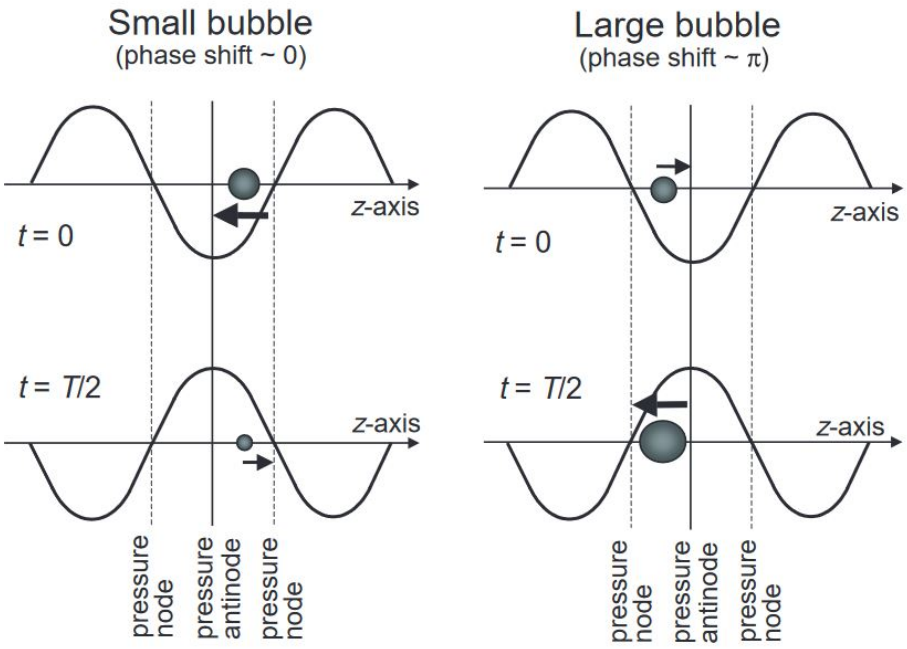

Figure 2.9. Bubbles smaller (left) and larger (right) than the resonant bubble size in a standing wave field during one oscillation cycle [64]. The arrows indicate direction and strength of the "momentary buoyancy" forces on the bubbles. By time averaging, the larger arrow "wins".

$-V(t)\nabla P(x_0, t)$. To derive the net force, the time-average is built:

$$F_{B1} = \langle V(t)\nabla P(x_0, t)\rangle. \tag{2.24}$$

which is called the *primary Bjerknes force*. The time average is typically not vanishing, since the bubble and the pressure gradient oscillations are generally phase coupled. The net force acting on the bubbles thus depends on the details of the oscillations of the bubble. These could be nearly harmonic at low driving, but also strongly nonlinear at high driving pressure. For a bubble oscillating weakly in a standing wave, its motion depends on its size in regard to the resonance radius, because this determines the relative phase between the bubble volume and the pressure (which in turn is coupled to the phase of the pressure gradient). A large bubble cannot follow the changes in pressure of ultrasound, oscillates out of phase (large volume during high pressure phase) and is finally pushed to the pressure node. On the other hand, if it is a small bubble, it can follow the pressure signal, oscillates in phase (small volume during high pressure phase) and is attracted by the pressure antinode. Bubble motion in a standing wave during one oscillation cycle is illustrated in Fig. 2.9. The resulting behaviour is consistent with the formulation of sound pressure on particles in standing waves, that has been given above.

In propagating acoustic waves, bubbles with a size near the resonant radius feel a strong force in the direction of the propagating wave, whereas a weaker force exerts on bubbles which are much smaller or larger than the resonance size.

The primary Bjerknes force can be written for a single pressure field by introducing a

partially varying amplitude and phase: $p(x,t) = p_a(x)[cos(\omega t(+\phi(x))]$, as:

$$F_{B1} = -\nabla p_a(x)\langle V(t)cos(\omega t + \phi(x))\rangle + p_a(x)\nabla\phi(x)\langle V(t)sin(\omega t + \phi(x))\rangle \tag{2.25}$$

First and second terms on the right hand side refer to a standing wave and travelling wave contribution, respectively. For the ideal cases of a plane standing wave, $p_a = cos(kx)$ and $\phi = constant$, for some wave vector k.

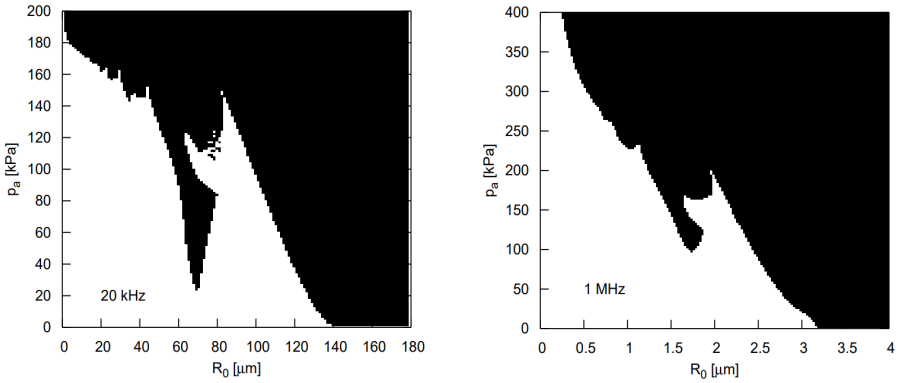

Figure 2.10. Primary Bjerknes force on bubbles in a standing wave of 20 kHz (left) and 1 MHz (right). The effect of the force is given in the plane of bubble equilibrium radius and driving pressure amplitude: white regions correspond to forces in direction of higher pressure amplitude (attractive antinodes), while dark regions indicate forces to lower amplitudes (repulsive antinodes). Figure from [67].

The secondary Bjerknes force has also an impact on bubble motion. Unlike the primary Bjerknes force, the secondary Bjerknes force is not directly derived from the incident sound field. Instead, it results from the scattered sound field emitted from an oscillating neighbored bubble. The secondary Bjerknes force can be expressed as [68]

$$F_{B2}^{1,2} = -\frac{\rho}{4\phi}\frac{(x_2 - x_1)}{|x_2 - x_1|^3}\langle \dot{V}_1(t)\dot{V}_2(t)\rangle \tag{2.26}$$

The equation gives the force of bubble 1 at position of x_1 exerted on bubble 2 at location of x_2. It is clearly seen that the strength of force is inversely proportional to the squared bubble-bubble distance. Moreover, the time averaged term is another determinant factor for the magnitude and sign of the force. This brings consideration of some other parameters which are time-dependent such as bubble size and acoustic pressure at the location of the bubbles. Therefore, many different situations are possible depending on bubble size and time. The possibilities can be simplified to the relative oscillation phase of the bubbles at some distance. According to that, there is an attractive force between neighboring bubbles of similar sizes and oscillation phases. The attraction force between bubbles becomes stronger at closer distances. As a result, the secondary Bjerknes force can become more dominant than the first Bjerknes force and leads to coalescence of bubbles.

The Bjerknes forces as shown in Fig. 2.9 refer to weakly driven bubbles. If the driving pressure gets higher, the volume oscillations become nonlinear, and the Blake threshold phenomenon plays a certain role. In particular, the strongly expanding bubbles remain expanded for longer than the weakly oscillating ones, and the time average of the forces

can change sign. This is illustrated in Fig. 2.10, where just the sign of the primary Bjerknes force in a standing wave is marked by colour in a plane of bubble size and driving pressure amplitude. One can see that at 20 kHz and pressures beyond about 180 kPa, nearly all bubbles are driven out of the pressure antinode. Only at pressures below about 10 kPa, the linear ("textbook") notion is recovered where *all* bubbles below resonance radius (here about 150 μm) are attracted by the antinode.

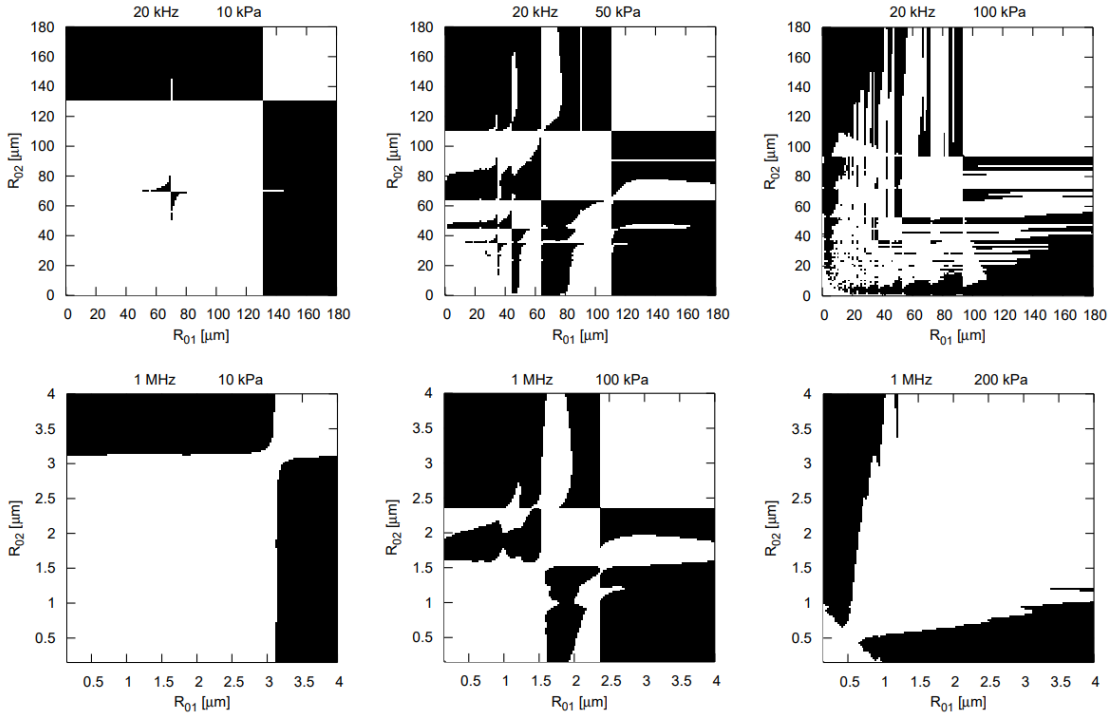

Figure 2.11. Secondary Bjerknes forces between bubbles of different size for driving frequencies of 20 kHz (top) and 1 MHz (bottom); increasing pressures are indicated from left to right. The direction of forces is marked by the colour: white regions show attraction between bubbles, dark regions repulsion. Figure from [67].

The nonlinearity also influences the secondary Bjerknes force for strongly driven bubbles, and the attraction-repulsion patterns between bubbles can become quite involved; see Fig. 2.11. Again, the linear notion where the resonance radius is separating attractive and repulsive regions is recovered only for rather low driving pressures.

2.2 Sonochemistry

Sonochemistry refers to the enhancement or altering of a chemical reaction and mass transfer in a liquid exposed to an ultrasonic wave. It is possible to achieve many different types of chemical reactions with ultrasonic cavitation. Numerous studies have been reported on ultrasound assisted homogeneous and heterogeneous chemical reactions, such as depolymerization [69], addition [70], esterification [71], ethylation [72], and alkylation [73]. Not only for advantages over other energy sources, but also for essential contribution to green science, sonochemistry has attracted considerably attention of researchers

$$H_2O \longrightarrow H^\bullet + HO^\bullet$$

$$O_2 \longrightarrow O + O$$

Scheme 2.1. Radical formation by ultrasound (sonolysis) and dissolved O_2

$$H^\bullet + H^\bullet \longrightarrow H_2$$

$$HO^\bullet + HO^\bullet \longrightarrow H_2O_2$$

Scheme 2.2. Formation of hydrogen and hydrogen peroxide

from various areas and utilized in widespread applications; such as, synthesis of nanomaterials, modifications and synthesis of inorganic materials, wastewater treatment, basic activation of enzymes, preparation of catalysts [74, 75, 76]. Sonochemistry provides handling less toxic precursors and solvents, enhancement of reaction kinetics, less energy need for chemical transformations, no toxic waste or side products, and recyclability of materials [76].

There are many parameters affecting the collapse of a bubble, and implicitly sonochemical activity, such as acoustic frequency and power, physio-chemical properties of the liquid content, external temperature and pressure, etc. Bubble collapse causes extremely high, localized temperature and pressure spots which generate so-called high energy micro-reactors. They dramatically increase reaction kinetics or facilitate molecular fragmentation of the gas content of the bubble interior. Although there are well-documented explanations for certain chemical reactions, there is no exact expressions combining overall parameters and clarifying the mechanism of sonochemistry [77] . Nonetheless, the adiabatic bubble collapse as of a simpler case, makes the temperature and pressure calculation possible as follows [36, 47];

$$T_{max} = \frac{T_0 P_a(\gamma - 1)}{P_\nu}, \quad P_{max} = P_\gamma [\frac{P_a(\gamma - 1)}{P_\nu}]^{(\gamma/\gamma - 1)} \tag{2.27}$$

where, T_0 is the liquid temperature, P_a is the acoustic pressure, γ is the ratio of specific heats of gas or vapor in the bubble interior, P_ν is the vapor pressure of the solvent. It must be noted that estimations on the temperature and pressure change during collapse are not precise since chemical reactions lead to high temperatures.

Sonolysis of Water

As water is exposed to relatively high energy, homolytic bond cleavage (homolysis) takes place, which forms radicals in the liquids. This process is called *sonoylsis*, if the driving energy source is cavitation. Predicting or simplifying chemical reaction mechanisms inside a collapsing bubble is a very challenging task [78]. Yet, one can assume a sonochemical reaction taking place homogeneously and express the fundamental reactions. In homogeneous sonochemistry, chemical reactions are induced by radicals, as a result of homogeneous sonolysis. Scheme 2.1 shows the formation of $H^\bullet$ and $HO^\bullet$ radicals, and the dissolution of O_2 by ultrasound [79]. These free radicals can possibly produce hydrogen and hydrogen peroxide [Scheme 2.2].

$$H^{\bullet} + O_2 \longrightarrow HOO^{\bullet}$$

$$HOO^{\bullet} + HOO^{\bullet} \longrightarrow H_2O_2 + O_2$$

Scheme 2.3. Formation of $HO_2^{\bullet}$ and hydrogen peroxide

$$H_2 \longrightarrow H^{\bullet} + H^{\bullet}$$

$$H_2O \longrightarrow H^{\bullet} + HO^{\bullet}$$

$$H_2 + HO^{\bullet} \longrightarrow H_2O + H^{\bullet}$$

Scheme 2.4. Formation of H_2 and hydrogen peroxide

In the presence of a solvent, molecules and ions of the solvent create bonds with water molecules. Water containing such dissolved species inside is called *aqueous solutions*. As the aqueous solution is irradiated by ultrasound, radicals combine with solute molecules which results in *oxidation/reduction (redox) reactions* [80].

Some particular dissolved gasses affect the sonolysis of water, because the free radicals also tend to recombine. For instance, the existence of oxygen slows down the rate of recombination of radicals. That means, if the sonicated water contains oxygen, a relatively high amount of hydrogen peroxide is produced [Scheme 2.3] [81]. On the other hand, if there is hydrogen, present H atoms suppress the oxidation reactions. H atoms can be produced in two different ways. Either H_2 bonds are disassociated by cavitation, within the existence of some noble gases (*i.e.* Ar), or combination of H_2 and $HO^{\bullet}$ [Scheme 2.4].

2.2.1 Sonoluminescence

Luminescence is the emission of visible photons from an excited electronic state of molecular species as a result of absorption of energy from an external source. Depending on the stimulant, the type of luminescence changes; such as, thermoluminescence, mechanoluminescence, bioluminescence, chemiluminescence and so on. As its very name signifies, *sonoluminescence (SL)* is the light emitted from a liquid as a result of cavitation by ultrasound.

SL was first observed by Marinesco and Trillat in 1933 [82]; yet, it is not clear whether they understood that the light emission was the result of cavitation, or not. After that, in 1935, Frenzel and Schultes showed that the light emission is the result of irradiation of water by intense ultrasonic waves [83]. Since then, enormous numbers of studies have been reported and many models have been developed in order to construe the origin of the light emission. However, there are still some unsolved problems under discussion. For instance, the existence of a shock-wave, the amount of water, and the temperature in a collapsing bubble, or the bubble fusion are considerably challenging research subjects. [84].

2.2.1.1 Theories of sonoluminescence

SL is emitted at the pressure antinode of a standing sound field, where the bubble collapse occurs. A single pulsing bubble can levitate steadily for hours, and SL emission is synchronized with the frequency of the ultrasound. If the suitable resonators are employed and favorable experimental conditions are set, a dim stable glow from even a single bubble can be observed by the unaided eye. This *star in a jar* has been an intriguing topic for scientists from different fields [85]. While there is somehow a general consensus about some form and modification of the Rayleigh-Plesset equation explaining the bubble collapse, none of the models defining mechanisms of SL emission have built any consensus yet. In 1996, Glanz reported a short review on the status of the possible explanations and noted "... ideas about what could be producing the light have proliferated, and the list now includes imploding shock waves, jets of liquid crashing into the bubble wall, tiny electric sparks, and radiation torn from the background fluctuations of empty space"[86].

Historically, theoretical models were always assuming the simplest case of a single bubble in an infinite liquid with an isolated environment. On the other hand, the technological limitations were only allowing the controlled experiments on a cloud of bubbles; since the capturing, controlling, and observing of a single, stably levitating, isolated bubble needs strict experimental requirements. Although cavitation has been studied at least for a decade [27], and first observations of SL from bubble clouds date back to 1930's [82], luminescence emission from a single bubble was observed for the first time in 90's [87, 88]. Not only the instrumental limitations, but also the complex nature of the SL mechanism leads to inaccurate and/or irreproducible measurements; thus, even very fundamental and key observations have been under discussion for a long while. For instance, the correlation between the phase of acoustic cycle and the moment of light flashes have been investigated in the course of years. However, several authors reported that instrumental arbitrary shifts were resulting in inconsistent results [89]. Hence, the phase of bubble volume oscillations were used to determine the moment of flashes, instead of the phase of the sound field. Afterwards, volume oscillations were measured by Meyer and Kutruff [90], using flash photography; then, by Negishi using light scatter [91]; and later, by Gaitan [87], using a sophisticated time-resolved measurement setup.

2.2.1.1.a Mechanochemical theory

One of the first models puts forward is *triboluminescent theory* which explains the luminescence emission from many crystals as a result of a breakdown of the quasi-crystalline structure by chrushing [92]. On the basis of this theory, Weyl and Marboe suggested that luminescence is a result of recombination of ions which are generated by dissociation of molecules when the quasi-crystalline structure is distorted by the surface of a growing bubble [93]. Regarding their hypothesis, the simplest reaction resulting in luminescence can be given as:

$$\mathrm{A} + \mathrm{B} \longrightarrow \mathrm{AB} + \nu$$
$$\mathrm{A} + \mathrm{B} + \mathrm{C} \longrightarrow \mathrm{AB}^* + \mathrm{C} \quad \textit{or} \quad \mathrm{AB} + \mathrm{C}^*$$

Scheme 2.5. Luminescence emission (** represents excited state of a molecule*)

However, the fact that SL occurs during the collapse of a bubble was reported for the first time by Meyer and Kuttruff in 1959 [90]. Even though, the hypothesis of Weyl and Marboe was construed later on and the possible chains of chemical reactions resulting in luminescence during collapse phase of a bubble were discussed by Saksena and Nyborg in 1970 [94]; as Jarman [95] reported, there are more plausible conjectures explaining the luminescence emitted in visible spectrum.

2.2.1.1.b The electrical discharge theories

Early investigations on electrical theories was based on the Lenard effect (also known as *balloelectric effect*) which is the formation of negative electrical charges in water due to the destruction of a water surface by spraying water droplets. This effect also explained the negative electricity in waterfalls and fountains where water splashes [96]. Based on this theory, in 1939, Harvey postulated that the source of luminescence are the electrical charges on the walls of a collapsing bubble [97]. He proposed that surface charges are uniformly distributed in a spherical bubble, thus, the field intensity inside is zero and for a bubble to collapse, there should be a very high intensity field during the compression. Frenkel has also proposed an electrical model [98]. In his *microdischarge* hypothesis, it is assumed that cavitation causes non-compensated charges of opposite sign due to fluctuations of the ion distribution around the surface of the lens-shaped cavity. However, the suggested luminescence mechanism would only occur at the stage of bubble growth, whereas Meyer and Kuttruff showed that SL is emitted during collapse of a bubble [90]. Later on, some major missing points of this proposal were corrected by Nathanson [99], yet Frenkel's cavity model is still not satisfactory for a complete explanation.

On the other hand, in 1974, Degrois and Baldo [100] postulated another electrical model in which a bubble absorbs the free atoms via inside of the bubble surface. Due to the asymmetry of the absorbed charge distribution, a molecule is distorted and polarized. During bubble collapse, all kinetic energy used for molecule polarization is being concentrated until the point of discharge, which results in SL. However, Seghal and Verral have reported that their experimental observations do not support such an electrical model [101]. Suslick *et al.* also objected to the electrical model, they have put forward and claimed that the free energy released by such discharge cannot be sufficient to emit SL [102, 103].

All these electrical theories have been disfavored by time due to inconsistencies with experimental data [104, 101]. One of the latest electrical theories has been put forward by Margulis, who has discredited all previous models [105, 106]. In his new electrical model, he referred some experimental findings as the evidence in which coalescence of small bubbles form a deformed bubble larger than resonant size. A small bubble, formed close by a large one, joins into it. Margulis has asserted that charge separation takes place during the formation of a larger bubble. As the smaller bubbles are being detached from the larger one, negative charges accumulate from the larger surface to

smaller surface, while larger surface is being charged positively. A discharge between these negative and positive charges results in light emission. Despite of the experimental aspects, this new electrical model was also contested and not found to be sufficient by other authors [107, 108]. Suslick *et al.* has also reported that luminescence could also be emitted in nonpolar liquids and liquid metals, thus the origin of luminescence cannot be electrical [102]. Their experimental results disagree with Margulis' theory and any other electrical theory. They concluded that SL or sonochemical reactions can only be explained by a theory based on high temperature and pressure changes.

2.2.1.1.c The Shock-wave Model

The shock-wave model, a mechanochemical hypothesis, claims that a spherical shock-wave is formed inside a collapsing bubble, and it diverges where temperature goes up to 10^6 K. The origin of the model comes from the *triboluminescent theory* which explains the luminescence emission from many crystals as a result of a breakdown of the quasi-crystalline structure by chrushing [92, 93]. According to that theory, light emission takes place at the phase of bubble growth. In 1960, a theory of propagation of a spherical shock wave within a bubble was first mentioned by Jarman [95].

The model was reported as a study of numerical calculation according to fundamental fluid dynamics equations [109], as a justification of experimental data from Barber *et al.* who observed the pulse width of the single bubble sonoluminescence light as less than 50 psec [110]. Afterwards, studies were focused on such a scenario and researchers had started to believe in the shock wave model until the publication of Gompf *et al.* in 1997 [111]. They observed that the pulse width of the emitted light is much longer than that of reported by Barber*et al.*. Then similar experimental findings were published, and it was resulted that shock-wave model is inadequate alone to interpret the origin of SL. In short, findings support both the existence and absence of a shock wave; and even if a shock wave forms inside a bubble, it is also not very clear how it causes light emission.

2.2.1.1.d The Hot-spot Model

Since the investigation of SL emission started, temperature has always been suggested as an energy source of the process. The *hot-spot model* rests on extreme temperature and pressure changes which are based on the adiabatic heating of the gas during the bubble collapse. It was first suggested by Neppiras and Noltingk in 1951 [46]. According to that model, high temperature and pressure values are reached at the last stage of an adiabatic bubble collapse, and the thermal equilibrium of the compressed gas molecules emit black-body radiation. Since this theory has been postulated, temperatures from several thousands to millions of kelvin were claimed [109, 112, 113, 114, 115].Regarding the temperature estimation, of course the assumptions about the events inside a collapsing bubble and the predictions on a formation of SL light cannot be the same. There are many suggestions supporting the hot-spot model and explaining how bubbles glow, such as the black-body emission, the ionized gas model and the confined electron model [116, 117]

One possible mechanism is the homogeneous heating of the bubble interior in which the emission takes place via blackbody radiation [47]. Another possibility is the inhomogeneous heating and formation of and a shock wave, or a compression wave from the

inward bubble wall motion towards the bubble center. Consequently, further compression of bubble interior leads to generation of plasma [107]. In this case, Bremsstrahlung would take place. A third possibility is the occurrence of chemical reactions of the bubble components due to the high temperatures and pressures, so that the light is produced by recombination after dissociation [118].

2.2.1.2 Single and multibubble sonoluminescence

Single bubble sonoluminescence (SBSL) is the luminescence emitted from a single bubble trapped in the acoustic field, whereas multi bubble sonoluminescence (MBSL) come from multiple bubbles. The most common way to trap a bubble in the sonic field is to choose a geometry and frequency that produces only a pressure bulge in the center of the cuvette [87]. For the lowest alternating pressure amplitude at which a bubble can be trapped, the bubble oscillates spherically and slowly dissipates due to surface tension, where the liquid has been previously degassed. As the alternating pressure amplitude is increased, the bubble grows by rectified diffusion [119]. In most cases, the bubble moves around its rest position, jets, performs surface oscillations, and possibly even breaks into a multitude of small bubbles that repeatedly recombine and break apart again at the next collapse. Such bubbles do not emit light [120]. When the alternating pressure amplitude is further increased, the region of stable SBSL is reached. The bubble volume suddenly shrinks, then the bubble begins to emit light, and finally the bubble becomes stationary [121]. These transition events occur smoothly and the oscillations become stronger. The more violently the bubble collapses, the hotter it becomes while collapsing. At a certain point, the bubble interior reaches sufficient temperatures which causes most of the components of the bubble (O_2, N_2) to react chemically with each other or with the water vapor molecules, and they dissolve in the liquid. If the bubble was previously air, it shrinks until only argon remains in the bubble and light is emitted. Due to the smooth transition, it is possible to obtain SL even in water with a bubble moving erratically around the rest position, which is called m-SBSL (moving-SBSL) [122].

In SBSL, the properties of the light emission can be investigated in detail, since reproducibility and good observability are given. Among other things, the pulse durations of SBSL could be extensively investigated. They depend sensitively on the experimental parameters (ambient temperature and pressure, pressure amplitude, and type and amount of dissolved gas in the liquid) and pulse durations. The pulses occur only at the time of the minimum radius. The ratio of rest radius to maximum radius is used as a rough criterion for the occurrence of SL in oscillation. If a value of about 10 is reached in water, SL occurs [123].

In the measured spectra of SL, there are differences for SBSL and MBSL. In the case of SBSL, significantly higher mean temperatures fitted to blackbody radiation are achieved (10000 -50000 K [124, 125, 126]) than in the case of MBSL (2000-5000 K [127]). However, it is important to note that the high temperatures of the SBSL only occur when the bubble remains stationary. If it moves excursively around a zero position (m-SBSL), the maximum attainable temperature decreases and, as in the case of MBSL, emission bands can be obtained [128]. The collapse temperature apparently depends on how spherical the bubble collapse is. This case can be presented by SBSL, but not for m-SBSL and MBSL. In MBSL and m-SBSL, aspherical collapse is common and it leads to focus less

energy, that means lower collapsing temperature. Moreover, bubble undergoing some events, such as jetting as well as splitting into many small bubbles, consumes energy, and droplets of the liquid presumably mix into the interior of the bubble. Thus, such parameters should also be considered as factors resulting in small final temperature compared to SBSL.

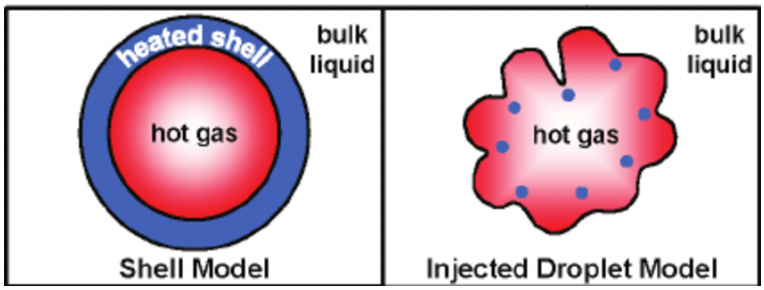

Figure 2.12. Possible mechanisms leading to excited metal atom emission from cavitation bubble: **a)** The heated shell model **b)** The injected droplet model

In case of the existence of non-volatile alkali metal ions for SBSL and MBSL, the excitation mechanism is not fully understood. Two possible mechanisms are proposed (see Fig. 2.12). The first one is the "heated-shell" and in this case, the alkali cations are reduced, heated and excited at the bubble wall. An alternative mechanism is the "droplet-injection" model [129]. Here, very small drops of liquid are introduced into the bubble by a mechanism that is not yet clear. The second mechanism proposes that surface modes of the bubble as the source of the droplets [129]. An alternative is provided by a jetting bubble. Once the nonvolatile alkali cation has entered the gas phase of the bubble, an excited neutral atom can be produced, which then falls back to the ground state by light emission. The light intensity during bubble collapse can be influenced by several factors [130]. One way to enhance the light emission is to reduce the temperature of the liquid [51]. Furthermore, the static pressure can also be increased [131]. The content of the bubble also plays a crucial role: if the liquid is saturated with noble gases, the emission can be multiplied compared to air saturation. An increase of the SL intensity by noble gases can be explained by the thermal conductivity, which is lower for noble gases than for air [132]. In addition, noble gases do not react with other components in the bubble, so that an additional energy consumption can be excluded. Another point is to dissolve luminol in water; NaOH (most commonly), or any other base regarding the recipe must be added. As a result, a higher concentration of $HO^{\bullet}$ is present in the liquid. Contamination of metal cations in the water can additionally split the water into $H^{\bullet}$ and $HO^{\bullet}$, which also leads to an enhancement of the luminescence.

2.2.1.3 Sonochemiluminescence

Sonochemiluminescence (SCL) is the glow resulting of a reaction between added chemical and radicals produced by cavitation. Bubble collapse produces hydroxyl radicals that subsequently react with molecules in the liquid. Accordingly, the light is not generated by the bubble collapse, but by a chemical reaction. The reaction with the hydroxyl radical causes the molecules in the liquid to enter an excited state, where light is emitted by falling back to the ground state. The SCL may occur later than the SL because the

molecules do not necessarily react instantaneously and emit light, but may continue in a metastable state. For the same reason, light emission may also occur at locations other than the bubble collapse, as flow in the liquid or the bubble motion may move the excited molecule to another location where it emits.

Luminol ($C_8H_7N_3O_2$) is a typical chemical used for SCL experiments. It is utilized to observe sonochemical activity, and spot the active regions in sonoreactor [133]. Possible mechanism of SCL given in Scheme2.6 which has been reported by McMurray and Wilson [77].

Luminol is a weak diprotic acid with first and second pK_a values of ∼6.3 and ∼13-15, respectively [3] [77]. pK_{a1} and pK_{a2} of luminol correspond to the hydrazide hydrogens. In this study, the pH value of aqueous luminol solution is approximately adjusted to 10.5-11.0; hence, the predominant luminol species is luminol monoanion (**II**). Then, luminol monoanion is oxidized by sonochemically produced $HO^{\bullet}$ radicals and diazaquinone radical anion is formed (**III**). This oxidation mechanism competes with the reactions between $HO^{\bullet}$ and H_2O_2 / HO_2^- generated by ultrasound. The compounds coming out from **III**, interacts with $O_2^{\bullet}-$ and hydrogen peroxide is formed **IV**. Then, the product decomposes and eventually relaxes to the ground state of aminophthalate monoanion accompanied by blue light emission at wavelength of ∼430 nm.

2.3 Ultrasonic reactors

Since the extreme temperature and pressure conditions of acoustic cavitation were known, chemical and physical applications of it have attracted attention of researchers from various fields. Although the advantages of cavitation over conventional methods was proven, technological limitations inhibited the utilization of cavitation in a large scale industrial applications. In addition to that, the efficiency of the process was limited by some parameters of cavitation, such as acoustic impedance, mixing, heating, streaming, erosion and sound field attenuation. Although individual characteristics and trends of such parameters are generally known, optimum combinations of those differ from one sonoreactor to another. Due to this complex nature of cavitation, and technological restrictions, large scale industrial applications are still suffering from erosion and non-uniform energy dissipation in the high power intensity reactors [134]. Therefore, numerous ultrasonic reactor designs have been reported and each has been optimized individually to achieve desired application. Different geometries of reactor designs can be divided into two general groups as batch and continuous.

2.3.1 Batch type

Batch reactors are more versatile, low cost, well-known and simpler designs with respect to their continuous counterparts. The reactors having a batch geometry are ultrasonic bath reactors, ultrasonic sonotrode-based batch reactors and ultrasonic cup-horn reac-

[3] pK_a is a number indicating the strength of an acid, and it is negative base-10 logarithm of K_a given as $pK_a = [A^-][H^+]/[HA]$; where K_a is the acid dissociation constant, $[A^-]$ is the concentration of the conjugate base of the acid, $[H^+]$ is the concentration of hydrogen ions, and $[HA]$ is the concentration of chemical species HA. The lower the pK_a value, the stronger the acid.

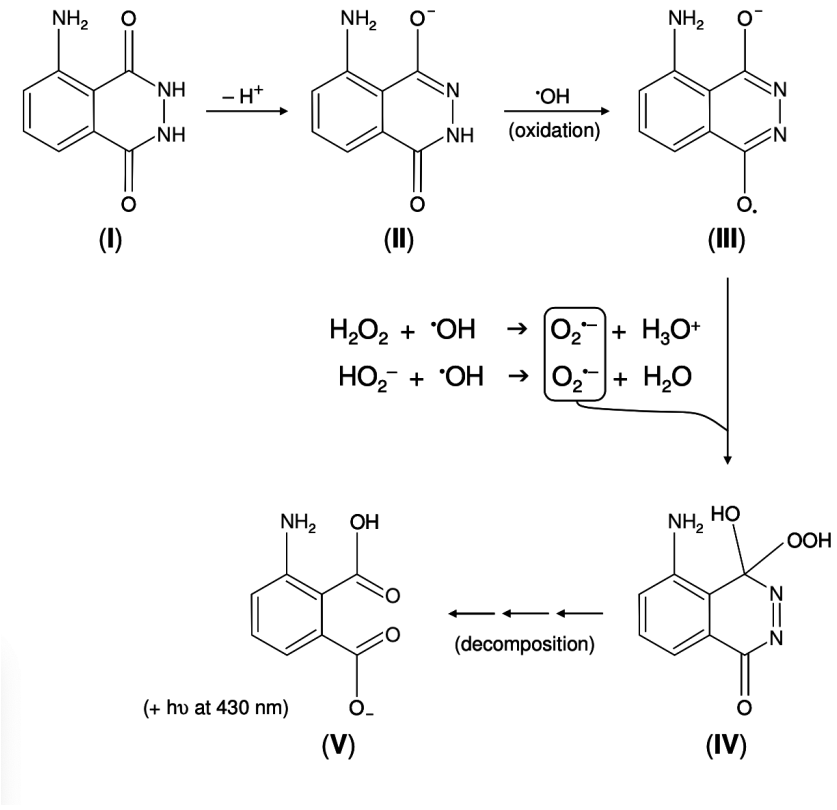

Scheme 2.6. Reaction pathway of SCL emission from luminol solution at pH∼10.5 [77]. Oxidation of luminol monoanion by the sonochemically generated $HO^{\bullet}$ results in a bright blue light emission at 430 nm.

tors. In the simplest case of an ultrasonic bath, ultrasound transducers are mounted on the side and/or bottom walls of a rectangular-shaped container (Fig. 2.13).

Ultrasonic bath reactors are very suitable and convenient for small scale applications requiring a low energy density. They are mostly employed for cleaning [135], electrodeposition [136], water treatment [137], and synthesis [138]. Larger scale of ultrasonic baths are utilized with high power intensities for cleaning in automative, electroplating, plastic, and food industries [134].

Previously, these baths were manufactured to perform sonication between 20 kHz to 40 kHz. However, low frequency operations for several hours are considered as a risk for human safety in regard to audible limit (20 kHz) [23]. Today, they operate mostly at around 40 kHz or beyond, yet, avoiding noise exposure (i.e. wearing ear protection) during operation is still advised. The commercial ultrasonic baths can also be modified and fabricated depending on the purpose of the customer. For example, in Fig. 2.14, different baths with an immersed stack of ultrasonic transducers are shown. Such sonoreactors offer an application dependent transducer selection by size and frequency, an easy exchange of a desired transducer, and a higher cavitation activity inside the bath.

Ultrasonic sonotrode-based batch reactors have a similar design to an ultrasonic bath

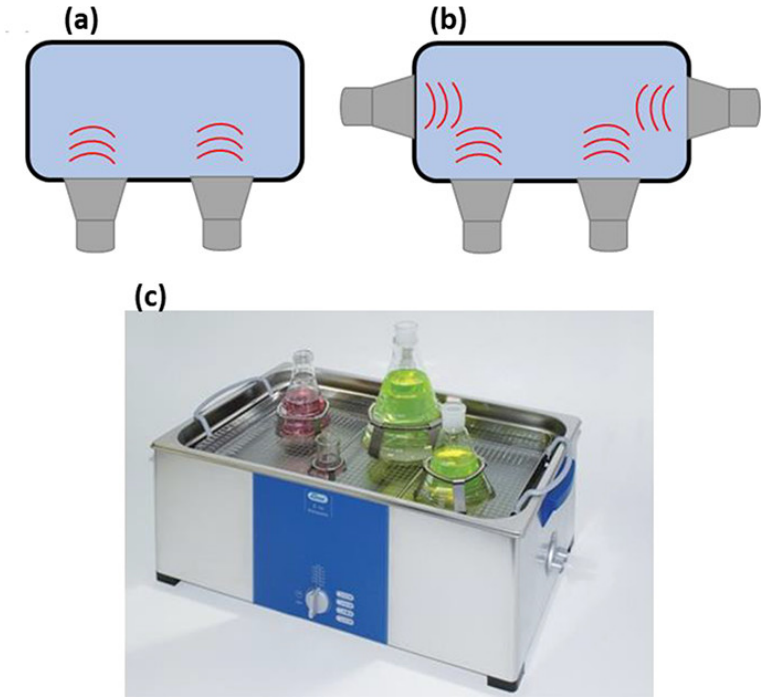

Figure 2.13. Ultrasonic transducers are attached to **a)** the bottom walls, and **b)** both bottom and side walls. **c)** Lab-scale ultrasound bath. (source: [134])

reactors. However, a sonotrode-based design targets a high local cavitation intensity which is almost up to 100 times higher than in an ultrasonic bath. In sonotrodes, a transducer is connected to a metal rod which is known as ultrasonic horn. Therefore, while the transducer is being kept away from the reaction medium, a sonotrode concentrates the acoustic energy. Material, volume and shape of the container, as well as liquid height and displacement of the horn are essential parameters for the reaction to be achieved while designing such reactors. Some sonotrodes are designed in a way that the horn can be changeable depending on the application. This also allows to replace the horn whose tip eventually gets damaged after a while due to temperature, pH and cavitation.

Over the course of years, many sonotrode shapes have been designed, such as linear, cone, stepped, circular, and airbone depending on the application medium (single, or multiphase) and purpose; hence sonotrode-based reactors in various geometries are available in the market. Despite their various advantages, not only the replaceable tip of the horn, but also the degradation of a sonotrode by long time usage in large scale industrial applications is still one of the major drawbacks [139]. Moreover, uncontrolled heating of the medium is another problem depending on the physio-chemical properties of the liquid and volume. A possible solution is usually a cooling system which can be adapted externally, like a cooling bath or a cryogenic circulation jacket [140].

The ultrasonic cup-horn reactors are simply a type of sonotrode designs. Similar to the sonotrode-based reactors, the cup-horn transducer is displaced inside the container most often from the bottom. The container is filled with a liquid, but this liquid does not have to be the reaction medium. It can also used as a transmitting medium for the reaction

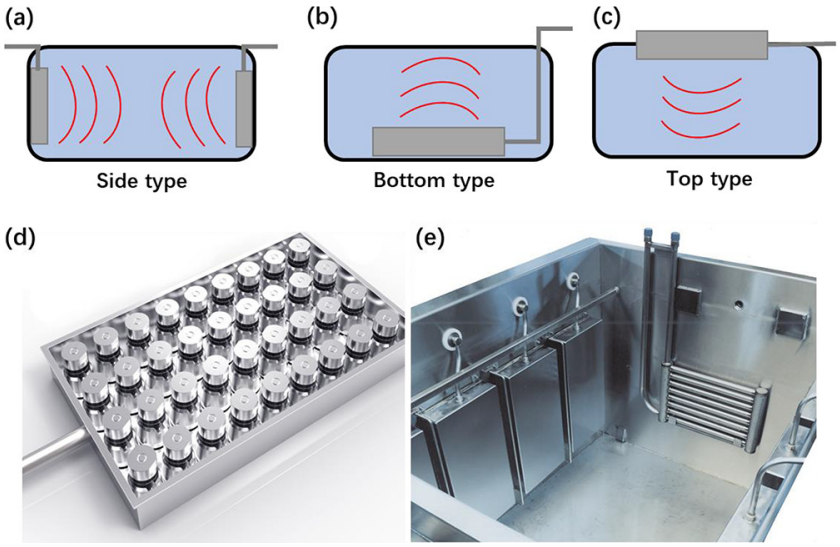

Figure 2.14. Ultrasonic transducers are attached to **a, b, c)** different possible positioning of immersed transducers, **d)** stack of transducers, **e)** large scale industrial bath with immersed ultrasound transducers on side walls (source: [134])

vessel, and such reactors are called indirect cup-horn reactors (Fig. 2.15).

Cup-horn based batch reactors offer almost 50 times more energy intensity than ultrasonic bath reactors, whereas they provide less energy dissipation to the liquid than sonotrode ones due to their larger emission surfaces. However, a larger surface also leads to a smaller tendency of degradation, therefore the cup-horn reactors are very advantageous to utilize in extraction of trace metals from complex matrices [141]. Such applications mostly involve strong acids to extract and leach noble metals (i.e. Au, Ag), the ultrasonic cup-horn offers a very quick and efficient processing with low chemical waste, cost and sample loss. [142].

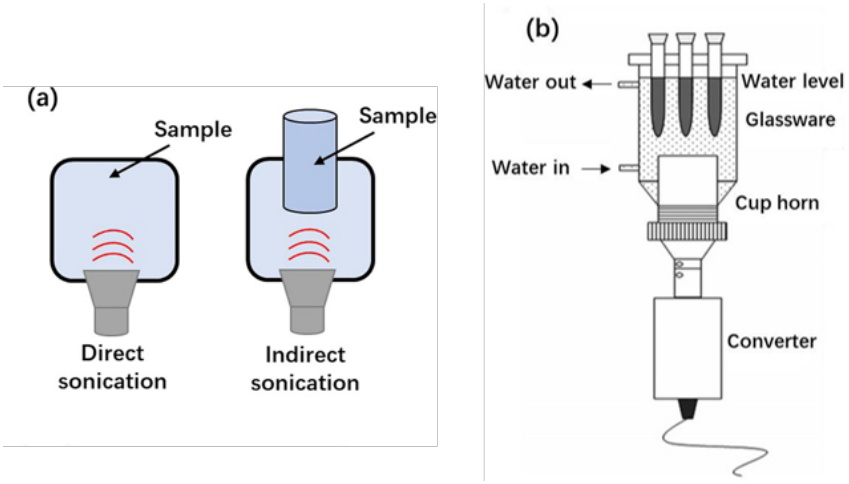

Figure 2.15. **a)** A simple schematic of a cup-horn based batch reactor with direct and indirect sonication, **b)** Indirect cup-horn sonotrode reactor with multiple sample vessels

2.3.2 Contiuous (Flow) ultrasonic reactors

Continuous reactors, also known as flow reactors, are utilized in *process intensification (PI)* which has been an innovative technology in fine-chemicals and pharmaceutical industries in the last decade. PI aims to increase the product quality, lower the waste and energy consumption, increase the efficient use of raw materials and better control over the process [1]. As long as the chemical reaction conditions allow, using continuous reactors is very advantageous over their batch counterparts. There are different flow designs equipped with ultrasonic transducers depending on the feasibility of the processing.

For continuous reactors, controlled flow is the common essential factor in obtaining high efficiency. In case of a water flow through any chambers or tubes, as ultrasound is applied, laminar flow always turns into a turbulent one. Therefore, a homogeneous environment for optimum reaction kinetics can only be achieved by a detailed characterization. Flow parameters of the operation vary depending on many different factors, such as reactor volume and design, cavitation properties (i.e. ultrasound frequency and power), dynamics of the fluid, solid content of the liquid, and so on. All variables have to be characterized and optimized with respect to each individual application.

2.3.2.1 Continuous reactors with emitting walls

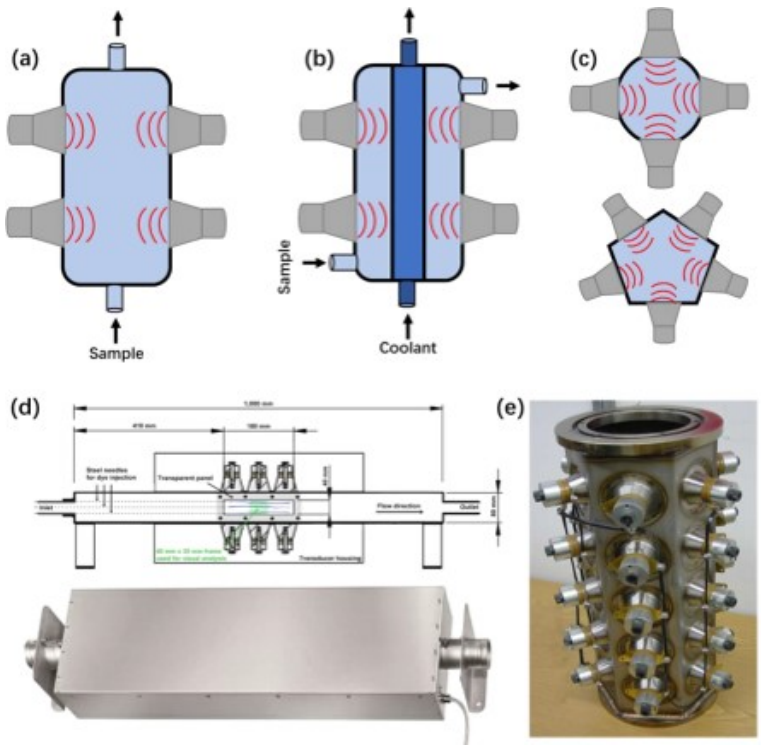

Figure 2.16. A simple schematic of emission walls **a**) without cooling system, **b**) with cooling system. **c**) A diagram of cross-sectional, cylindrical and hexagonal tubular emission walls **d**) Design of a flow reactor with emitting walls with 6 transducers (BANDELIN Electronic GmbH & Co. KG, Berlin, Germany) **e**) Hexagonal tubular emitting walls with 5 transducers in each surface with an adjustable frequencies of 20 kHz and 40 kHz (KLN Ultraschall AG, Germany).

In these reactors, arrays of ultrasonic transducers are mounted to the walls of cylindrical or polygonal shape a tubular reaction chamber (Fig. 2.16.a-c). Tubular flow reactors are commercially available and can be externally integrated to an existing setup. Additionally, a suitable cooling system can be easily attached to it.

The displacement of the cavitation concentration is one of an important parameters of emitting wall reactor design. In order to prevent the deformation of the surfaces of the tubing wall and the transducers as much as possible, the cavitation intensity in the middle of the tube is preferably focused into the middle of the tubing instead somewhere near the walls. Since the cylindrical tubular reactors reflect the sound field better than the polygonal ones, they are a more promising equipment by their lifetime. Another factor of transducer positioning is to provide the uniform cavitation. Homogeneity of mixing and heating are the key parameters of the chemical reactions in the first place. Therefore, transducers have to be attached in a configuration, that allows cavitation inside the chamber to be uniform at each point. Apart from positioning, the number of the transducers to be employed is crucial to achieve the optimum power for the efficiency of the process. For this purpose, there are designs offering dual frequencies (Fig. 2.16.e).

2.3.2.2 Continuous reactors equipped with sonotrodes

Continuous reactors equipped with sonotrodes combine high intensity and well-focused ultrasound features of sonotrodes, and the advantages of flow processing. As previously noted, sonotrodes have been manufactured in different geometries, hence, wide ranging designs of flow reactors utilizing sonotrodes are commercially available. The reactors can be equipped with multiple sonotrodes at different frequencies with an adjustable power option. They can operate 24h/7d depending on the application and process more volume of product than their batch counterparts [143]. Some examples of industrial scale flow sonoreactors, designed in accordance with the desired chemical reactions, are given in Fig. 2.17.

It also has to be mentioned that microwave combined ultrasonic flow reactors are also commercially available. The combination of ultrasound and microwave enables the application of different energy levels in a single system which allows selective transformation in organic synthesis and catalysis. Hence, both research laboratories and industries show great interest to their synergistic effect. In such reactors, there are two different chambers, one is equipped with an ultrasonic horn, the other one is simply a microwave oven, and the mixture can circulate through the chambers by a pump [144].

2.3.2.3 Continuous ultrasonic microreactors

Apart from the large scale counterparts, micro-structured continuous reactors are prominent chemical processing systems in the last decades within the increasing trend in researches on PI [8]. Due to the characteristics of a high surface-volume ratio and an enhancement in mixing by internal circulation, microreactors offer an increase in heat and mass transfer coefficients and enhancement in efficiency of energy conversion. These reactors are also cost efficient and environmentally friendly, as a result of their small volumes, fewer and less equipment requirements, lower energy consumption, safer handling of hazardous chemicals, ease of controlling the reactions taking place at high pressures

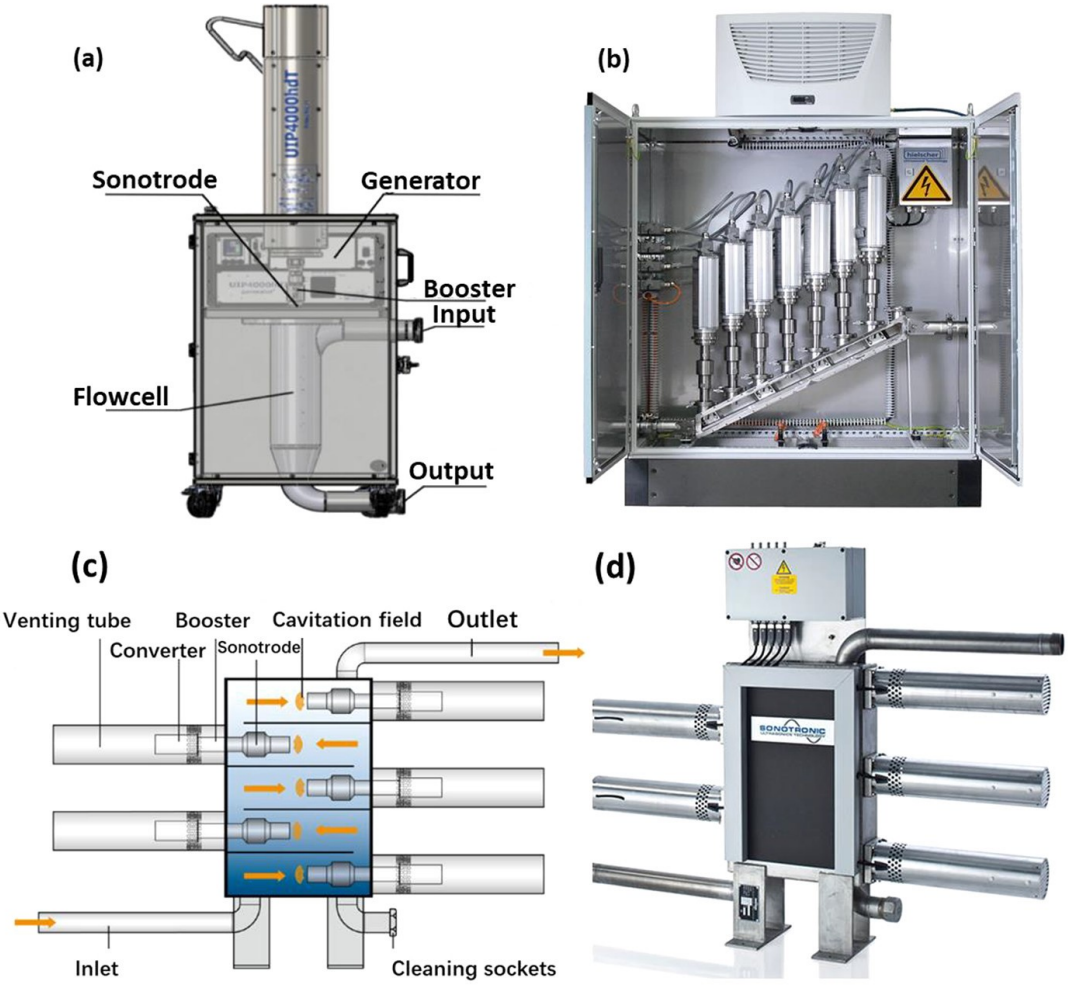

Figure 2.17. Industrial continuous sonoreactors employed with sonotrode: **a**) Continuous sonoreactor with a single sonotrode in a closed system (Hielscher Ultrasonics GmbH), **b**) Industrial continous reactor employed with 7 identical sonotrodes, which can provide power between 1000 and 16000 W for waste-solid water treatment., **c**,d) Schematic drawing and the image of full scale continous sonoreactor (ULTRAWAVES Water and Environmental Technologies, Hamburg, Germany). [134]

and temperatures [4].

The developments on microreactors have been focusing on utilizing an alternative energy source which is non-classical, non-contact, and sustainable; such as microwaves, plasma radiation, electrostatic fields, and ultrasound [145]. In this study, we use ultrasound as an energy source in order to initiate and/or enhance the chemical reaction (*sonochemistry* through flow channels, see Sec. 2.2). Ultrasonic flow microreactors are constructed as reactors with a channel size of a few millimeters or less. They are mostly used in small scale or laboratory applications, but yet they have the advantages of industrial flow reactors in comparison to the batch counterparts. One of the most common limitation of ultrasonic assisted processing systems used in high purity required applications, such as pharmaceutical or food industries, are the corrosion of the sonotrode horns which is directly in contact with the reaction medium [134]. Degradation of the horn causes the contamination of the product by metallic residues. On the other hand, microreactors

offer the advantage of indirect sonication of a reaction medium in a closed system without any contamination.

The numerous structures of microreactors have been designed for different types of sonochemical reactions; such as, direct contact method of flow tube and Langevin transducer for liquid liquid extraction [13] and gas-liquid mass transducer intensification [14], polydimethylsiloxane-based microfluidic reactor using piezo ceramic for radical formation [11], teflon stack microreactor with piezoelectric actuator [7] or microchannels on top of Langevin transducer [15] for handling solid forming reactions, a horn transducer attached milichannels for crystallization of acetylsalicylic acid [18].

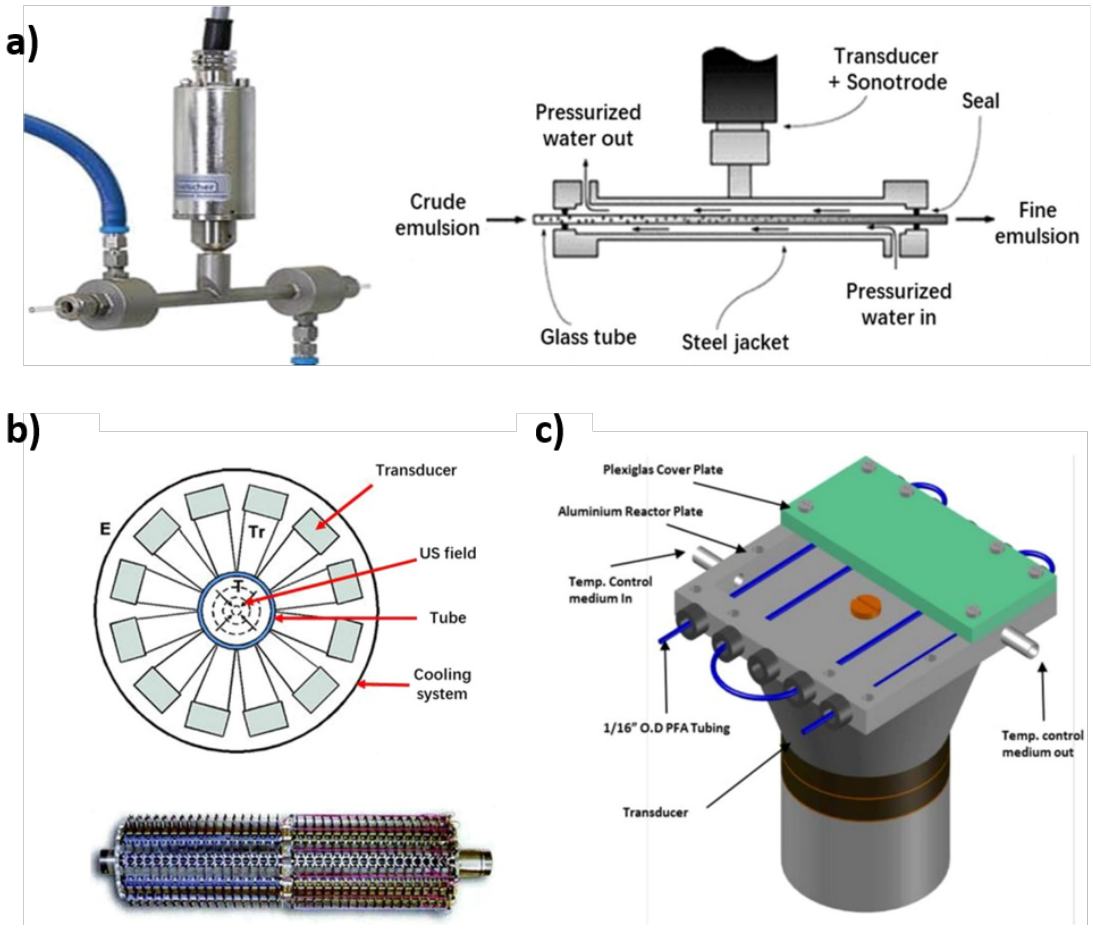

Figure 2.18. Industrial continuous micro-sonoreactors employed with different type of transducers: **a**) An ultrasonic flow cell and it's schematic drawing on the right, **b**) Cross-section and the core/reaction chamber of SonerTec sonoreactor, **c**) Reaction channels on top of an ultrasonic transducer for liquid-liquid extraction. [134]

Figure 2.18 represents ultrasonic microreactors employing different types of transducers and channel materials designed according to the desired sonochemical reactions to be performed. In Fig. 2.18.a, a simple design of a microreactor utilized with a single reaction channel and ultrasonic horn is shown [146]. This flow-through microreactor has a glass tube as a reaction chamber with an inner diameter of 2 mm, and is surrounded with a cylindrical steel jacket. The reaction takes place inside the glass flow tube, and

there is no contact, neither with the sonotrode nor the atmosphere. In order to control the reaction temperature, there is circulating water between the glass tube and the steel jacket that the sonotrode is mounted onto. This kind of flow microreactor can be used for the synthesis of high purity products, both in large and laboratory scales. In Fig. 2.18.b, a patented design employed with a cylindrical sonotrode is represented [147]. The reactor consists of many (typically 4 to 16) electroacoustic cylindrical transducers displaced radially around the reaction tube made of polytetrafluoroethylene. The liquid is circulated through the tube, and acoustic cavitation is focused in the middle. The whole system is sealed, both the reaction chamber and the transducers; hence, not only the temperature, but also the pressure inside the chamber can be controlled. The reactor shown in Fig. 2.18.c is designed by John *et al.* for temperature controlled liquid-liquid extraction [13]. Perfluoroalkoxy alkane microchannels of 0.8 mm inner diameter are placed on top of an aluminum plate which has grids, and plexiglass is mounted on top of the microchannels. Channels are irradiated by a Langevin type of transducer indirectly. Liquid flow through the channels is applied via a syringe pump.

Among these many different designs, the most practical setup from an experimental perspective is used in this study, which is to submerge transparent flow channels into an ultrasonic bath. Such a setup has advantages of easy installation, long residence times, large volume irradiation, and temperature control by coupling the (outer) liquid in the ultrasonic bath. Additionally, the setup enables visualization of cavitation bubbles and SCL signal via a transparent walls. However, it has the drawback of a large volume equipment (the bath), that causes the operation to be restricted to lower frequency ranges and lowers the energy efficiency, and is not fully stable and/or controlled. Another point is that some parameters of the bath and coupling liquid affecting the energy transfer through coupling liquid to the cavitating medium in the tube; such as, fixed position of the tubes, the height (volume), temperature and gas content of the coupling liquid. These are additional factors needed to achieve more controlled and reliable operation. This simple experimental design is yet very practical in order to obtain general information about characteristics of cavitation conditions and sonochemical activity in flow tubes. Some of the drawbacks can be overcome by some simple modifications; for instance, using less volume of coupling liquid, or utilizing higher frequency ranges. From an industrial point of view, it offers simple and feasible testing conditions for new or modified sonochemical reactions in flow tubes. It has the potential to be scaled up by numbering-up the lines in the bath which is rather simple and cost effective considering the general problems of the transition from laboratory to industrial scale [148].

2.3.2.4 Fundamentals of Laminar Flow

Flows exhibiting highly regular motion and smooth streamlines are called *laminar*, whereas flows highly disordered and having velocity fluctuations are classified as *turbulent*. The transition from laminar to turbulent flow depends on many parameters, such as the properties of the fluid itself, flow velocity, geometry, surface properties and so on. Among all these, the ratio of inertial forces to viscous forces is the main factor of transition and expressed by Reynolds number: $Re = (\rho V_{avg} D)/\mu$, where ρ is the density,

V_{avg} is the average velocity [4] ,D is the characteristic dimension of the device (diameter; in case of a rounded tube), and μ is the absolute dynamic viscosity of the fluid. For large Re numbers, inertial forces are higher than viscous forces; thus, fluctuations in the liquid cannot be prevented and the flow is said to be turbulent. If the Re number is small or relatively moderate then laminar flow is attained, as viscous forces are capable of suppressing the fluctuations and keep the flow in-line.

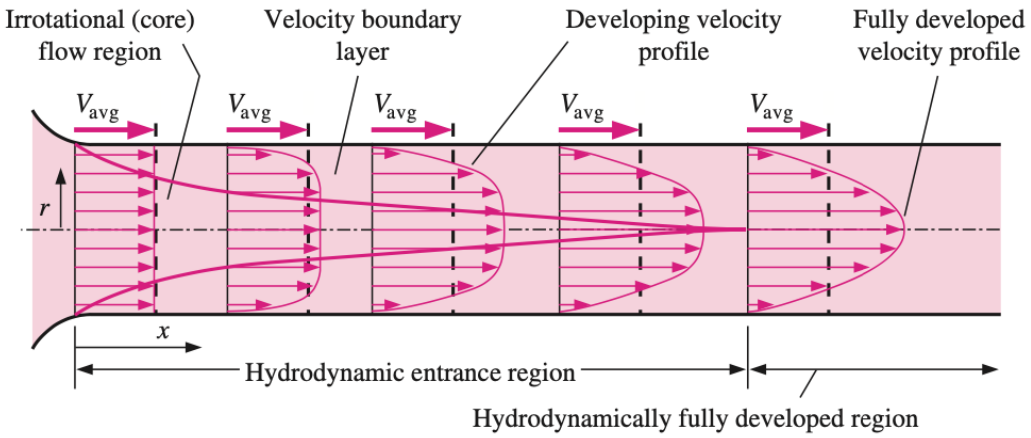

Figure 2.19. Development of velocity boundary layer in a circular pipe. The average velocity for laminar flow exhibits a parabolic profile [149].

As a fluid with a uniform velocity enters a circular pipe (see Figure 2.19),the particles of fluid in contact with the surface of the tube wall will slow down and fully stop due to the non-slip condition. These particles form a layer resulting in friction. To recover the velocity loss, the middle section of the flow has to increase the velocity to maintain a constant mass flow rate which results in a velocity gradient along the tubes. The region affected by viscous shearing forces due to fluid velocity is called *(velocity) boundary layer*; and *irrotational flow region* refers to the section in which frictional effects are negligible and velocity is constant in the radial direction. The region from where flow enters the tube and develops, until it merges at the center is called *hydrodynamic entrance region*. Until the velocity profile is completely developed, thickness of the boundary layer increases in the flow direction. As there is no change in V_{avg}, the velocity profile is said to be *hydrodynamically fully developed*. If the normalized temperature profile is also unchanged, then the flow is called *fully developed*. A fully developed laminar flow has a parabolic velocity profile as shown in Fig. 2.19.

In flow reactor designs, the most fundamental condition is the steady laminar flow of an incompressible fluid in the fully developed region in circular channels/ tubes. In this regard, supplying liquid into a channel (*i.e.* pump) in order to maintain the flow brings the *pressure drop* (ΔP) parameter along it. The pressure drop in laminar flow is:

[4] V_{avg} is the average speed through a cross-section. Due to the non-slip condition ($V_{wall} = V_{fluid}$), the fluid velocity is zero at the points touching the surface of the tube, and maximum at the center of the tube. V_{avg} remains constant as long as the fluid is incompressible and the cross-sectional area of the tube is constant.

$$\Delta P = P_1 - P_2 = \frac{32\mu L V_{avg}}{D^2} \tag{2.28}$$

The equation represents the pressure loss ΔP when a fluid with viscosity of μ flows into a channel of constant diameter D and the length L passed through via velocity of V_{avg}. This means that the lower the viscosity of the fluid (*i.e.* friction), the smaller the pressure drop. Once the pressure drop is known, the volume flow rate of laminar flow along a horizontal channel of constant diameter can be calculated;

$$Q = V_{avg} A_c = \frac{\Delta P D^2}{32\mu L} A_c = \frac{\Delta P \pi D^4}{128\mu L} \tag{2.29}$$

where A_c is the cross-sectional area for the circular channel ($A_c = \pi D^2/4$). Eq. 2.29 is known as *Poiseuille's law*, and this type of flow is called *Hagen-Poiseuille flow*. Eq. 2.29 expresses the dependence of the pressure drop on the viscosity of fluid, the diameter and length of channel; doubling the diameter of the channel can reduce the pumping power by a factor of 16.

Regimes of Gas-Liquid Two-Phase Flow

A multiphase flow refers to the simultaneous flow of materials, at least two of which are in different phases. There are two distinct phases which can be a combination of gas, liquid and solid particles. The most common two-phase flows in microchannels are gas-liquid (GL) and liquid-liquid (LL) flows due to their use in widespread practical applications, such as pharmaceutical, biomedical, engineering and some commercial purposes. The behaviour of a two-phase flow in a channel is determined by interaction and distribution of both phases. Distribution of phases are classified as flow regimes or flow patterns. In micro/milliflow reactor design, characterizing flow regime is the first step to optimize the channel size and operating conditions.[5] One of the most fundamental steps of analyzing a flow is to determine the flow regime which is strongly affecting the thermohydraulic properties of a flow, such as the heat transfer rate and the pressure drop. There are many definitions and dimensionless parameters to describe the configuration of a flow [151]. It has to be noted that flow regimes in microchannels are similar to those that take place in relatively larger diameter channels, with the exception of stratified flow. Flow is generally laminar in microchannels. As the diameter of the channel increases, instabilities are observed in the laminar flow regime due to inertial effects. Hence, stratified flow is not observed in flow regimes of microchannels.

Fig. 2.20 depicts a schematic of flow regimes of GL phase flow regimes in channels. Material, geometrical details, and configuration of the channel; properties, velocity and wetting effects of phases are predominant factors affecting the flow in microchannels. There are five main flow regimes; bubbly, slug, churn, slug-annular and annular. In a bubbly flow regime (Fig. 2.20.a.), bubbles are distributed and able to move through

[5]Flow characteristics of milli- and micro-sized channels show significant differences. Dimensions of millichannels are larger than the molecular free path (O (10^{-8}) m for gas). Hence, the Kundsen number which is the ratio of molecular mean free path to characteristic dimension of the flow becomes very small, then the continuum assumption applies. On the other hand, as the channel size is reduced (*e.g.* submicrons), some other parameters begin to affect the flow characteristics; such as slip at the channel wall, viscous energy dissipation and an electric double layer [150]. In the context of this study, characteristics of flow regimes discussed in this section correspond to relatively larger micro-, and millichannels.

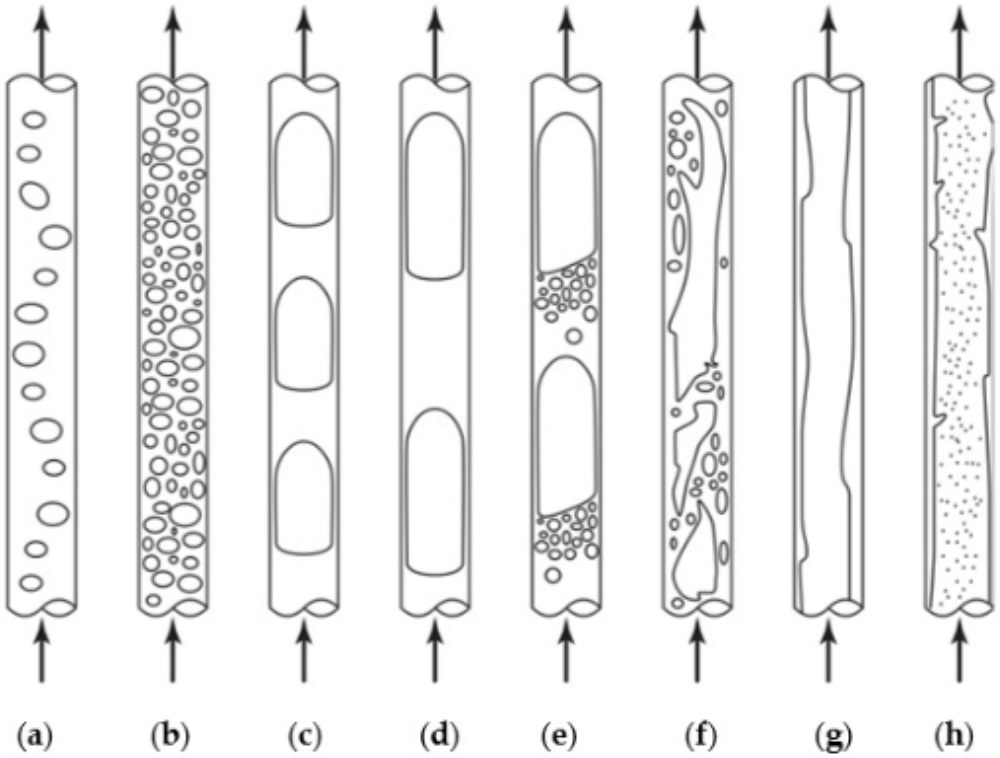

Figure 2.20. The schematic of GL flow regimes in the vertical channels. **a,b)** bubbly flow, **c,d)** Taylor, or segmented flow **e)** transitional flow slug to churn **f)** churn flow **g)** annular-film flow **h)** mist-annular, or wispy- annular flow. Retrieved from [152]

the liquid phase at a low superficial velocity. As the bubble is small, bubble-bubble interaction is negligible. On the other hand, an increase in gas to liquid volumetric flow rate leads to split and the coalescence of bubbles as shown in Fig. 2.20.b. If the volumetric flow rate is further increased, the coalescence of bubbles turns into a dominant event, and consequently large bubbles are formed. These bubbles are surrounded by a thin liquid film and have the characteristic bullet shape of a Taylor flow (Fig. 2.20.c-d.). This flow regime is also known as slug, segmented, plug, bolus or intermittent flow [153]. As gas to liquid volumetric flow rate is continued to be enhanced, small dispersed bubbles start to form in the liquid phase. As a result, transition between slug to churn flow takes place (Fig. 2.20.e.). In the churn flow regime, a variety of bubble lengths and irregular gas plugs are formed (Fig. 2.20.f.). This chaotic regime occurs as the flow velocity is increased. In such a case, both the disperse and the carrier phases are not continuous anymore. For larger-sized channels, this chaotic flow behaviour is much more remarkable. This regime is also called semi-annular or unstable-slug flow. In annular flow, an increase in gas velocity causes the formation of a liquid thin film on the walls of the channel (Fig. 2.20.g.). If there are small liquid phase droplets in the core of the gas phase, then it is called mist flow pattern (Fig. 2.20.h.). It has also be noted that the material of the channels has a high impact on the formation and the boundaries of flow patterns, whereas the inlet junction type (*e.g.* T or Y) has negligible effect [154].

2.3.2.5 Effect of cavitation on continuous microreactors

Continuous microreactors are designed to perform chemical reactions using flow chemistry. Combining these reactors with ultrasound offers a higher achievement and ease of complex microfluidic reactions and operations. Cavitation bubbles can be utilized to generate a flow or enable optimization of the flow dynamics by mixing [155], pumping [9], switching [156] and sorting [157] along the tube or channel.

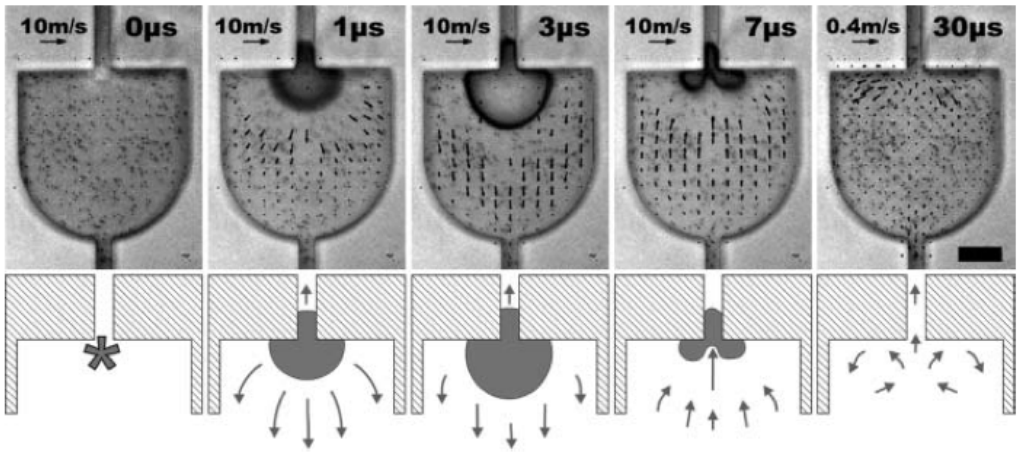

Figure 2.21. Working principle of micropumping via a single bubble. A configuration consists of a single bubble in a microfluidic chamber *below* and a channel *on top* where the liquid is pushed into. The frames captured during pumping are given on top, and the corresponding sketches are depicted below. The arrows show the velocity vectors of the flow field. From the first to the last frame, respectively: Inception of a bubble, bubble expansion, bubble at maximum radius, jet formation, vanishing of the bubble [158].

Effective and rapid mixing is one of the major parameters taken into account for microchannel design. For larger volumes, mixing low viscous and miscible fluids is a relatively simple process. Turbulent eddies favor the entrainment of liquids, and molecular diffusion takes place at large interfacial areas. In the case of microfluidics, even at relatively high velocities, surface forces keep the flow laminar; that means turbulence is most likely not attainable due to very small Re numbers, particularly for high-viscosity fluids. Therefore, mixing is typically dominated by the diffusion which is limited to take place only on small interfacial areas. However, diffusion based mixing is very inefficient and generally takes a long time, especially for the liquids containing macromolecules or large particles (e.g. bacteria, enzymes) which have diffusivity coefficients lower than that of the solution itself [159]. In order to achieve rapid, homogeneous and efficient mixing, there are various ways to implement eddies into microfluidics. Numerous *microfluidic mixers* have been reported in the past decade by using different approaches; such as optical [160], magnetic [161], hydrodynamic [162], electrokinetic [163] and so on. Among all, *acoustofluidic micromixers* are rather advantageous because they offer more efficient, homogeneous and faster mixing of even high-viscosity fluids [155] and depending on the design, cavitation can also provide stirring. There are many different ways reported to implement acoustics into micro and millifluidic systems; for instance,

generating a flow by a single bubble[164], bubble-induced acoustic streaming [159], flow chamber micromixing via acoustic waves [165].

There are also microchannel designs in which cavitation bubbles are employed for pumping purposes. The mechanisms of the expansion and the collapsing of bubbles are used to move the fluid towards a desired direction [158]. Although, various configurations have been reported to implement cavitation into microfluidic systems to achieve *micropumping*, a general trend focuses on developing a microchip which consists of a microfluidic chamber, and a channel[12]. A fully expanded bubble is generated at the exit of a narrow channel which is smaller than the chamber dimensions (See Fig. 2.21). Such a bubble exhibits the similar dynamical behavior to a bubble standing next to a rigid boundary. While the bubble expands, some liquid is pushed into the channel; and the liquid is sucked back during an early collapse. As a jet is formed, liquid is pushed again into the chamber [9].

Chapter 3

Materials and Methods

In this chapter, the design and operation of experimental setups with a high-speed camera to investigate cavitation conditions, as well as synchronous experimental methods to observe sonochemiluminescence (SCL), are described.

3.1 Experimental Setups

3.1.1 Channels on top of transducer

Reactor Design

A schematic drawing of the channels contacting the ultrasound transducer is shown in Fig. 3.1. In this design, an aluminum plate measuring 70 x 70 mm with a thickness of 5 mm is mounted on top of the Langevin transducer (Elmasonic, Germany) using glue. The bottom of the bath is made of stainless steel with a thickness of 1.5 mm and is bolted to the polycarbonate walls. Perfluoroalkoxy alkane (PFA), an inert and hydrophobic polymer, was selected as the tubing material. PFA tubing has a low bending radius, which allows for ease of use in a wide range of designs, and provides a transparent and clear view for observing the events occurring inside. The outer diameter of the PFA tubing (BOLA, Germany) employed in this design is d_o=1/32" (≈1.58 mm), while the inside diameter is d_i=1/16" (≈0.8 mm). The tubing is held in place by the channels in a 5 mm thick polycarbonate top plate that is screwed onto the aluminum plate from the corners. Polycarbonate offers high transparency for imaging and is a sound-soft material, making it durable during ultrasound applications.

Two syringe pumps (ProSense, Multi-Phaser™NE-500, The Netherlands) are utilized to alternatively supply the aqueous solution (i.e., luminol solution) and air from the inlet side through a T-junction, while the outlet side remains open. The pumps work synchronously to create a regular gap of air and a slug of aqueous solution with a desired phase ratio by switching. During the ultrasound exposure, the slugs and air gaps undergo distortion due to mass exchange caused by droplet ejection and air entrainment.

Experimental procedure The experimental setup is depicted in Fig. 3.2. The characteristics of the ultrasound waves are controlled using a frequency generator (Tektronix AFG 3021, USA) and applied through a power amplifier (E&I Ltd., 1040 L, USA) via a home-made impedance matching box. The reactor surface is illuminated by an intense continuous wave (cw) light source (Sumita LS-352A, Japan). To capture the

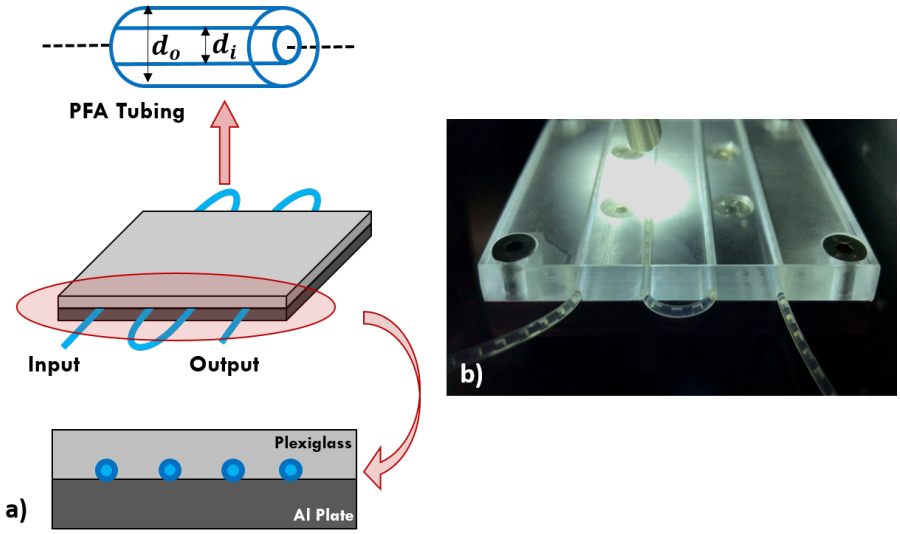

Figure 3.1. **a)** Cross-sectional configuration of PFA channels with an inner diameter of d_i=1/16" (∼0.8mm). **b)** Photograph from the top view of the reactor plate showing the slug flow of liquid and air.

reflected light and visualize the cavitation bubbles inside the tubing, a high-speed camera (Photron, Fastcam SA5, Japan) is positioned perpendicular to the reactor, equipped with a long-distance microscope attachment (K2/SC, Infinity, USA). The luminescence emissions are observed using a digital SLR camera (Nikon D700, Japan) in a dark room condition. The acoustic pressure maps are obtained using a calibrated hydrophone (Brüel & Kjaer 8103, Denmark).

3.1.2 Submerged flow channels

In this section, two setups for submerging flow channels are described. While the reaction bath remains the same, the sonication conditions and the configuration of the flow tubes differ between the setups. Additionally, the cameras used for high-speed recordings and luminescence observations, the pumping system for supplying liquid and/or liquid-air into the tubes, and the equipment for driving and controlling ultrasound have been previously explained in the experimental procedure section of the direct contact design (see Section 3.1.1). Therefore, in this section, only the reactor designs will be provided.

3.1.2.1 Submerged loop tubes

A schematic drawing of the flow channels submerged in the ultrasonic bath is presented in Fig. 3.3. The bath is constructed with polycarbonate walls measuring 140 x 50 x 150 mm^3 and is open at the top. It is mounted on top of two Langevin transducers (Elmasonic, Germany) using a steel plate, with only one of the transducers being utilized while the other remains unused. A comprehensive investigation of the cavitation structures in the bath under various conditions was previously documented by Reuter *et al.* [60]. In this experiment, the bath is subjected to sonication at a frequency of 27.2 kHz with an

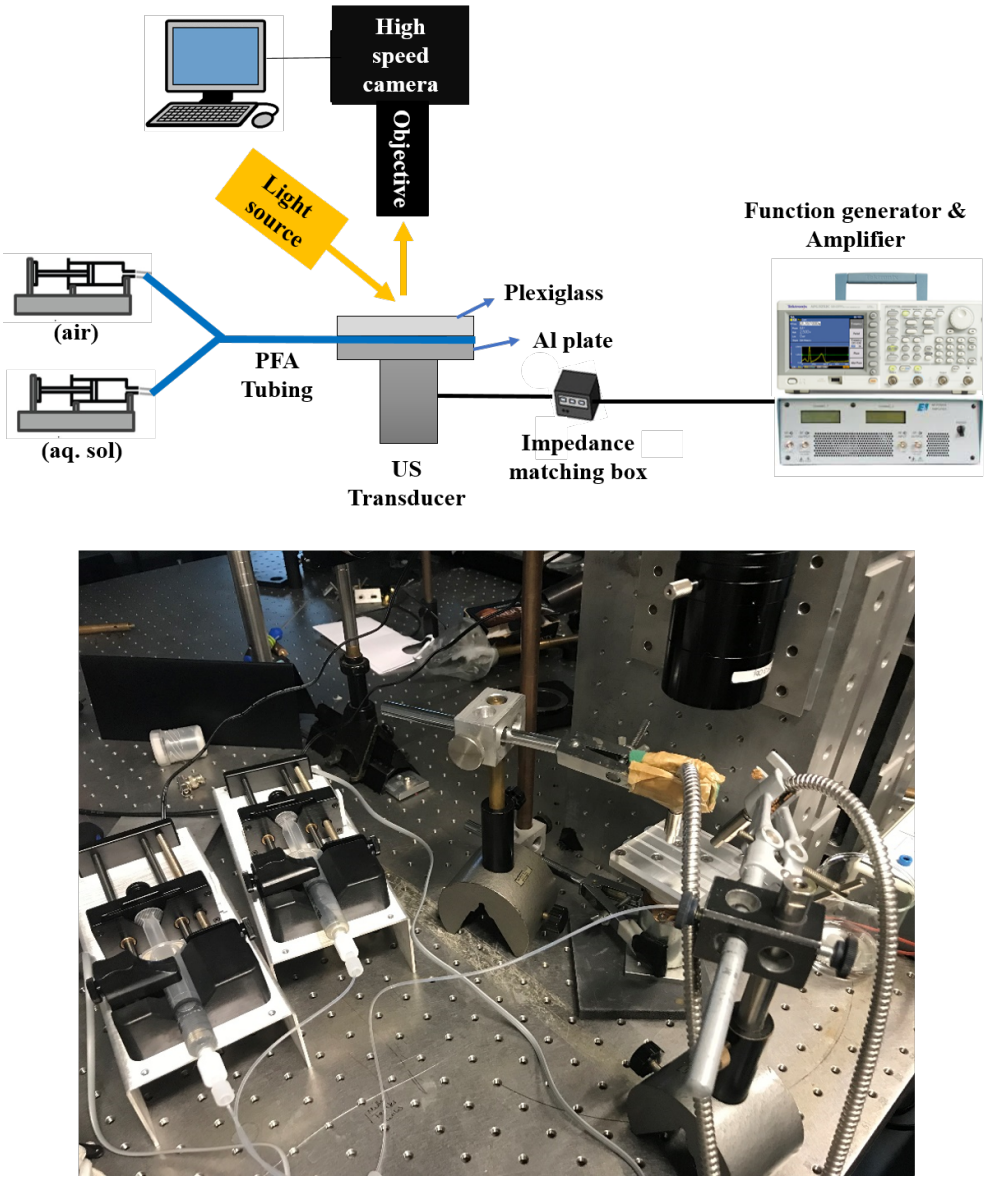

Figure 3.2. Schematic representation and photo of the experimental setup for the direct contact reactor. Liquid-air segmented flow is formed by alternating pumping in the channels. Sonication is performed at different frequencies ranging from 25 kHz to 52 kHz. The channels are illuminated by an intense light source to collect the reflected light from the aluminum plate on which the channels are placed. Visualization of bubbles inside the channels is achieved using a high-speed camera with a long-distance microscope.

applied power of approximately 65 W.

The bath is filled to a height of 60 mm with degassed distilled water, and the previously described PFA tubing (with an inner diameter of approximately ∼0.8 mm) is submerged in the ultrasonic bath, forming three loops with a diameter of approximately 50 mm. These loops are fixed in a stable position slightly above the steel plate, along the center of the transducer. For the purpose of observing both cavitation and SCL, air gaps and

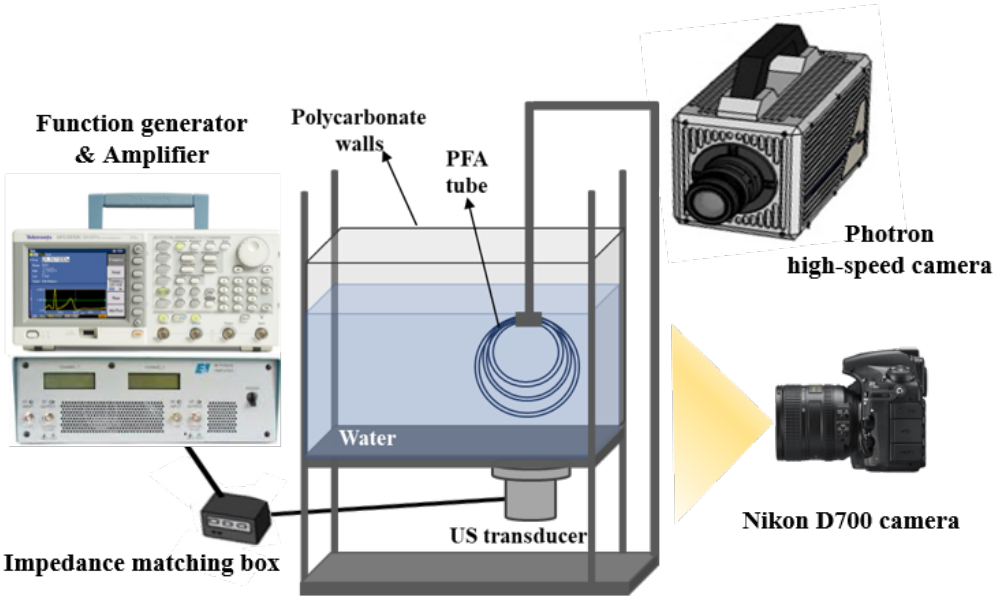

Figure 3.3. Schematic drawing of the loop channels submerged into ultrasonic bath. The PFA channels are filled with alternating air and luminol solution using pumps, and the flow is then stopped. The ultrasonic transducer is driven at a frequency of 27.2 kHz. The cavitation bubbles inside the tubes are recorded using a high-speed camera with a long-distance microscope attachment, while the luminescence emission is captured by a digital SLR camera.

luminol slugs are created within the tubing, and the pumps are halted to maintain the stability of the air and luminol in their respective positions. Alternatively, the interior of the tubes can be visualized using a long-distance microscope with a high-speed camera and appropriate illumination.

3.1.2.2 Submerged stacked tubes

Channels are also submerged into the same ultrasonic bath with the help of a polycarbonate holder as shown in Fig. 3.4 to have horizontal and stable lines at different heights. The ultrasonic bath is filled up to 11 cm and degassed distilled water is used as the coupling liquid. As the bath is sonicated, not only the liquid inside the channels but also the coupling liquid (*i.e.* water) inside the ultrasonic bath cavitates. These outer bubbles block the view of the bubbles inside the tube and restrict observing cavitation conditions. Therefore, water is degassed to reduce the cavitation activity inside the bath and observe the activity inside the tube more efficiently. The bath is sonicated at 25.7 kHz with alternating amplitudes. Different than the previous experimental setups, here a halogen lamp (Nikon Halogen D-LH, 100 W, Japan) is used to enlighten the channels to capture bubbles via scattered light, instead of using the previously mentioned intense cw light source and collect reflected light to visualize the bubbles.

Channels are also submerged into the same ultrasonic bath using a polycarbonate holder, as depicted in Fig. 3.4, to achieve horizontal and stable lines at different heights. The ultrasonic bath is filled up to a level of 11 cm, and degassed distilled water is used as the coupling liquid. During sonication of the bath, not only does the liquid inside

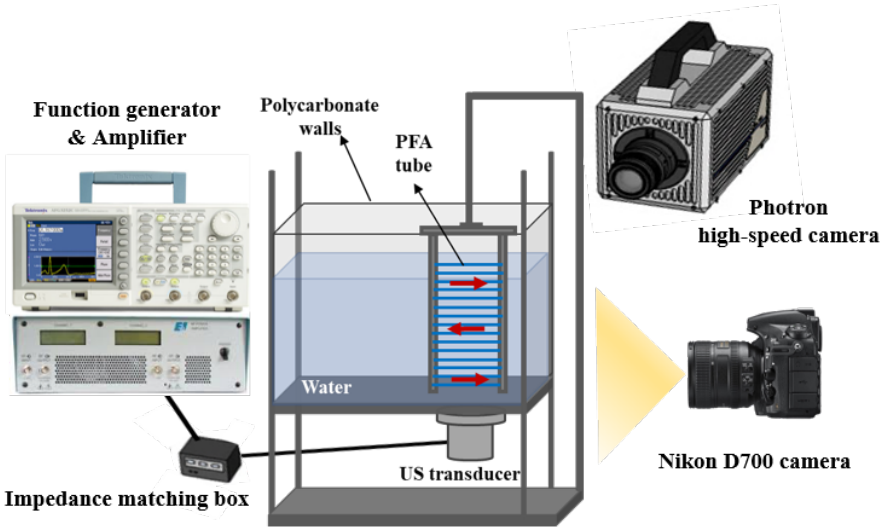

Figure 3.4. Schematic drawing of channels submerged into ultrasonic bath via polycarbonate holder. The U-shaped polycarbonate holder is submerged into the bath in an inverted position, with its open end facing downwards, along the center of the transducer. The transducer is operated at a frequency of 25.7 kHz. A high-speed camera equipped with a long-distance microscope is used to record the cavitation bubbles inside the channels, while a digital SLR camera is employed to capture the luminescence emission.

the channels cavitate, but the coupling liquid (*i.e.* water) in the ultrasonic bath also undergoes cavitation. These external bubbles obstruct the view of the bubbles inside the tubes and limit the observation of cavitation conditions. Therefore, the water is degassed to reduce the cavitation activity within the bath and enables a more efficient observation of activity inside the tubes. The bath is sonicated at a frequency of 25.7 kHz with alternating amplitudes.

In contrast to the previous experimental setups, a halogen lamp (Nikon Halogen D-LH, 100 W, Japan) is used here to illuminate the channels and capture bubbles via scattered light. This approach differs from using the previously mentioned intense continuous wave (cw) light source and collecting reflected light to visualize the bubbles. A photo of the stacked channels in the ultrasonic bath is presented in Fig. 3.5. The U-shaped channel holder is constructed from 10 mm thick polycarbonate and has dimensions of 35 x 70 x 200 mm^3. It features holes of ~1.6 mm along each of its long edges and can accommodate 39 lines of PFA tubing, each approximately 90 mm in length. The holder is aligned through the center of the transducer from its short side, submerged in the ultrasonic bath as an inverse U-shape, and positioned slightly above the steel plate. This U-shaped holder allows the channels to be positioned directly close to the surface of the bath.

3.2 Sonochemiluminescence measurements

3.2.1 Preparation of the luminol solution

For all the SCL measurements, a 0.1 mM aqueous solution of luminol is prepared. Luminol (3-Aminophthalhydrazide; 98%, Fluka, USA) is dissolved in deionized water at room

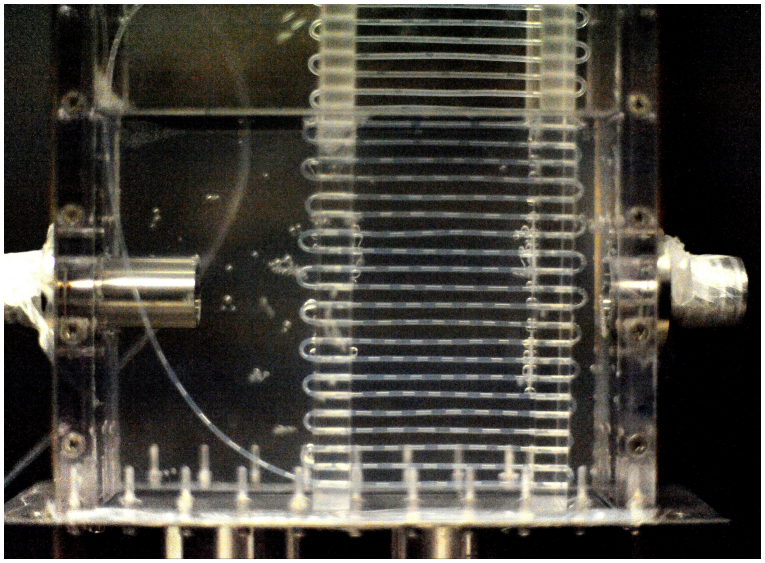

Figure 3.5. Stacked channels configuration. PFA tubing is arranged horizontally in lines using a polycarbonate holder with holes on each side. The stacked channels are positioned in the ultrasonic bath along the center of the transducer surface. The bath is filled with degassed water up to a height of 11 cm. The channels directly face the bottom of the bath without any medium in between.

temperature, and the pH is adjusted to approximately 11.5 by adding a NaOH solution (32 wt.%, Atotech, Germany). While there are several other methods for preparing luminol solutions that result in varying brightness and quenching times, this particular recipe was found to be more efficient due to its reasonably high brightness, which is crucial for luminescence observation from small volumes. The SCL emission is captured using a digital SLR camera (Nikon D700, Japan) with a long exposure time of 30 seconds under dark room conditions.

3.2.2 Enhancement of luminescence intensity

To assess the intensity of the luminescence emission, a glass cuvette measuring 30 x 30 x 70 mm^3 is submerged in the water-filled ultrasonic bath. The cuvette is used for testing purposes. It is filled with 25 mL of the luminol solution with a concentration of 0.1 mM. The ultrasonic bath is sonicated at a frequency of 25.7 kHz with an applied power of ∼80 W. The experimental setup for testing the luminol solution is illustrated in Fig. 3.6.
Since the molarity of the luminol solution is not as effective as changes in pH and the addition of alkali compounds [77], the molarity of the aqueous luminol solution is kept constant at 0.1 mM, and the optimum pH value of the solution is determined. Solutions with different pH values are prepared, and the SCL emission from solutions with pH 12.2 and pH 11.3 is shown in Fig. 3.7.a and 3.7.b, respectively.

The brightest emission is obtained from the luminol solution with a pH of 11.3. It has been reported that depending on the sonication parameters, conditions, and the addition of alkali metal and basic solutions, the maximum intensity of SCL emitted from the luminol solution should have a pH value between 11 and 13 [77]. However, since the diameter of the tube used in this study is 0.8 mm, which holds a small volume of liquid,

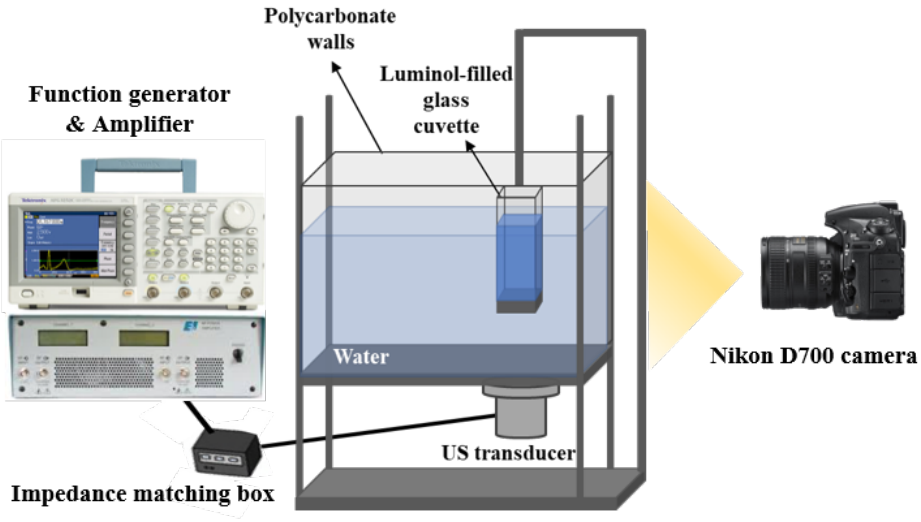

Figure 3.6. Testing the SCL intensity. A glass cuvette with the dimensions of 30 x 30 x 70 mm^3 is submerged into an ultrasonic bath. The cuvette is filled with an aqueous luminol solution.

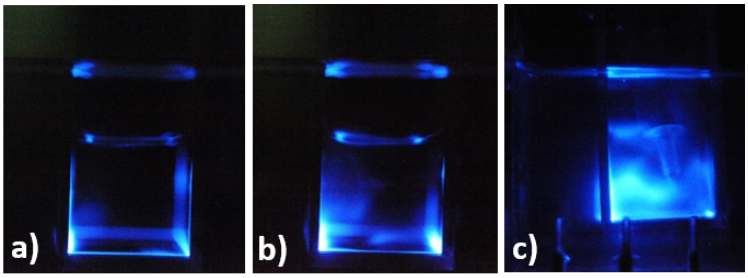

Figure 3.7. SCL emission from a glass cuvette filled with 0.1 mM luminol solution at different pH values.**a)** pH=12.2, **b)** pH=11.4. **c)** Enhancement of SCL intensity by Ar gas. Images obtained in dark room conditions with a 30-second exposure time using an SLR camera. The water-filled ultrasonic bath is sonicated at 25.7 kHz with an applied power of ∼80 W.

the SCL intensity is expected to be weak. Therefore, in order to observe the sonochemical activity inside the flow tubes, the SCL intensity is enhanced. As mentioned before, it is known that the presence of noble gases (e.g., Ar, Xe, Kr) increases the intensity of the SCL emission [132]. Hence, a continuous flow of Ar gas is provided into the luminol solution, and the light emission is captured under dark room conditions with a 30-second exposure time. A dramatic increase in luminescence intensity is observed (Fig. 3.7.c).

After optimizing the pH value and molarity of the luminol solution, a closed gassing and degassing setup was designed for a more consistent experimental procedure (Fig.3.8). The system allows degassing and gassing of the solution without disconnecting and contaminating the solution. Therefore, it is designed to be gas-tight, and vacuum-resistant flexible silicon tubes are used. A 0.1 mM luminol solution with a pH of ∼11.4 is poured into a glass container that has three gas-tight caps. One cap is used for pouring and placing a magnetic spin bar, while the other two caps are used as gas inlets and outlets. The magnetic stirrer is always kept on for more efficient operation. A vacuum pump and an Ar gas tank are connected to the gas line via a 3-way stopcock, which

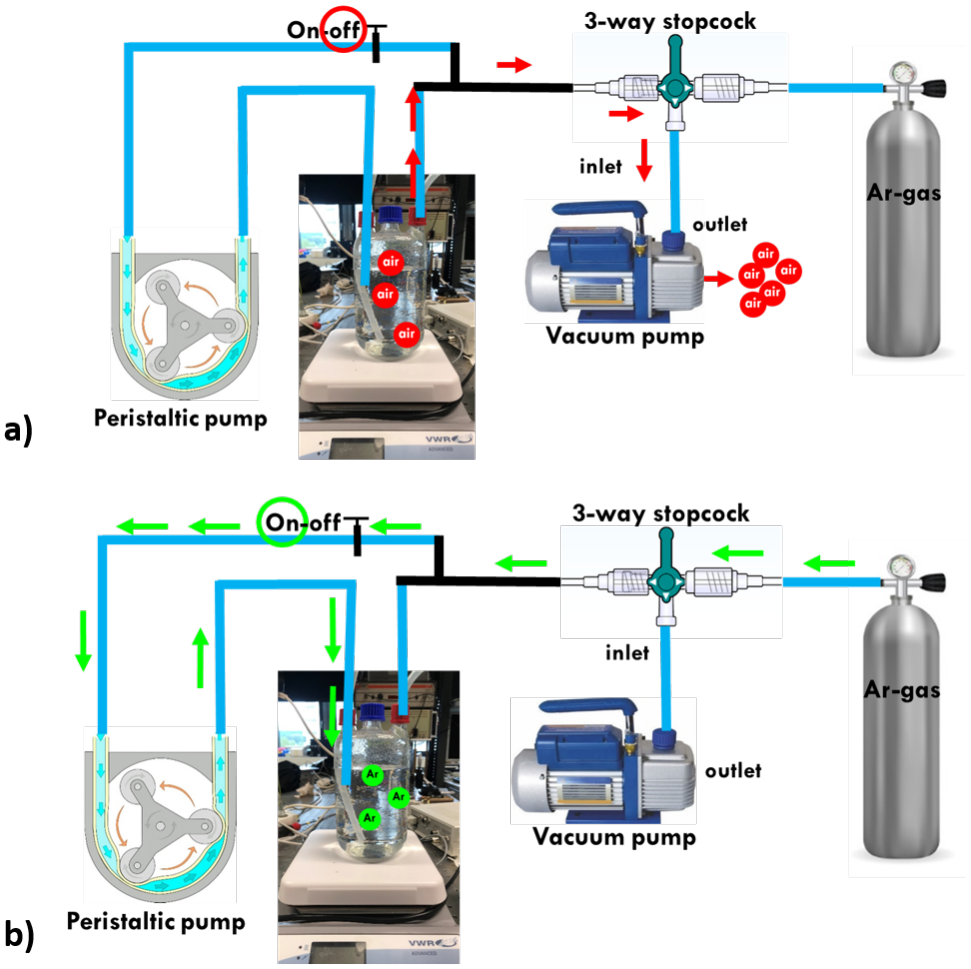

Figure 3.8. The configuration of closed system for **a)**degassing, and **b)** Ar-gassing

allows the direction of gas flow to be chosen. First, for degassing, the vacuum pump (MZ 2C NT, Vacuubrand GmBH, Germany), which is a diaphragm pump providing an ultimate vacuum of 7 mbar, is run for 30 minutes. Then with the help of the 3-way stopcock, the vacuum pump is turned off and subsequently, Ar gas is pumped. Ar-gas passes through a peristaltic pump (Masterflex L/S 7518-00, Germany). which supplies a regular gas flow via positive displacement into the container without any contamination. Similarly, distilled water used as a coupling liquid in the ultrasonic bath is also degassed for 30 minutes before each set of experiments to reduce cavitation activity inside the bath, allowing for better visualization of the flow tubes.

Chapter 4

Results

4.1 Channels on top of transducer

Flow channels placed in between an aluminium plate and a polycarbonate are subjected to the ultrasound by direct contact with the transducer without the presence of a liquid medium. The full picture of the design and the experimental setup are given in Section 3.1.1. This design has been first reported by John *et al.* and is called *direct contact method* [13].

The image from a water-air flow through the channel obtained in the silent condition is given in Fig. 4.1.a. The image is obtained by using an intense CW-light source, and the reflected light is collected by a high-speed camera equipped with a long-distance microscope. The round illuminated area is the reflection of an aluminum plate located under the channels. Water-air slug flow is formed regularly inside the PFA channel (d_i= 0.8 mm) in the direction from right to left, and the average flow rate is calculated as $\sim 7\,\mu$L/s. In the channel, a white region in a rectangular form corresponds to a water slug. On the other hand, air pockets appear as black regions on each water slug. It is seen that the liquid-gas shape of the boundaries on each side is different from each other. The front end of the water slug has a neater shape than the other ending. Fundamentally, one of the main reasons is the flow property. Generally speaking, slug formation is dependent on the regime and direction of flow. Here, a two-phase Taylor/ segmented flow is applied through the channel. In that case, air pockets are expected to be bullet-shaped (See Fig. 2.20.c-d.). According to the flow direction, the front boundary takes an elongated shape whereas the tail has a rather flat velocity profile. In the slug flow represented in Fig. 4.1.a., the water slug moves toward left; which means that from left to right it has a boundary to the tail of one gas pocket and the nose of another air pocket. Hence, the left ending of the water slug has a neater and slightly parabolic shape. Additionally, the reflection, illumination, and shape of the tube contribute to the distortion of the imaging. The light source illuminates the left side of the image slightly more than the other side which gives a rather sharp line to the left of the image. On the other hand, the metal surface leads to a strong reflection. The reflected light also makes different angles with rounded channels before reaching the microscope which leads to difficulties in evaluation. Distinguishing the channel wall can be given as an example. Around the left boundary interface, it is seen that the parallel lines on top and bottom of the air gap are the walls of the tube in thickness of ~ 0.4 mm. However, boundaries of the tube wall cannot be observed in a water slug. Fig. 4.1.b. depicts the

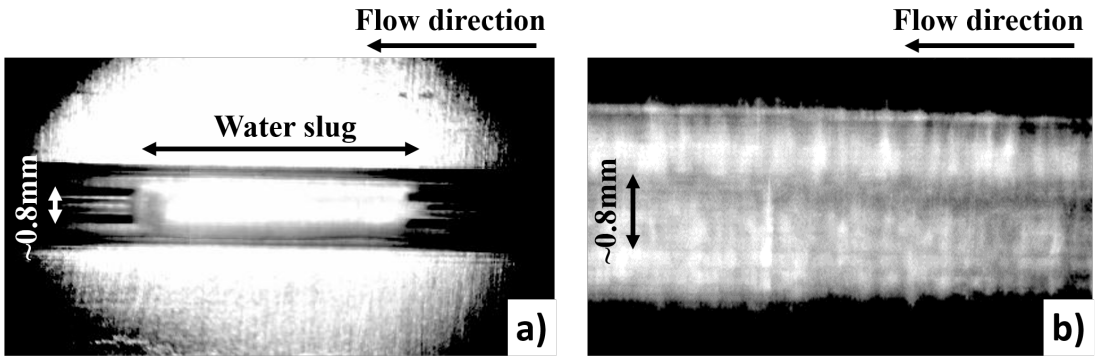

Figure 4.1. **a)** Image of the water-air flow through channel obtained in silent condition. The image is extracted from a 50 fps recording. The inner diameter of the channel is 0.8 mm and the flow rate is $\sim 7\,\mu$L/s in the direction from right to left. The round illuminated area on the background is the reflected light from the surface of the aluminium plate underneath. The water slug is seen as a white rectangle in the middle of the tube. Black regions on each side of the water slug refers to the air pockets. The channel thickness (0.8 mm, same as inner diameter) can also be distinguished around the boundary between water and air pocket. **b)** The image of the water slug extracted from a 100k fps in order to observe the cavitation activity inside the channel during sonication at 13 kHz, and the function generator is driven at amplitude of 270 mV. No cavitation is detected.

inside of a water slug through a channel sonicated at 13 kHz, and the function generator amplitude of 270 mV. The image is obtained from a 100k fps recording. No cavitation is observed inside the channel. Similar to Fig. 4.1.a., due to the same optical restrictions, it is very difficult to spot the upper and lower border of the inner tube wall. Channels are sonicated at 25, 36, 48 and 52 kHz, and are given in Fig. 4.2. Cavitation bubbles are seen as white, whereas their shadow is black due to reflection from the metal surface. In general, it is not possible to identify the cavitation conditions inside the channels in detail. The number and the size of bubbles are not clearly seen since bubbles are bright and they have shadows as well. The cavitation activity inside the channels is detected as the transducer is driven at 25 kHz or more. Change in the frequency of the transducer changes the share of travelling and standing waves through the channels. Thus, different amplitudes are applied for different frequencies in order to initiate cavitation. Moreover, more spherical, individual and smaller bubbles are obtained in lower frequencies. The increase in frequency leads to formation of bigger bubble clusters which can also exhibit a streamer structure. For the highest driven frequencies, bubble clusters become larger and have surface instabilities. Therefore, clusters of larger bubbles are observed and a higher number of bubble densities were obtained at higher frequencies. Moreover, the water-air interface is recorded and given in Fig. 4.3. Higher number of water droplets were observed at an air slug in higher frequencies. Injection of the water droplets can be correlated with the bubble densities and/or the bubble centers in water. Bubble seeding occurs only via surface waves/instabilities of the air-water interface of slugs. This works possibly better at higher frequencies. The reactor poses challenges for cavitation analysis and operation. Investigating cavitation conditions in channels is a challenging task due to their small scale and high speed. The use of rounded channels with an aluminum plate underneath presents an additional challenge related to brightness and contrast in imaging. The cavitation structures in the channels cannot be observed clearly, leading to

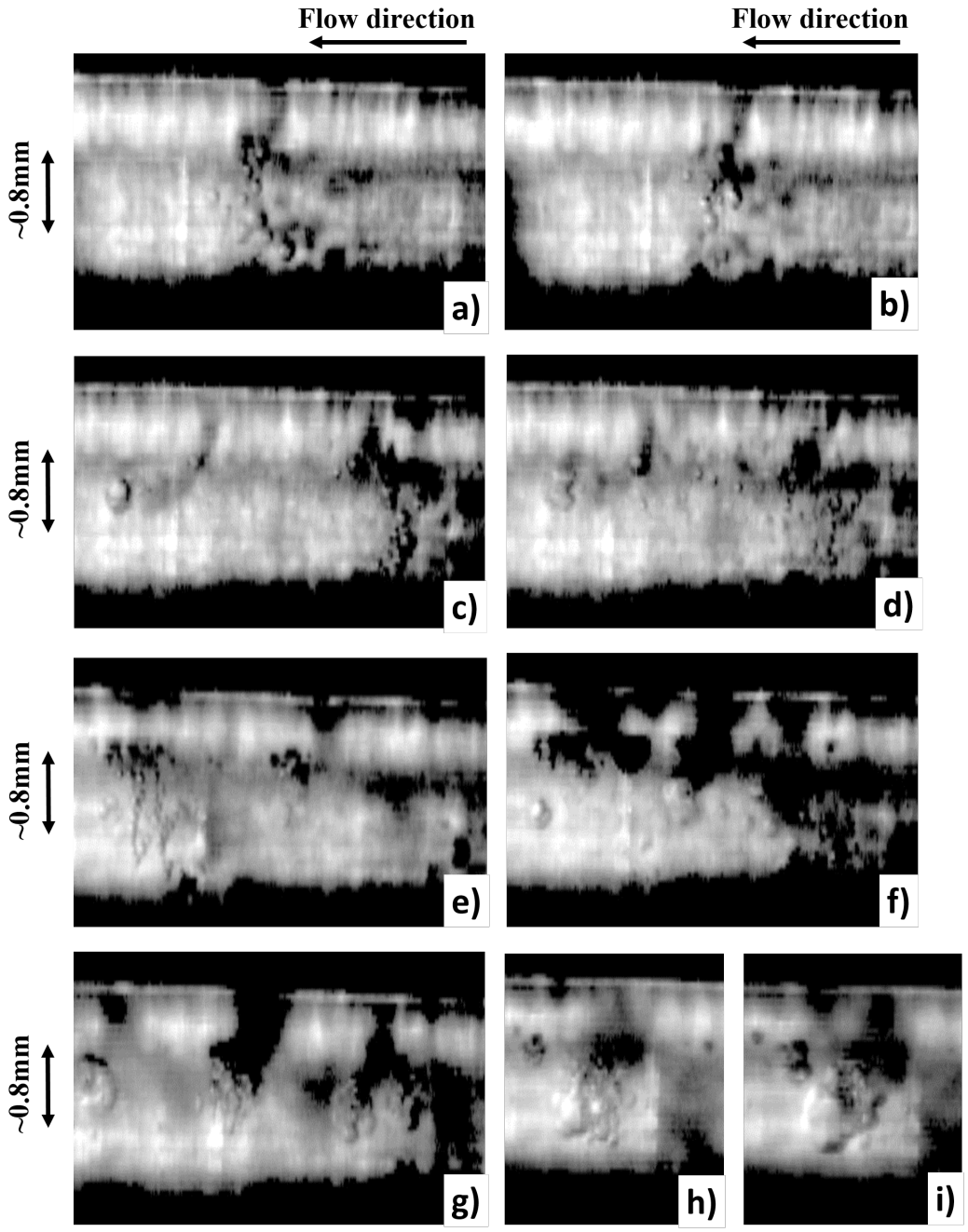

Figure 4.2. Images of cavitation activity inside channels sonicated at different frequencies. Images obtained with a high-speed camera at 100k fps. Rate of water-air slug flow is $\sim 7\,\mu$L/s towards to the left. The transducer is driven at **a,b)** 25 kHz, with 270 mV; **c,d)** 36 kHz, with 360 mV; **e,f)** 48 kHz, with 580 mV; **g, h,i)** 52 kHz, with 580 mV

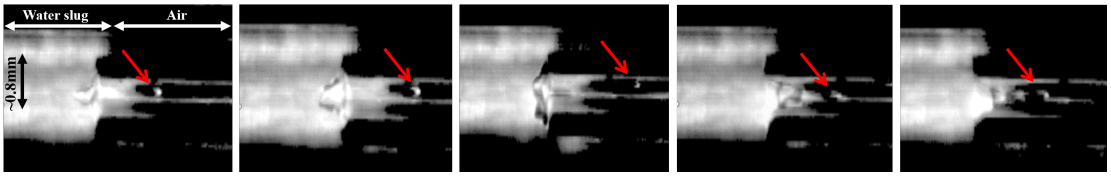

Figure 4.3. Interface between water (left) and air (right) slugs, obtained at a frequency of 52 kHz with the electrical input of 580 mV. The capillary waves and droplet/bubble ejection at the two-phase boundary seem to play a crucial role for the cavitation bubble seeding in the liquid. A higher number of ejected water droplets into the gas (arrows) were observed at higher frequencies, in correlation to higher cavitation bubble numbers at the higher frequencies.

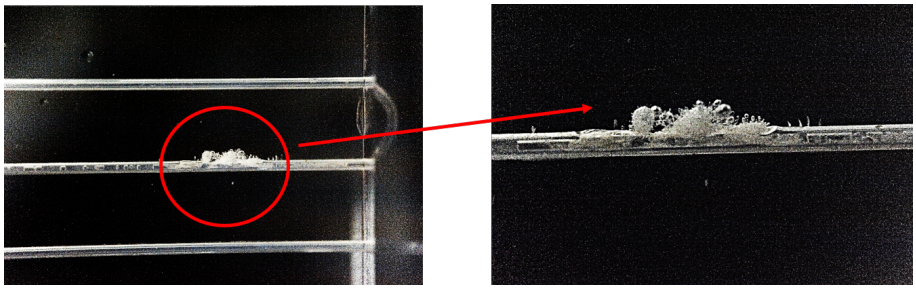

Figure 4.4. Deformation in PFA tubing and polycarbonate top cover caused by overheating of aluminum plate.

difficulties in extracting individual bubbles and measuring the time-dependent changes in their radius to investigate compression and rarefaction phases. Furthermore, the PFA tubing is not tightly squeezed between the aluminum plate and polycarbonate channels, resulting in gaps that affect the uniformity of sonication. The heating of the transducer and aluminum plate during sonication, along with the absence of a cooling unit or liquid, causes damage to the tubing and polycarbonate (see Fig. 4.4).

Due to the limitations in high-speed imaging, the direct coupling reactor is replaced with a *mini-ultrasonic-bath*. This reactor is designed and constructed by J. J. Joseph and the assembly of the reactor is depicted in Fig. 4.5 [166, 167]. The mini-ultrasonic-bath reactor simply introduces a coupling liquid that prevents heating problems and enables the control of the temperature as well.

Although the reaction chamber is directly mounted on the top of the transducer, it is considered an indirect contact type of the reactor due to the presence of coupling liquid. Moreover, the same authors implemented direct contact elements into mini-ultrasonic-bath as intervals which are simply holders to attach the channels to the metal plate underneath [167, 166]. This hybrid closed-interval mini-ultrasonic bath has been characterized and investigated in detail for liquid-liquid extraction. For collaboration purposes, the first variation of the mini-bath-reactor shown in Fig. 4.5 is tested. A mini aluminum cuvette is constructed by a 10 mm thick, 80 x 80 mm aluminum plate, hollowed out in the center to a depth of 8.5 mm. The PFA tubing is held by eight holes which are on two sides of the mini bath. The other two sides have holes for an inlet and an outlet for the circulation of the coupling liquid to the control temperature. The open-top bath is screwed onto a multi-frequency type Langevin transducer (Ultrasonics World MPI-7850D). A 5 mm plexiglass plate is screwed on top of the aluminum cuvette

and sealed to make sure the small compartment is watertight.

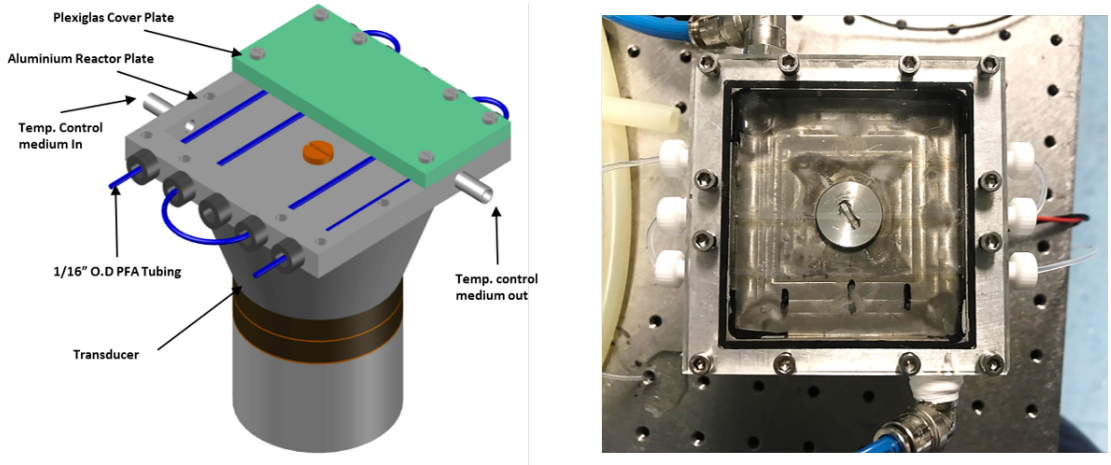

Figure 4.5. Mini-ultrasonic-bath reactor assembly and a top-view of reactor [166]

The mini-bath is filled with degassed distilled water via the coupling liquid inlet, then the inlet and the outlet are sealed. The coupling liquid is not circulated in order to prevent or at least suppress cavitation in the medium. The water-air slug flow is applied at flow rate of about 9 μ L/s into the channel whose diameter is 0.8 mm. Similar to the direct contact reactor, the channels are illuminated from top and the reflected light is collected via a long-distance microscope which is attached to a high-speed camera. The transducer is operated at 40 kHz and an amplitude of 590 mV applied (delivered power of about 19 W). Consecutive frames recorded at 100k fps from the water-air boundary are given in Fig. 4.6. It is seen that the air pocket containing bright water droplets is on the left, the water slug is on the right side with a wall-attached bubble cluster. As it is compared to the frames obtained from a direct contact reactor (see Fig. 4.2), the contrast of the two phases are different. The reason is the coupling media which absorbs the reflected light from the aluminium plate underneath. The water-air interface shows surface oscillations and water droplets are being ejected into the air gap. Water droplets can be shot hard due to stronger surface oscillations. This, in turn, could result in ejected water droplets having longer trajectories and facilitates the merging of water droplets which is the reason of a distorted surface reflection recorded from a big water droplet in some frames. On the other hand, wall-attached bubble clusters cannot be identified enough. It is concluded that the mini-bath enables observing the events taking place in an air gap, whereas it offers poor contrast to identify and analyse bubble structures in detail.

4.2 Channels in bath reactor

4.2.1 Sonicated submerged flow tubes

In this section, experiments were carried out with a 0.1 mM luminol solution prepared as mentioned in Sec. 3.2.1. After the formation of the air and luminol slugs by alternating pumps, the flow was stopped when the slugs became about 1cm in length. The experimental results demonstrated in this section were obtained from non-moving slugs.

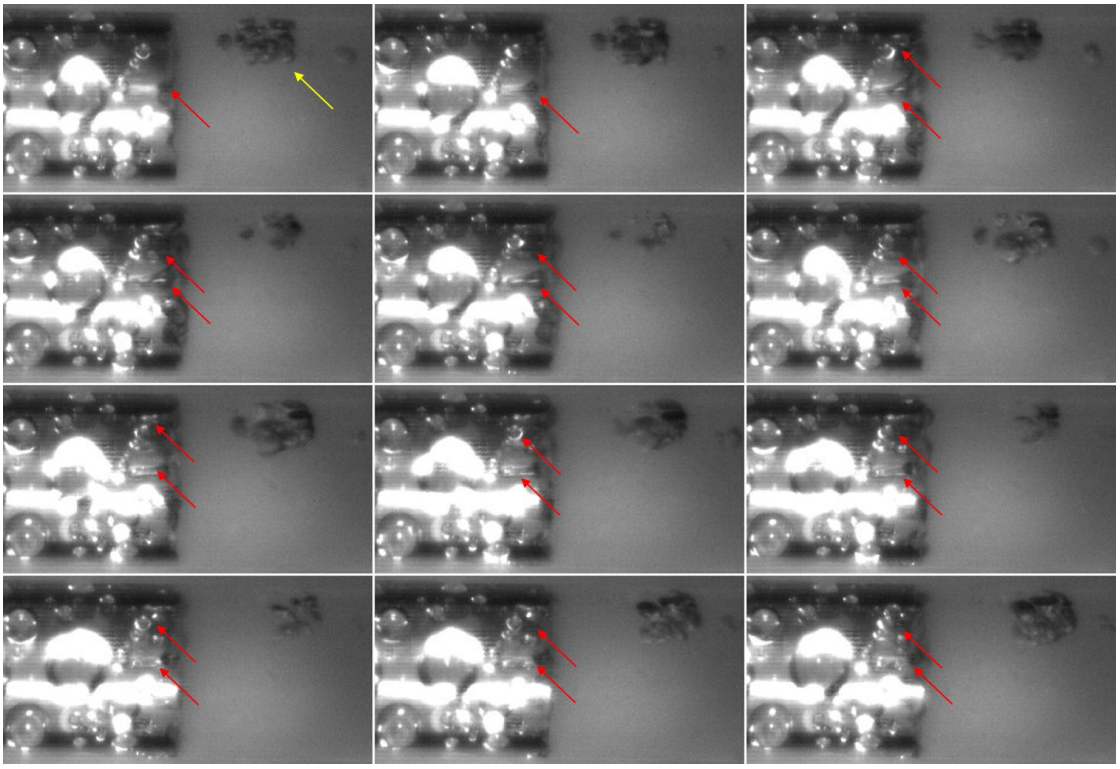

Figure 4.6. Oscillating bubble cluster in water slug and ejected water droplets in air gap. The yellow arrow show the bubble luster in the channel, while the red arrows point the droplet ejection. Consecutive frames are obtained by recording with 100k fps and an exposure time of 10 μs. The frame height is approximately the same with the channel diameter which is 0.8 mm. The transducer is operated at 40 kHz with a delivered power of 19 W (the difference between the forward and reflected power). The water-air slug flow rate is about 9 μL/s and flow direction is from left to right.

In these experiments, the applied ultrasound frequency and electrical power are 27.2 kHz and 65 W, respectively.

4.2.1.1 Sound field inside an ultrasonic bath

To investigate the cavitation conditions inside the tube, the sound field inside the ultrasonic bath was experimentally analyzed and numerically simulated. The acoustic pressure distribution inside the ultrasonic bath was experimentally mapped by using a probe hydrophone. A hydrophone scan was carried out in a rectangular region where the tube was located, in the absence of a tube. Driving frequency was 27.2 kHz at a power of 65 W. The measured sound field, appearing as a rectangular region, is overlaid to the graph of the cuvette according to the exact measurement position in Fig. 4.7.a. The noise of the measurement is rather high, since the sound field forms standing waves and leads to cavitation in the liquid at the indicated power. Moreover, the data intervals are rather coarse due to the size of the hydrophone. The color code represents the amplitude of the fundamental frequency which is derived after the Fourier transform of the hydrophone time traces obtained at the scan positions. Since the diameter of the probe is about 10 mm, it does not come closer than 5 mm to the bottom and the wall

of the cuvette. It is measured that the sound pressure is about 2.5 bar (250 kPa) at the bottom of the bath close to the transducer surface. Vertically, after that high-pressure zone, the first low-pressure region lies in about 25 mm height, and then another high-pressure region appears in about 40 mm height, having amplitudes in the range of 2 bars. The pressure amplitude does not go completely to zero in between those two maxima regions, showing that there is a certain share of traveling waves within the field. Further it is seen from the mapped region that the pressure decreases and falls off to zero towards the top of the open surface and towards the walls of the cuvette. The water-air interface should well behave like a sound soft boundary (pressure node), which is clearly the case. While the cuvette wall material polycarbonate has a slightly higher impedance than water (2.7 MPa·s/m vs. 1.5 MPa·s/m), the outer boundary of the rather thin plastic wall (5 mm) should again be sound soft. From the measurements one can see that the container walls act essentially sound soft, and a pressure node forms.

Fig. 4.7.b represents the numerical simulation of the pressure field inside the cuvette. The numeric model is constructed on Louisnard's approach [168]. This model is based on a modified Helmholtz equation taking nonlinear dissipation into account, caused by homogeneously distributed bubbles. The model is solved in 3D by using the finite element software of Comsol (Comsol AB, Sweden) (further reading, [169]). A comparison to the measurement shows a good correlation of the numerical pressure result.

Figure 4.7.c depicts the SCL emission from the ultrasonic bath filled with luminol, captured at the same frequency of 27.2 kHz and power of 65 W, and with the exposure time of 30 sec. As a result of sonochemical activity ($HO^{\bullet}$ radical production) inside the ultrasonic bath, blue light is emitted. Observing the spatial distribution of light intensity thus allows to characterize chemical cavitation activity inside the liquid [170]. As a "first approximation", one would expect a high cavitation activity at high sound pressure levels, and therefore a high correlation between luminol emission regions and high sound pressure regions.

According to the sound field simulation (see Figure 4.7.a), the first and highest maximum pressure region is seen as a red hump lying up to a height of around 20 mm directly on top of the transducer. However, contrary to the "first expectation", only very little luminescence emission is observed at the bottom of the cuvette above the transducer. Mainly a central faint blue vertical stripe appears, but to the left and right remains a rather dark region. Above the stripe, a first horizontal blue band occurs, somewhere between the high pressure region in front of the transducer and the pressure minimum ("node"). A similar, but stronger emitting horizontal band exists further up, again in-between a node and high pressure zone (antinode). Then a dark hole and again a blue region somehow below the free surface follow. The dark hole is rather well positioned where hydrophone mapping and numerical simulations show a pressure antinode.

The absence of SCL emissions in the high pressure zones and antinodes is at first glance surprising, but can be explained by Bjerknes forces and bubble dynamics at high driving pressures. As we have seen in Sec. 2.1.6, the primary Bjerknes force in a standing wave, acting on a bubble of given equilibrium radius, inverts at some high pressure level. This means that bubbles are repelled from antinodes if the sound pressure is sufficiently high, and no bubbles will remain in these zones. Instead, the bubbles group "half-way" between pressure nodes and antinodes, forming specific patterns ("jellyfish" structures,

see [171]). Here it seems to happen exactly like this, and the horizontal pair of blue bands above the transducer probably corresponds to a time averaged picture of chemical activity of a jellyfish structure. Further, the absence of bright SCL in the region right above the transducer is possibly due to a fast bubble repulsion from the transducer surface, leading to fast upwards streaming bubbles (which are typically continuously nucleated at the transducer). When the bubbles are moving too fast, non-spherical shapes and jetting will occur [172], potentially destroying or deteriorating the hot spots and thus the chemistry during bubble collapse. The faint vertical stripe might indicate the still active bubbles in the upward bubble stream ("lightning" structure, see [171]).

Further arguments to explain the observed disagreement of the high sound pressure and SCL or SL refer to the formation of bubble clusters in strong cavitation [173]. Other authors have reported that the acoustic pressure amplitude increases the luminescence intensity up to a certain threshold, beyond that luminescence intensity is diminished [174]. The cluster argument involves the secondary Bjerknes forces, causing the bubbles oscillating in phase to be attracted to each other, forming a cluster. Once the pressure amplitude increases, the secondary Bjerknes force becomes stronger, and more or larger bubble clusters are formed. Within the cluster, bubbles tend to coalesce and become larger, which would result in repulsion from the antinode and pushing towards the nodes in the standing wave [175]. This argument is reminiscent to the expulsion of bubbles of fixed size at growing pressure amplitude: Note that in Fig. 2.10 one can change from antinode attraction to antinode repulsion via increasing driving pressure, or via increasing the bubble equilibrium size. Potentially, both can happen at the same time, of course, leading high pressure zones empty of bubbles and without SCL signal.

Still another argument refers to sound damping inside a dense bubble cluster. The intensity of a sound wave passing through bubble clouds or clusters decreases due to the impedance shielding effect caused by the outer surface of the bubble cluster. This, in turn, should lead to a decrease of the luminescence intensity. It is further noted that with an increase in sound pressure, the rate of increase in the secondary Bjerknes force is much larger compared to the primary Bjerknes force. Eventually, it becomes dominant as the sound pressure amplitude exceeds a certain threshold and might diminish the luminescence intensity [174]. The same mechanism could also explain the bright region on the bottom left and right of the bath. Bubbles expelled from the high-pressure zone might travel to the lower-pressure regions. Moreover, it can be observed that the bottom left surface of the bath emits bright luminescence, whereas no corresponding high-pressure region is observed in the simulated map. This may be due to a second transducer attached to the bottom left. The second transducer was neglected in the simulations since it was turned off, but the boundary conditions might be affected. In particular, this region might result in a non-soft impedance or even a sound hard wall where higher pressure develops and bubbles collapse more strongly, finally producing the $HO^{\bullet}$ radicals observed via their luminol emission.

In conclusion, the experimental pressure map and the numerical simulations agree quite well, considering the noisy (cavitating) environment and the approximations made in the numerical model (e.g. homogeneous bubble void fraction, monodisperse bubble population, that are probably not fully met in reality). Therefore, it can be supposed that the pressure distribution is roughly like shown in Fig. 4.7.a, b, and indeed the highest pressure zones remain void of SCL, as shown in Fig. 4.7.c. This in turn implies

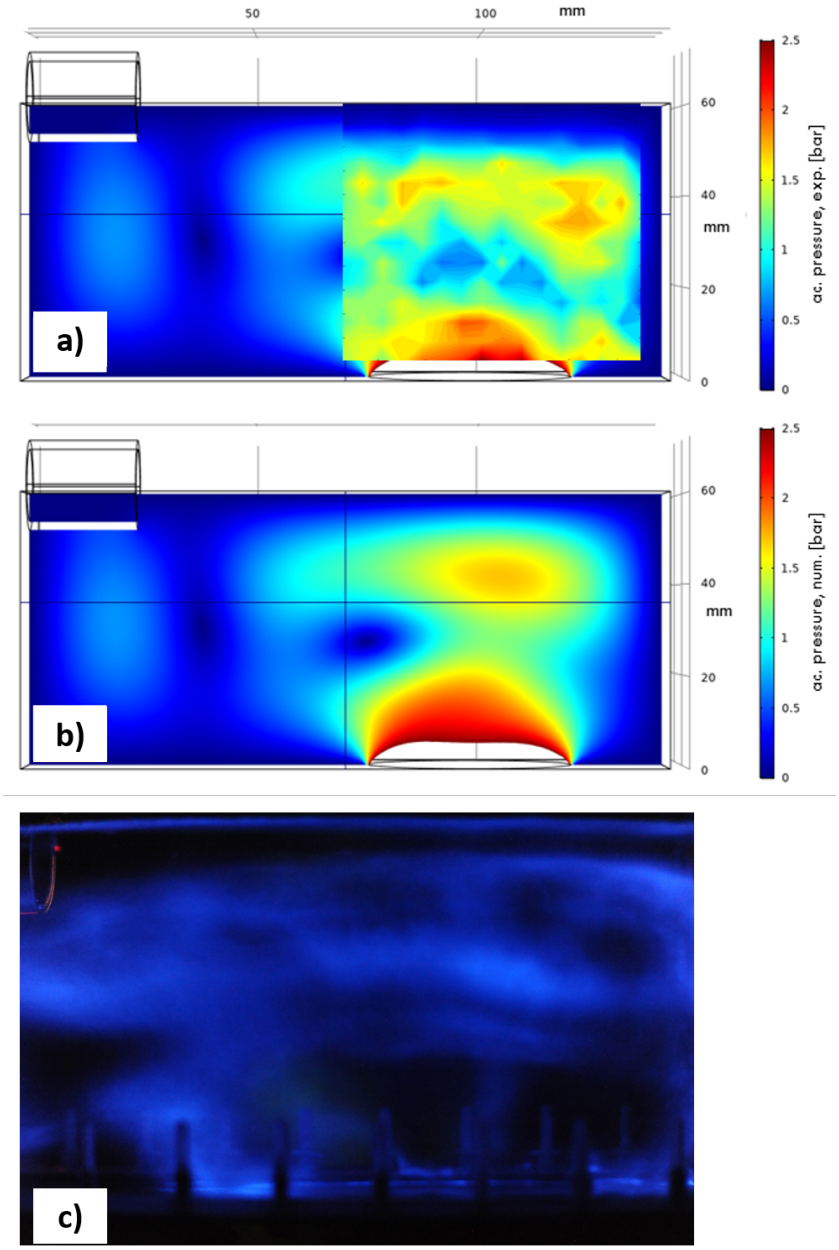

Figure 4.7. **a)** Measured pressure amplitude in the central plane above the transducer which is at the bottom right. The hydrophone-scanned rectangular area is positioned on the background of the numerical mapped sound field. **b)** Colour codded sound pressure amplitude on the central, vertical plane above the transducer (calculated with Comsol applying Louisnard's model [168] with a gas void fraction of $\beta = 4.10^{-7}$ and a radiated power of 65 W). The colour code for the corresponding pressure values of both images are identical. For a better contrast, the value of the pressure is limited by 2.5 bar, and the higher pressure areas (right above the transducer) appear in white colour. **c)** SCL emission of sonicated aqueous 0.1 mM luminol solution (filling height of the bath 6 cm; exposure time 30 seconds; 27.2 kHz, 65 W.)

either repulsion of active bubbles from the high pressure regions (probably taking place around the "dark holes" in the upper part of Fig. 4.7.c, where bright ring-like structures occur), and/or too fast bubble propulsion, leading to non-spherical collapse geometries and thus "too cold" collapse spots for chemistry (possibly happening directly above the transducer in the right lower part of the figure). Further, a too dense clustering and according pressure shielding might happen to avoid SCL at high pressure zones. Taking these effect into account, many features of the luminol emission map can be explained in relation to the pressure maps, in particular a favorable emission condition somewhere between highest and lowest acoustic pressures.

4.2.1.2 Sonochemiluminescence from channels

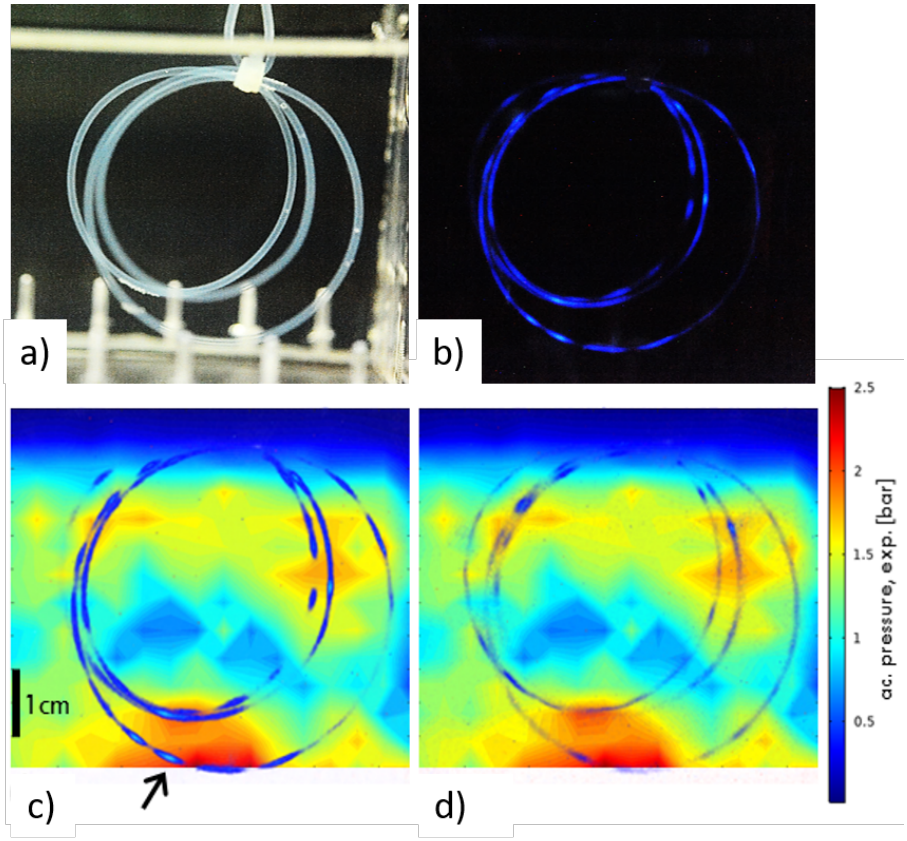

Figure 4.8. **a)** Daylight image of the loops in the ultrasonic bath filled with water. The white horizontal line over the loops is the water level in the bath, the spikes at the bottom of the cuvette are the screws joining the polycarbonate walls and aluminum bottom plate of the bath. **b)** SCL emission from luminol-air slugs along tube (27.2 kHz, 65 W, water height 6 cm, exposure time 30 s). **c, d)** Two different emission recordings of luminescence from the loops, overlaid to the measured sound field (units see colour coding bar). The arrow shows the approximate position of the channels in which high speed recordings of Fig. 4.9 have been obtained from.

It has been previously reported that neither cavitation bubbles nor luminescence emission are observed in sonicated, relatively small (20 μm) channels filled only with liquid [11]. Similarly, no cavitation bubbles are detected in larger sonicated tubes filled with pure

liquid. Cavitation conditions have been found to only take place within the existence of both liquid phase and gas phase in the channels. Therefore, aqueous luminol solution and air are both pumped into the loop-shaped channels via a T-junction, forming a Taylor flow. The flow is stopped to collect luminescence emission with higher contrast, since the SCL signal from small volumes is very weak and difficult to detect, and the temporal shift of the liquid slugs would deteriorate the situation. As stationary slugs are sonicated, regions of cavitating aqueous luminol solution emit weak blue light, which again indicate $HO^{\bullet}$ radical formation [77].

Fig. 4.8 presents an image of the loop arrangement in the bath and SCL emissions from two different runs of sonication, together with a mapped sound field. In Fig. 4.8.c and d, blue emissions are extracted from raw images and embedded in the measured sound field (see Fig. 4.7). It can be observed that the recorded signal follows the shape of the loops; however, the emission is not continuous along the tube. This might be due to no nucleation in the air gaps between luminol slugs, inadequate driving pressure to promote cavitation conditions or chemical activity, or low luminescence emission below the detection threshold. Since the luminol slugs and air gaps are no longer stationary during sonication, they can undergo different events such as splitting, merging, and some slugs becoming shorter or longer than 1 cm. This also alters the number of cavitation bubbles and the intensity of luminescence emission in each volume of slugs. Additionally, luminescence emission is brighter at some spots along the tube due to the different structures of localized bubbles discussed in Section 4.2.1.3. The sound field pressure distribution is also a determining factor in the strength of the signal. Although the SCL signal is relatively high in the high-pressure region, there is no complete correlation. From the low-pressure region of the lower right side, weak emission or no signal is detected, as expected. On the other hand, clear luminescence emission is observed from the left side of the low-pressure region. The inconsistency between sound pressure regions and corresponding luminescence emission obtained from loops might be possibly due to gas pockets between luminol slugs. The existence of air gaps along the tube leads to perturbation of the sound field, *i.e.*, reflections. Furthermore, it is also observed that the length of the luminol slug and the ratio between the lengths of luminol slugs and air gaps also change the cavitation conditions inside the tube. Acoustic resonance in luminol slugs may also be another factor explaining the discrepancy in luminescence emitting areas of the loop and the sound field map inside the container [176].

4.2.1.3 Bubble structures

Cavitation activity was examined from the left bottom of the part of the channels shown by an arrow in Figure 4.8.b. The flow was stopped during sonication, and bubble structures were observed. Bubbles show erratic behavior and form prototypes of clusters in different varieties. Figure 4.9 represents a series of bubble ensembles recorded in a total amount of time of approximately one second. One of the distinct characteristics of bubble clusters is the tendency of attaching or aggregate to the upper or bottom walls of the tube (Fig. 4.9 a,b.). Another typical structure is "plug" which is a rectangular ensemble of bubbles stretching between the top and bottom surface of the tube (Fig. 4.9 c,d), and also sometimes having sharp edges at the sides as well (Fig. 4.9 e,f). Although both structures are confined longitudinally, it is not very clear whether the

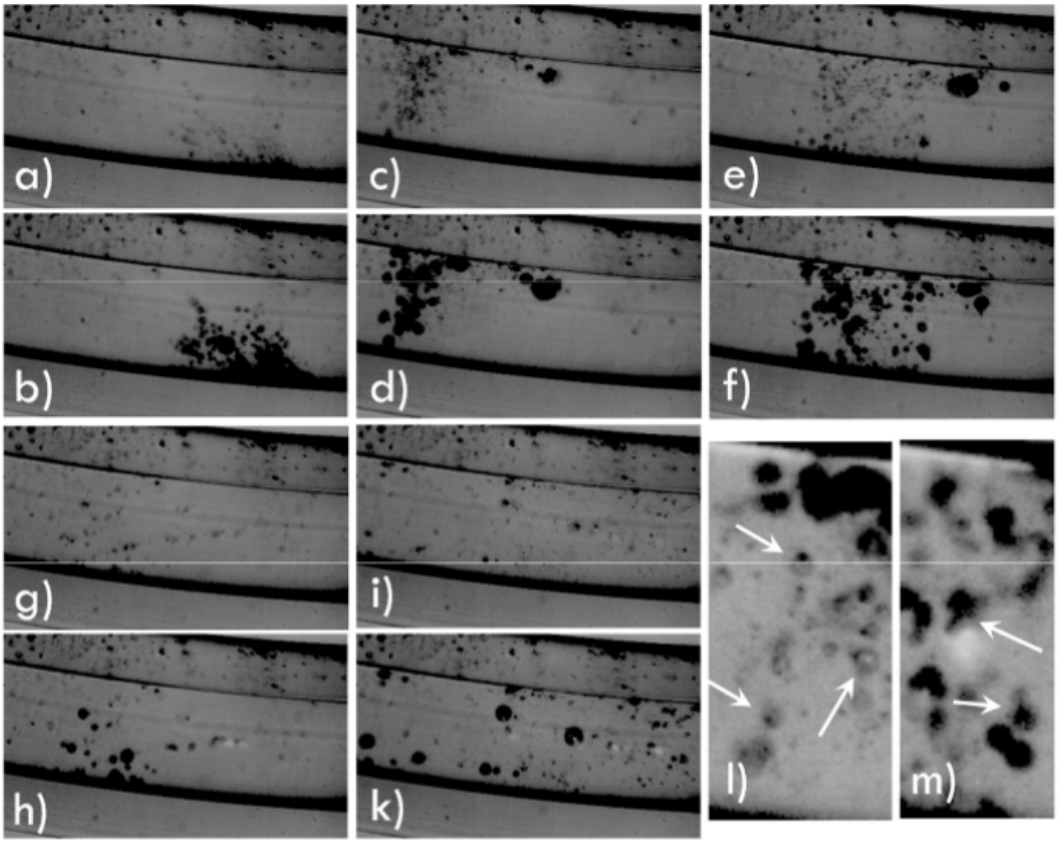

Figure 4.9. Different cavitation bubble structures in the tube, at the nearly collapse phase and subsequent phase of maximum expansion. Recorded with 20k fps, exposure time of 50μ s. Frame height is approximately 1.5 mm from a to k, and 0.8 mm for l and m. **a, b)** Wall-attached cluster, **c, d)** Narrow plug, **e, f)** Wider plug, **g, h)** Streamer, **i, k)** Disperse, **l, m)** Displacement and jetting of bubbles.

bubbles agglomerating towards the walls and the ones in the shape of plugs are similar or not. Since the tube is spherical, it is not possible to discuss the attachment of bubble clusters to the back and front walls of the tube. However, as they are compared in longitudinal along the tube, it can be said that the plugs seem to have sharp limits to the neighboring bubble-free regions at the sides, whereas the wall-attached ones do not have such clear boundaries to the remote bubbles in their surrounding liquid. There are also less confined structures such as longitudinal streamers and fully dispersed bubble fields, given in Figure 4.9 (g,h) and Figure 4.9 (i,k), respectively.

Confined cavitation bubbles interact strongly and frequently, due to low inter-bubble distances. Different events, such as merging and splitting, take place every few or each acoustic cycle. While interacting, they move and a collapse jump occurs accompanied by a jetting event. Displacement and jetting events are shown in Figure 4.9 (l,m), and arrows mark the bubble silhouettes/shades recorded during the long exposure time. An individual bubble cannot be tracked due to some rapid interactions and displacements. Moreover, low spatial resolution (~5μm/pixel) leads the collapsing bubbles to disappear and limits the re-identification of individual bubbles after the collapse. Cavitation bub-

bles interact less frequently in more diffuse structures, but a collision still occurs every few acoustic cycles. In one structure, approximately 30 to 200 bubbles can be identified, but the number of bubbles varies during the acoustic cycle. Only a few collapsing bubbles can be observed since the spatial resolution is low. The maximum number of bubbles in one structure is recorded somewhere between minimum and maximum expansion. As the maximum expansion is reached, a total number of bubbles again decreases. In consecutive frames of Figure 4.9, various clusters, sizes, and numbers of bubbles are demonstrated at the phase of near collapse (1^{st} frame) and full expansion (2^{nd} frame).

4.2.1.4 Bubble dynamics reconstruction

When the experimental data can be resolved enough to observe the oscillation of a bubble at least for a few cycles, one can simulate bubble radius-time dynamics and bubble collapse conditions. Numeric models allow reproducing of the experimental data by using the bubble radius at equilibrium and the local pressure amplitude. Although bubble systems are typically unsteady, the models are still useful to produce reliable estimations. Here, in order to improve the temporal resolution of the image recordings, a few bubble oscillation periods are observed and back-folded to a single acoustic period [177].

The dynamics of the bubble oscillations are fitted to the model of Zudin given in Equations 2.20 and 2.19 [57], which has an additional term for the presence of tube walls derived from a single bubble model postulated by Keller-Miksis [49]. That model simulates the temporal evolution of the bubble with an equilibrium radius of R_0 inside a cylindrical tube of length L and radius R_T, under an acoustic pressure of $p_{ac} = p_a sin(2\pi ft)$, where f is the acoustic frequency (27 200 Hz). Other parameters can be listed as; static pressure (p_0=100 kPa), vapor pressure (p_ν=2.33 kPa), surface tension (σ =0.0725 N/m), dynamic viscosity (μ=0.001 Ns/m^3), the density of the liquid (ρ=998 kg/m^3), the polytropic exponent is set to the adiabatic gas compression (γ=1.4, for air), and water properties are valid for the temperature of 20°C. It has to be noted here that a smaller channel radius and/or a longer tube length influence the parameters. One particularly expects a reduction in both the linear resonance frequency and the amplitudes of driven oscillations [58]. On the other hand, a larger tube radius and shorter tube length lead to typical bubble dynamics in an infinite liquid. By using this model, maximum and minimum radii can be calculated, and the compression ratios R_0/R_{min} can be estimated to identify the peak conditions during bubble collapse.

The model used for the reconstruction of the bubble radius vs time curves is based on a single stable oscillating bubble at least for a few cycles. However, such isolated individual bubbles are not prevalent in multi-bubble structures and the number of bubbles to be tested is limited. A sample bubble used for the reconstruction and the radius-time plot is given in Figure 4.10. The representative bubble was located at the tail of a "plug structure" which is recorded at 100k fps, and the plot is obtained by back folding of the measured data points onto a single driving oscillation, assuming it is periodic. Data points do not precisely fall onto a single curve, hence they do not represent a perfect periodicity. Nevertheless, the consistency of the expansion phase for 0.4< t/T <0.6, and the collapse phase at around t/T $\approx$ 0.9. The equilibrium radius of the bubble approximately equals the size measured before expansion, which is around $R_0 < 3.5\,\mu m$,

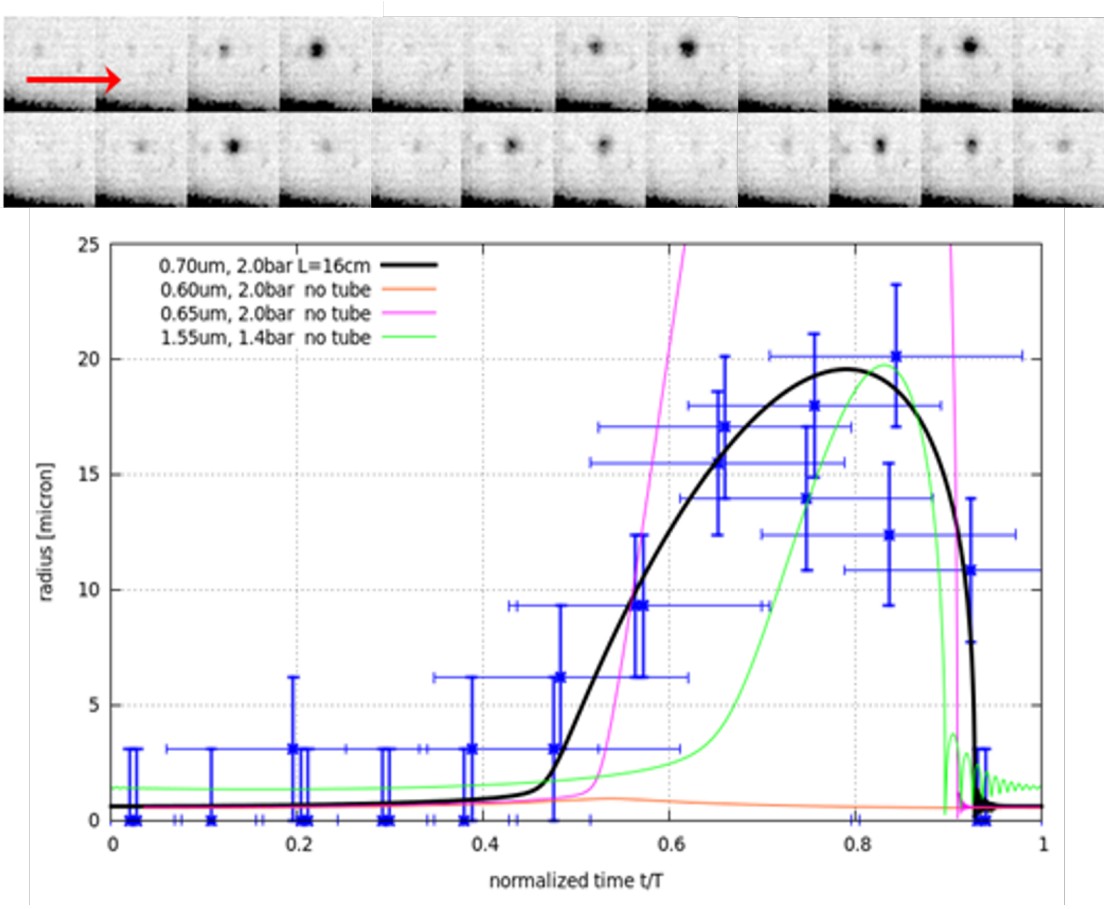

Figure 4.10. A single bubble at the edge of a "plug structured" cluster in a flow tube exhibits nearly stationary dynamics. **Top:** A sequence of 24 frames of a bubble corresponding to 6 driving periods from left to right in the direction of the arrow. Recording is at 100k fps, exposure time is 10 μs, and the frame width is 192 μm. **Bottom:** Reconstructed bubble radius-time curves. The experimental bubble radius is given with error bars and back-folded onto a single acoustic period $T = 1/f$. Different colors of lines represent different cases of the bubble dynamics model as mentioned in the text. The best fit is given as a thick black line, obtained for the pressure amplitude of p_a=2 bar, with $R_0 = 0.7\,\mu$m and L=16 cm.

whereas the maximum radius is $R_{max} \approx 20\mu m$. That gives the ratio of R_{max}/R_0 larger than 6, which indicates a strong collapse. Using the aforementioned model of Zudin (Eqs. 2.20 and 2.19) with a sound pressure amplitude of 200 kPa supposed by sound field measurement, a good fit is obtained for the tube radius of 0.4 mm in the length of 16 cm, and is represented in Figure 4.10 as a thick black line. According to that model, the bubble collapses down to R_{min}=0.085 μm which gives the maximum gas compression ratio of $\alpha = R_0/R_{min} \approx 8$. By using the adiabatic law of $T_{max} = T_0\alpha^{3(\gamma-1)}$ where the ambient temperature is $T_{max} = 293$ K, the peak temperature is derived as $T_{max} \approx 3500$ K. It has to be noted that without taking the presence of the tube into account, obtaining a reliable fit becomes difficult. As the standard Keller-Miksis model is applied (L=0) to reproduce the experimental data for P_a=200 kPa, a response converges to the sensitive parameters close to the Blake threshold, in which a slight change in R_0 causes either very small or very large R_{max} values [39]. Such cases of modeled bubble

oscillations are shown in Figure 4.10, for an equilibrium radius pf $R_0 \approx 0.6\,\mu$m (pink line, having a peak lying out of the plot) and $0.65\,\mu$m (orange line). Moreover, if a lower pressure is applied to attain the R_{max} value, which is compatible with the experimental data of R_{max}, one obtains a much shorter expansion. This case is also demonstrated in Figure 4.10 as a green line which is the plot for R_0= $1.55\,\mu$m and p_a= 140 kPa. It is seen that the R_{max} value meets the experimental value well, however, it does not represent an extended expansion.

For a successful bubble dynamics fit, another point to be considered are the parameters regarding the tube. The tube radius is experimentally fixed, whereas the tube length L has to be chosen larger than the average length of the liquid slugs (∼1cm). Otherwise, R_{max} goes again to large values. This could be possibly due to the effects of neighboring bubble clusters, which might be similar to the tube walls. This could be due to the effects of neighboring bubble clusters, which might have a similar influence on the presence of the tube walls.

4.2.2 Sonicated stacked flow tubes

In this section, the same in-house-built ultrasonic bath is used as a reactor. PFA tubing (inner diameter of 0.8 mm) is fixed in parallel, equidistant horizontal sections and submerged into the water-filled bath with the help of a polycarbonate holder. The experimental details are provided in Section 3.1.2.2. The bath is now filled with 11 cm of water, which changes the resonance frequency slightly to 25.7 kHz, as well as the standing wave pattern. Ultrasound is applied with different amplitudes.

4.2.2.1 Sound field inside an ultrasonic bath

The applied ultrasonic field forms a standing wave and generates cavitation inside the bath. The presence of a cavitating bubble field in the coupling liquid leads to a higher dissipation rate, resulting in the propagation of traveling waves [168]. To better characterize the cavitation conditions for flow tubes, the acoustic pressure inside the ultrasonic bath is again analyzed both numerically and experimentally.

Fig. 4.11.a depicts the measured acoustic pressure distribution inside the bath by a hydrophone, in the absence of the tube. The rectangular pattern is the measured pressure map which is placed onto the numerical simulation according to the measurement coordinates. The hydrophone probe avoids touching the side walls and bottom plate of the bath, hence the measured pressure map starts at a distance of 0.5 cm from each corner. Since the ultrasonic bath was originally built for some different experimental purposes [60], it has a flow inlet towards the inside at a height of about 6 cm which also limits the measurement of sound pressure on that side of the bath. The bath is scanned while the transducer is driven at 25.7 kHz with 10 mV. The resolution of the map is increased by setting the data collection steps of the probe to a distance of 0.2 cm, and a 90 mm x 90 mm area is scanned. After completing the pressure map, the transducer is driven with 340 mV which corresponds approximately to an electrical power of 60 W. The sound pressure of three points around maximum pressure is measured. The average of high voltage and low voltage measurements for each point are taken as a factor to scale up the sound pressure map obtained at amplitudes of from 10 mV to 340 mV.

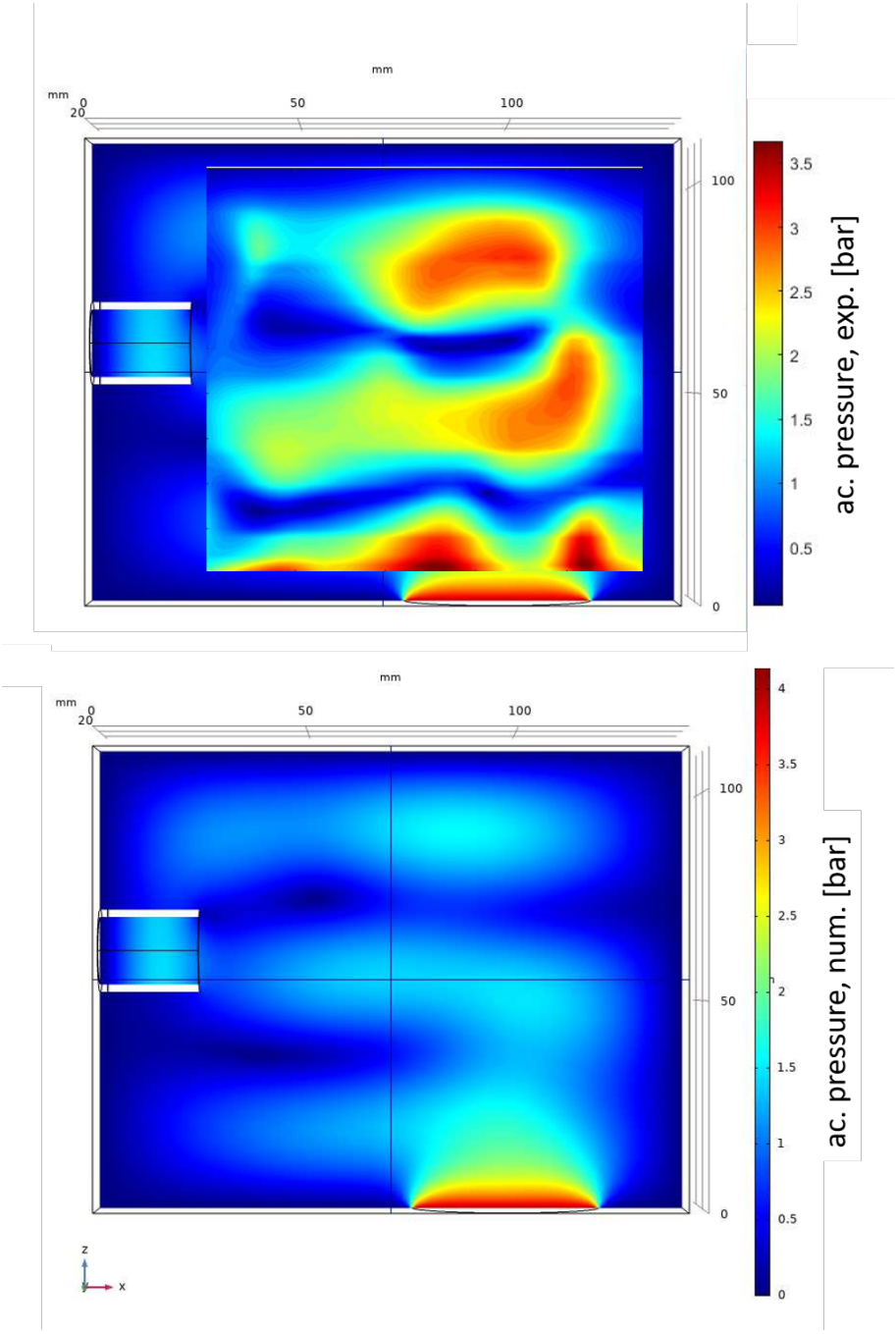

Figure 4.11. **a)** The measured sound field map with the color-coded pressure amplitude. The map is observed as a rectangular pattern on the background of the numerical simulation according to the exact measurement coordinates. The transducer is operated at 25.7 kHz. The applied voltage is maintained at an electrical power of 10 mV during mapping. **b)** Numerical simulation of the sound field inside the ultrasonic bath. The void fraction is $\beta = 5.10^{-6}$, with monodisperse nuclei of equilibrium size $R_0 = 5\,\mu$m.

The numerical simulation of the acoustic pressure inside the ultrasonic bath is given in Fig. 4.11.b. Similar to the 6 cm water-filled ultrasonic bath, here the same approach of Louisnard is used [168]. With this model, nonlinear dissipation caused by homogeneously distributed bubbles is taken into account. This approach proposes that bubbles generate passive nuclei up to a certain acoustic pressure amplitude, but beyond that, they turn into cavitation bubbles dissipating strongly. The parameters of water are standard, and the parameter for the bubble void fraction is $\beta = 5.10^{-6}$ with monodisperse nuclei of equilibrium size R_0=5 μm. The finite element software Comsol (Comsol AB, Stockholm, Sweden) is used again to solve the model in the 3D domain with sound soft boundary conditions for the walls of the container and the free top surface. This is a reasonable approach as argued above, since the impedance of polycarbonate is not too dissimilar to water $Z_{polycarbonate}/Z_{H_2O} \approx 1.8$), and the outside is surrounded by air. The flow tubes are not taken into account in the simulation. As it is seen from Fig. 4.11, the maps obtained from the hydrophone measurement and numerical simulation are compatible. The positioning of the maximum pressure zones is very similar. After the first maximum pressure zone, the next pressure maxima lies in between the water height of around 40 and 60 mm in both maps and the pressure between the two maximum zones falls to zero.

As expected, the highest acoustic pressure is measured at the bottom of the bath to which the transducer surface is attached. The highest pressure has a distribution over the cuvette bottom at three different zones, rather than being a single hump as it is seen from the simulated map. The middle one which is wider than the other two might be the one coming from the transducer directly. The small one on the left and the narrower one on the right side can be due to the boundaries of metal and polycarbonate. Further, as mentioned above, the second (silent) transducer, attached to the left below the bottom, is not considered. There might also be bending modes or some attenuation factors between the transducer and the metal plate of the bath. The bottom of the container is made of stainless steel (thickness of 1.5 mm), whereas the front element of the transducer glued to the bath is made of aluminum. Employing two different metal compositions might lead to attenuation of the ultrasound signal due to the difference in acoustic impedance. It is also known that transducers become warmer after a certain operation time and/or power, and they dissipate heat. The transducer here is attached to the cuvette via glue which eventually affects the traveling sound waves and causes some distortion of the transmittance. All these factors are not taken into account while simulating the pressure map.

4.2.2.2 Sonochemiluminescence from an ultrasonic bath

The SCL images of Ar-gassed luminol solution filled in the bath are recorded for different sound pressure amplitudes and given in Fig. 4.12. Luminescence emission from the container is recorded with 30 s of exposure time, for different function generator amplitudes from 500 mV to 100 mV (i to ix), with a decreasing step of 50 mV. The delivered electrical power (the difference between forward and reflected power) approximately is 93, 84, 75, 62, 48, 33, 24, 13, and 5 W, respectively from i) to ix). Since the exposure times are 30 s, each column is recorded in 4.5 minutes, and performed one after another consecutively from a) to c). Therefore, from the left top image to the right bottom image, the total sonication time is 13.5 minutes. From one column to another, there is

no significant change in the SCL profiles. Quenching of the SCL from luminol, ultrasonic degassing (especially Ar), change in gas content of the aqueous solution, energy dissipation by heating of the transducer and the liquid can cause less $HO^{\bullet}$ production, and lower cavitation activity for long operation times. Therefore, SCL signals decrease from left to right for each row. It should be noted that for power inputs lower than 5 W no luminescence emission is observed. It is seen that as higher delivered electrical power is applied (first three rows), strong luminescence emissions are recorded over the bottom surface of the container, particularly where the transducer is attached to. However, above the mid-height of the bath, there is no or weak luminescence emission observed. Between the third and fourth rows, the overall SCL profile changes drastically when the electrical power is set from ∼75 W to ∼62 W. For applied power lower than 62 W which is from the fourth to the eighth row, a similar SCL emission profile is observed, becoming thinned out for lower power. Finally, a somehow different and sparse pattern appears at the lowest driving amplitude in the last row of Fig. 4.12.

The most intense emission is recorded from the first three rows of Fig. 4.12. It is seen that there is strong emission over the transducer surface, whereas the upper half of the bath is emitting weak or no luminescence. As the power input increases, the sound field travels further in the liquid, and as a result, sonochemically active zones spread over larger regions and more $HO^{\bullet}$ radical formation is seen. This has been previously reported and confirmed with sono-generated chemiluminescence studies [77]. On the other hand, the number of cavitation bubbles increases and forms a bubble cloud that can absorb and/or scatter the sound wave. This can consequently cause bubble shielding which is weakening the acoustic field. It has been reported that an increase in power changes the volume of the bubble cloud more than proportional; hence, it cancels more sonochemically active regions by increased energy dissipation [178]. Moreover, these bubbles can also alter the acoustic impedance of the medium resulting in a decrease in energy transfer efficiency from the transducer to the medium. This attenuation factor is called decoupling losses. The overall intensity of emission diminishes within the change in electrical power from ∼93 W, row i), to ∼75 W, row ii), which attributes to a decrease in sonochemically active zones. There is almost no SCL emission up to a container height of about 40 mm which looks like a void of cavitation as a result of bubble repulsion from a high-pressure region. There are only some corners and walls away from the transducer surface where luminescence emission is detected. This means that bubbles repelled from the high acoustic pressure produce $HO^{\bullet}$ radicals.

The overall SCL profile changes drastically when the electrical power is set from ∼75 W to ∼62 W (third and fourth rows). For an applied power of 62 W, emission zones are in the form of lateral stripes which are attributed to a standing wave field [179, 180]. Furthermore, over the bottom of the bath, there is a void of emission which is opposite of the SCL signals obtained in higher pressure amplitudes (first three rows in Fig. 4.12). As it is mentioned before in SCL emission for a 6 cm filled bath, here also the expulsion of cavitation bubbles from high-pressure zones can be the mechanism interpreting the dark zone above the bottom surface, since the increase of the rate in the secondary Bjerknes force is more than that of the primary Bjerknes force as the sound pressure amplitude increases. Bubbles become larger, form clusters, and are repelled from the high pressure regions [175]. Therefore, high-pressure zones become dark or emit very dim light, whereas lower-pressure regions emit brighter light. This mechanism explains

the SCL profiles observed from applied power of 62 to 13 W (fourth to eighth row), with some slight differences. Some double layers, reflecting jellyfish bubble structures above and below pressure nodes, turn into large circles enclosing the pressure nodes [171], or take some different shapes, whereas the others simply disappear. A decrease in the sound pressure amplitude might lower the size of the bubbles. Smaller bubbles have less dissolved gas content and they collapse less violently which might result in a decrease in the final temperature of bubble interior. This in turn affects the reaction rates of sonochemical activity and reduces the $HO^{\bullet}$ radical dissociation [181]. Consequently, less luminescence intensity is expected. On the other hand, since the bubbles are smaller as the sound pressure decreases, they are no longer repelled from high-pressure zones since the primary Bjerknes force becomes more dominant. As a result, for lower sound pressures, there is no (or weak) luminescence observed in the low-pressure zones. That is why bubbles emit SCL in antinodes under very low acoustic pressures as it is seen in the images of the last row in Fig. 4.12.

To show the change in the luminescence emission profile better, a larger scale of both images (Fig. 4.12a.iii, a.iv, and a.ix) are given in Fig. 4.12.a, b, and c. The SCL image is depicted in Fig. 4.12.d with an overlaid simulated pressure map. It is seen that the height and width of the maximum pressure over the surface show a correlation with the dark zone over the surface observed in the SCL emission image. As mentioned before, no luminescence is detected in the highest pressure zone which is attributed to bubble shielding. Above the first maximum pressure, the two double-layer structures of SCL images do not look coherent with the second and third maxima of the simulated map. Bright lines fall between the high-pressure zones of the simulation. This can be explained by the effect of the Bjerknes forces which leads bubbles to be repelled from the high-pressure zone. As a result, luminescence emission is detected at the lower pressure regions. On the other hand, it has to be noted that numerical simulations do not take all parameters into account such as real boundary conditions, bubble distribution, real radius and the shape of bubbles, and non-linear bubble oscillations.

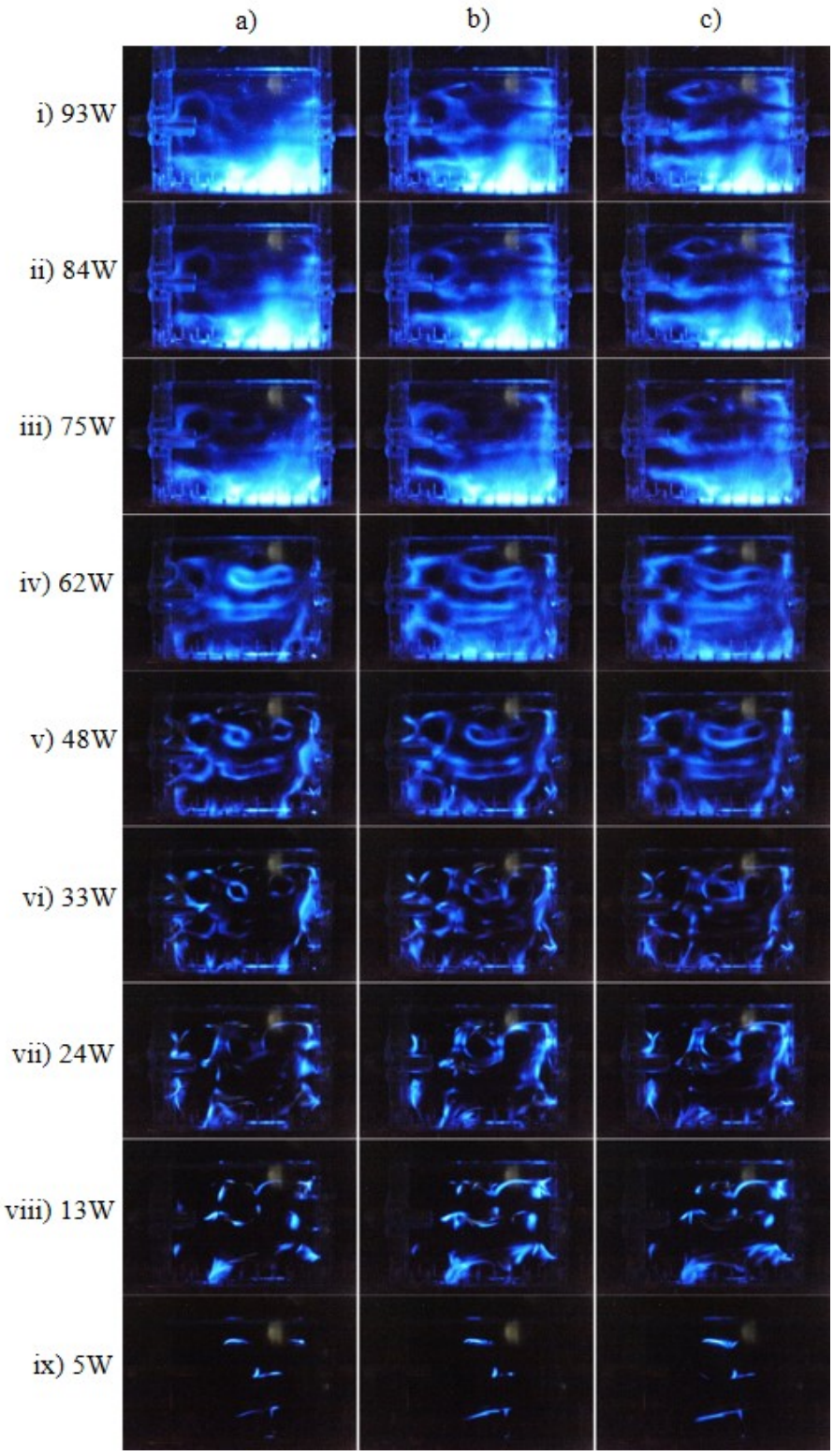
a)
b)
c)
i) 93W
ii) 84W
iii) 75W
iv) 62W
v) 48W
vi) 33W
vii) 24W
viii) 13W
ix) 5W

Figure 4.12. Ar-gassed luminol filled container is sonicated at 25.7 kHz with varying electrical power input. Each column refers to set of images captured with a digital SLR camera, with the exposure time of 30 s. Each row corresponds to different function generator amplitudes from 500 mV to 100 mV with the steps of 50 mV (from **i)** to **ix)** ; corresponding to the delivered electrical power (the difference between forward and reflected power) of approximately 93, 84, 75, 62, 48, 33, 24, 13, and 5 W. Since the exposure time is 30 s, each column is recorded in 4.5 minutes, and performed one after another consecutively as column **a)**, **b)** and **c)**.

The sound pressure maps obtained via a hydrophone measurement and numerical simulation are embedded in the SCL image observed at the applied power of 62 W in Fig. 4.13.d and 4.13.e, respectively. In Fig. 4.13.d, it is seen that SCL emissions match with lower pressure regions which are just surrounded by the maximum pressure zones (red). A dark (or very dim) region is seen over the transducer surface up to 40 mm which is correlating with the first high pressure zone obtained via the simulation. This correlation might be explained by the bubble shielding effect. Between the first and second maximum pressure zones of the simulated map, the SCL signal mostly comes from some walls and corners. As the second maxima zone of both simulated and measured maps comes, the SCL emission profile coincides. According to the overlapping regions, one can say that the double-layered structure matches with the second pressure maxima. The darker region in the middle of the double layer structure corresponds to a higher sound pressure field of the second maxima (orange color code), while the bright emissions come from rather lower pressure locations (yellow color code). The reason is that the bubbles become larger, and they tend to coalesce by the secondary Bjerknes force, and these bubbles are attracted towards antinode by the primary Bjerknes force. Eventually, bubbles become larger than the resonant size and the direction of the primary Bjerknes is reversed; so that, bubbles are expelled from the antinode. Consequently, antinode regions have a very low population of bubbles, if any. In fact, in experimental conditions, sound pressure exceeding the cavitation threshold leads bubbles to oscillate non-linearly [172]. Hence, even if the bubble radius is constant, the primary Bjerknes force acting on a bubble smaller than the resonant radius is reversed from attractive to repulsive [178]. The next high-pressure zone of the map is coherent with the second double layer. In between these two high-pressure regions, no SCL signal is recorded and the map shows a blue color code that indicates minimum pressure falling to zero. The emission lines overlap with the form of the last high-pressure region. Again, the red color code inside the pressure zone indicates higher pressure while the yellow color around it points out lower pressure. On the other hand, the SCL emission matches with the yellow zone, whereas the red zone correlates with the dark region between the luminescent stripes. Double layer emissions are attributed to the bubbles repelled from an antinode and producing $HO^{\bullet}$ radicals around the nodes. This can be explained with the same mechanism driven by the Bjerknes forces acting on the bubbles as mentioned.

The SCL image obtained from the lowest pressure amplitude which corresponds to the delivered electrical power of 5 W is given in Fig. 4.13.c. The SCL profile changes with a different amplitude pressure. For better comparison, the simulated sound pressure map is embedded into the SCL image and depicted in Fig. 4.13.f. Bright lines (streamers) of the SCL image obtained with 5 W correlates with the high sound pressure regions; while, the SCL image of 62 W has the dark or no emission in the maximum pressure zones (See

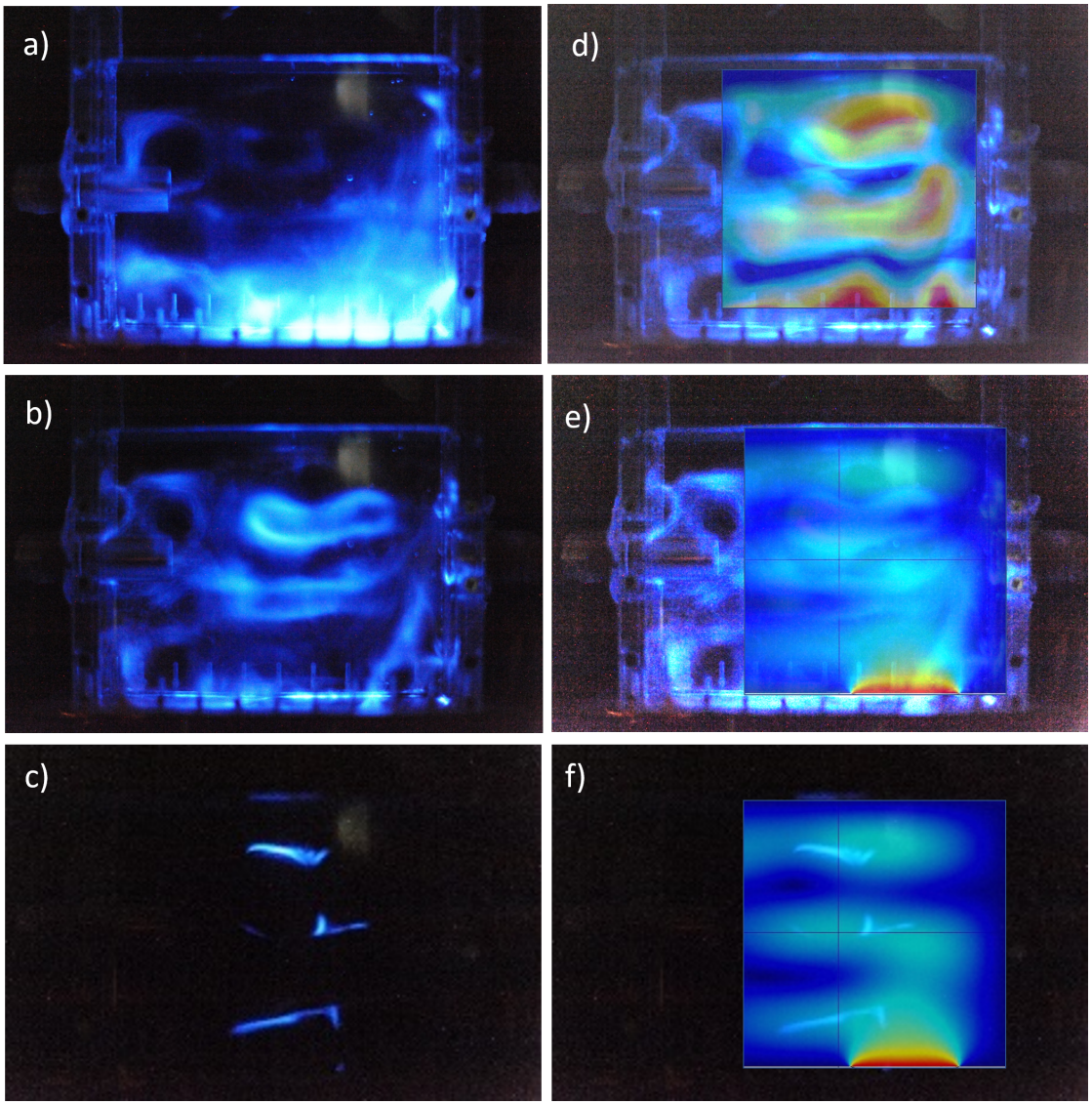

Figure 4.13. SCL signals obtained from a luminol-filled ultrasonic bath for three different power inputs. The bath is filled up to 11 cm, and the transducer is operated at 25.7 kHz with the electrical power of (the difference between forward and reflected power) **a)** 75,W, **b)** 62 W, and **c)** 5 W. Luminescence emissions are captured with a digital SLR camera with an exposure time of 30 s. **d)** The sound pressure map obtained via a hydrophone (Figure 4.12.a) is superimposed onto the luminescence emission image captured with a power input of 62 W. The numerically simulated pressure map (Figure 4.12.b) is overlaid onto the **e)** SCL image captured with an electrical power 62 W and **f)** 5 W.

Fig. 4.13.e.). Under low acoustic pressures, cavitation bubbles become smaller which leads to less violent collapses and weaker luminescence emission (or no emission). Moreover, bubbles are no longer repelled from high-pressure zones, since the first Bjerknes force exerts on bubbles stronger than the second Bjerknes force. Consequently, the overall luminescence intensity diminishes with the decrease in the sound pressure amplitude and the bubbles emit light at higher-pressure regions.

4.2.2.3 Sonochemiluminescence from stacked channels

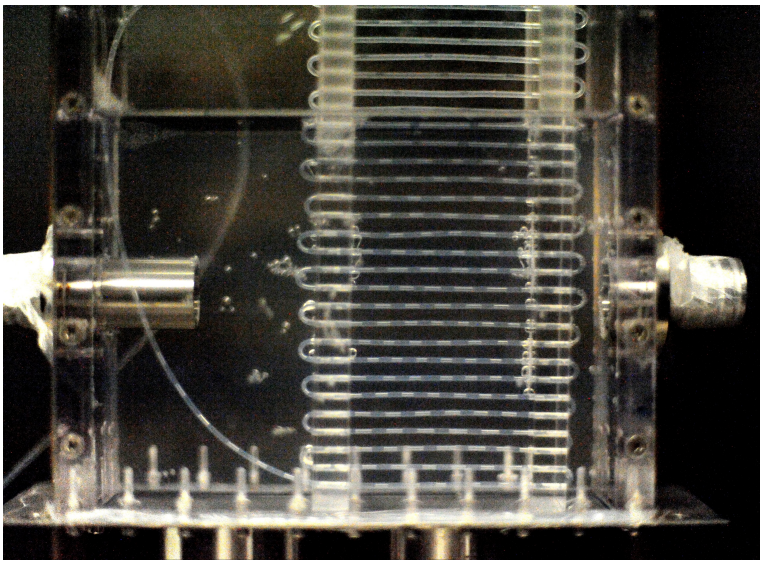

Figure 4.14. Photo of stacked channels before sonication. PFA tubing is placed horizontally as lines by a polycarbonate holder which has holes on each side. The stacked channels are placed into an ultrasonic bath along the center of the transducer surface and the bath is filled with water up to 11 cm. Channels directly face the bottom of the bath without any medium in between, and the polycarbonate holder does not have any contact with the bottom plate of the bath. Channels are filled with a luminol-air slug flow, with about the same volume ratio of both phases. Dark and bright pockets in channels correspond to luminol pockets and air gaps, respectively.

PFA channels are submerged into the ultrasonic bath via a polycarbonate holder as described in detail in Section 3.1.2.2 and a photo of the channels is given in Fig. 4.14. The bath is filled with water up to a height of 11 cm, and the channels are placed into the ultrasonic bath along the center of the transducer surface. The smaller the channel size the lower the volume loads; thus, luminescence intensity is not expected to be as bright as in bulk luminol solution. However, as the channels filled with only luminol solution is sonicated, no luminescence is detected. Although the luminol solution is prepared by first degassing and then Ar-gassing in a closed system in order to enhance the light intensity, it is considered that luminescence emission can probably still be weak and beyond the limits of the SLR camera. Hence, cavitation activity is investigated via a high-speed camera to verify the existence of cavitation bubbles. No cavitation bubble is observed from channels only filled with treated luminol solution. To initiate cavitation in channels, a luminol-air slug flow is formed inside the channels by alternatively pumping two phases. Luminol-air can be distinguished through transparent channels, where darker pockets in the channels refer to luminol and bright (white) ones correspond to air gaps. The slug flow exhibits regular formation and the ratio of lengths of both phases are almost equal in each line of the channels in the water-filled bath. Then the flow is stopped and channels are sonicated at 25.7 kHz with varying amplitudes.

SCL images from the channels are captured with an exposure time of 30 s and depicted in Fig. 4.15. As a comparison to SCL from the ultrasonic bath (see Fig. 4.12), the transducer is driven at different electrical amplitudes in the range of 500 mV to 100 mV, from

a) to i), respectively. According to the change in electrical amplitude, delivered power to the bath changes between 93 W to 5 W (which is the difference between the forward and reflected power). Due to the small volume in the channels, which are also about only half full with luminol, weak SCL signals are obtained. For better comparison, the brightness/contrast of the images is adjusted without any relative change between them. It must be noted that the channels are sonicated for 4.5 min which can be considered as a long operation time leading to a distortion in the form of the luminol-air slugs. (*i.e.* transition from slug to churn by cavitation). It must be noted that sonication changes the physical and chemical conditions, such as the ratio of lengths of luminol-air slugs, two-phase boundary, and distribution of dissolved gases within the channels that affect the cavitation activity and luminescence intensity.

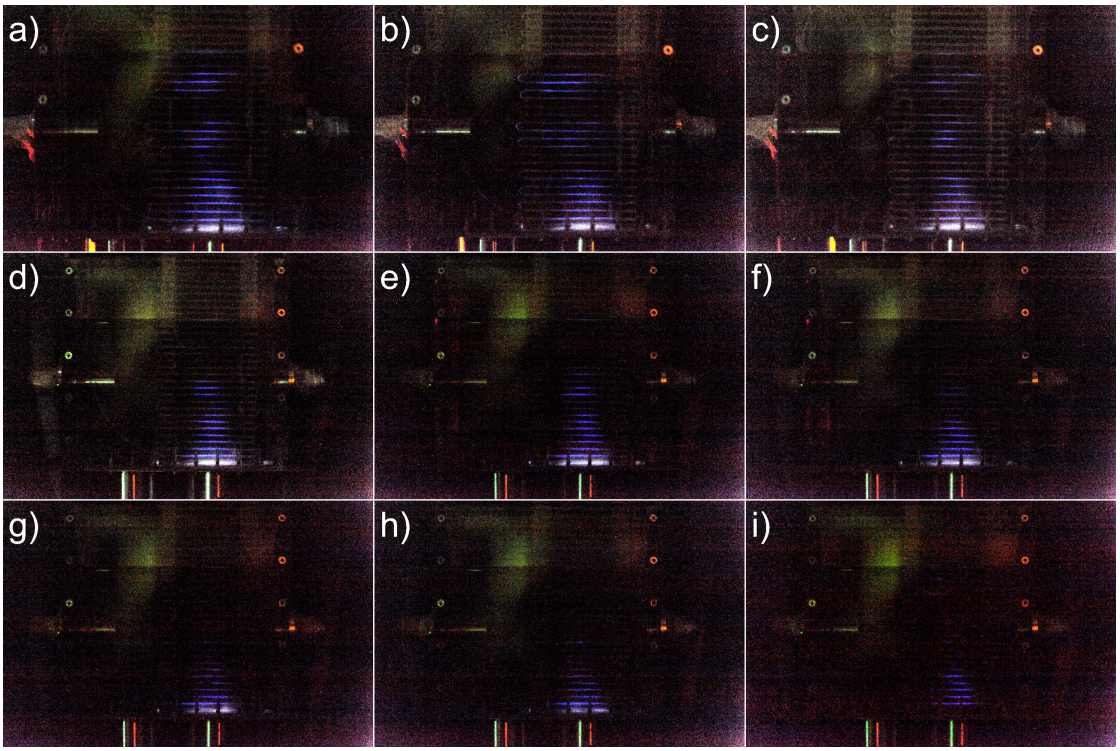

Figure 4.15. SCL from luminol-air-filled channels submerged into an ultrasonic bath filled with water up to a height of 11 cm. SCL images are obtained in dark conditions. After merging all images into a single figure, overall brightness/contrast is adjusted in order to distinguish the differences between each image. Luminol and air slugs are formed, then the pumps are stopped. Luminescence emissions are recorded with an exposure time of 30 s. Channels are sonicated at 27.5 kHz with different amplitudes. From **a)** to **i)**, the applied electrical amplitude changes from 500 mV to 100 mV with a decrease of 50 mV, respectively. Corresponding applied power (the difference between forward and reflected power) is about 93, 84, 75, 62, 48, 33, 24, 13, and 5 W.

As it is seen from Fig. 4.15.a-4.15.i, the overall intensity of the SCL signal decreases with the decrease in applied amplitude. In the first row of images (93 to 75 W), the SCL signal from the channels is observed as three noticeable groups along the positioning of the transducer. The intensity of emission decreases slightly within the decrease in applied power. On the other hand, the brightest emission comes from the group of channels which are closest to the transducer surface since the highest sound pressure

is expected over the surface of the transducer as shown in Fig. 4.11. Signals coming from the second and third groups of channels have less intensity than the first due to their longer distances to the transducer; since sound pressure amplitude decreases farther from the transducer surface. For the second row of images Fig. 4.15.d-4.15.f, no SCL emission is detected from the channels furthest away from the transducer. On the other hand, the second group slowly fades away and slightly merges with the group of channels closest to the sonication surface. In the last row of images in Fig. 4.15.g-4.15.i, SCL is only detected from channels close to the transducer. SCL intensity also diminishes and reaches the minimum of all nine images. It must be taken into account that sonication alters physical and chemical conditions inside channels which have an impact on luminescence intensity, such as quenching of luminescence, and ultrasonic degassing as it is shown as consecutive columns in Fig. 4.12. Additionally, the Ar gas content in luminol pockets decreases since there is a continuous exchange of dissolved gases in a two-phase boundary during sonication. Lower volumes of Ar in the bubble interior result in weaker luminescence intensity. SCL observations from the channels have some other parameters to consider which are not included in the case of luminescence emission from the bulk liquids. The presence of tubes affects the cavitation conditions, so the luminescence emission. Physical changes such as pressure difference between the inlet and outlet of channels, the distribution of two phases and dissolved gases have also an effect on the decrease in overall SCL intensity from Fig. 4.15.a to Fig. 4.15.i.

In the previous section, three different emission profiles observed from luminol-filled ultrasonic bath are discussed and shown in Fig. 4.12. It is discussed that depending on the pressure amplitude, bubbles are expelled or attracted from antinodes which results in different profiles. On the other hand, in the case of a SCL emission from luminol-air slugs in channels exhibit only one type of pattern as different pressure amplitudes are applied. Generally speaking, the only similarity between SCL observations from sonicated channels and the bath is the decrease in luminescence intensity as the applied power decreases. For better comparison, SCL images from luminol solution-filled ultrasonic bath with the electrical power of 75 W and luminol-air filled channels submerged into an ultrasonic bath for the power of 93 W are given in Fig. 4.16a and b, respectively. Patterns observed in SCL images from channels sonicated with 75 W and 93 W are the same, with only a difference in brightness; hence, the one driven with 93 W is selected for comparison. At first glance, emissions in both images are considered alike regarding longitudinal positioning of the double-layered signal in Fig. 4.16.a, and the second and third groups of emission in b. To compare both images, a cut line of 11 cm is placed longitudinally along the middle of the transducer in both images. RGB intensities of both images are read from the bottom of the ultrasonic bath to the water height of 11 cm and given in Fig. 4.16.d and 4.16.e, respectively obtained from bath and channels. A comparison of the two graphs show that there is a shift in positioning of SCL emissions. Cavitation bubbles in 'bulk liquid' are free to move, hence they are deployed concerning pressure distribution inside the bath. As discussed before, dark regions between each parallel emission layer refer to high-pressure zones. Since bubbles are repelled from antinodes, they glow in lower pressure regions around antinodes (Fig. 4.16.a). On the other hand, the existence of channels can change the profile of the sound field distribution inside the bath. Although theoretically acoustic impedance of PFA tubing is nearly the same as that of water; geometry, positioning, thickness, and the number of channels have exper-

imentally an impact on the sound field (damping effect). Bubbles confined inside the channels are expected to have different oscillation characteristics than the ones oscillating freely outside the channels. Dynamics of the bubble oscillating in a circular tube have been given in Eq. 2.20 by introducing an additional term to the Rayleigh-Plesset equation and the effect of the presence of the tube to the bubble size vs time curve is previously discussed for a bubble in loop channel (see Fig. 4.10). Confined bubbles are supposed to be smaller than the ones in bulk liquid, since the pressure inside the tube is lower. They do not expand as much as larger bubbles and they are expected to collapse later. Moreover, the smaller the bubbles the lower the compression rate which means less violent collapse takes place. This results in lower temperatures during the collapse, with reduction in sonochemical activity leading to luminescence emission. Additionally, smaller bubbles have less volume of dissolved gas content and consequently less $HO^{\bullet}$ radical dissociation occurs via cavitation. Hence, the interaction of radicals and luminol molecules decreases. As a result, confined bubbles are expected to emit less luminescence than the ones in the bulk liquid.

Bubbles in bulk liquids and channels do not only show differences in volume oscillations but also bubble motions. Bubbles in bulk liquids are free to move in space depending on the applied pressure field inside the liquid. On the other hand, cavitation bubbles inside the channel are restricted by walls. This might be the main reason for the shift in RGB intensity profiles between Fig. 4.16.d and Fig. 4.16.e. The SCL image from a luminol-filled ultrasonic bath is compared with the simulated pressure field map previously (see Fig. 4.13). It is seen that high-pressure zones are surrounded by a double-layer emission where blue color peaks are saturated between the heights of 35 to 55 mm and 65 to 85 mm above the transducer surface in Fig. 4.16.d. This means that both double-layered structures elongate by a similar amount. Moreover, there is a very thin layer of light emitted on the surface due to the bubble shielding effect. In the case of an emission from the channels, according to Fig. 4.16.e, the peak of the blue color shows a strong emission which starts from the channels close to the surface of the bath where the transducer is attached to and gradually weakens towards a height of about 40 mm. This first emission region is coherent with the sound pressure map as it is seen from Fig. 4.16.f. Since the bubbles are vertically restricted by the tube walls, they are not able to move depending on the acoustic force exerted on them. As the first high-pressure zone is passed and a relatively lower pressure is expected according to the sound pressure map in the bath, in Fig. 4.16.e no blue light emission is detected until about 50 mm which corresponds to the pressure node. The SCL emission recorded from second and third group of channels come from the heights of about between 50 to 70 mm and 90 to 100 mm, which are attributed to the second and third maxima of the pressure amplitude given in Fig. 4.16.f. According

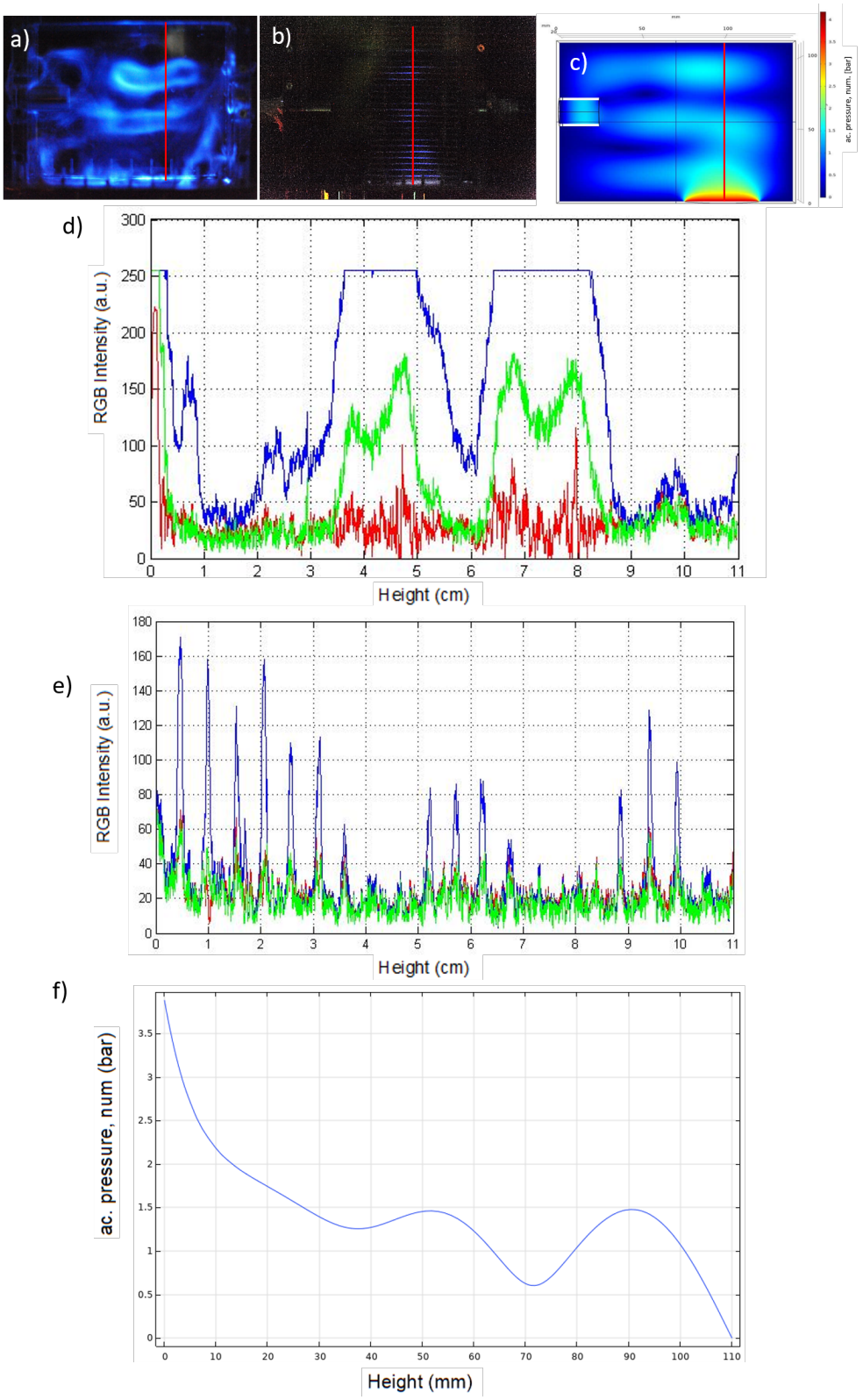
a)
b)
c)
ac. pressure, num. [bar]
d)
RGB Intensity (a.u.)
Height (cm)
e)
RGB Intensity (a.u.)
Height (cm)
f)
ac. pressure, num (bar)
Height (mm)

Figure 4.16. Cutline through SCL images obtained from a luminol-filled bath, luminol-air slug-filled channels, and a sound pressure map. The red line indicates the exact position of the cutline. The images are captured via an SLR camera with an exposure time of 30 s. **a)** The bath is filled up to 11 cm with a luminol solution and sonicated at 25.7 kHz with an electrical amplitude of 350 mV. **b)** The channels are filled with a luminol-air slug flow and submerged in an ultrasonic bath filled with 11 cm of water. The transducer is driven at 25.7 kHz with 500 mV. **c)** A simulated sound pressure map for the ultrasonic bath filled up to 11 cm (see Fig. 4.11). **d, e)** Changes in RGB intensity above the transducer obtained from the SCL image given in a) and b), respectively. **f)** Acoustic pressure above the transducer obtained from the simulated map in c).

to the RGB graph obtained from the SCL emission from channels (Fig. 4.16.e), the first and second peaks of the signal (from surface to top) are closer to each other than the second and third peaks. This coincides with the sound pressure map. According to the RGB profile of the simulated map, there is a smooth transition to the second maxima hump while the pressure drop between the second and third maximum regions falls almost to zero. The reason is that bubbles inside the channels are smaller at lower sound pressure amplitudes. In such a case, they are not expected to collapse hard, which lowers the luminescence intensity if they emit any. As the graphs of the SCL images obtained from channels and bath are compared, one can say that the second and third high-pressure zones are coherent with a slight shift. The reason is that the bubbles in a bulk luminol solution move in space according to the acoustic forces acting on them. On the other hand, bubbles inside channels feel less pressure and are vertically restricted by channel walls.

4.2.2.4 Phase shift between bubbles oscillating inside channels and an ultrasonic bath

Investigating bubble structures inside channels is a challenging task due to cavitation in the coupling liquid. The tubing is rounded, and both bubbles inside and outside the channels tend to attach to the channel walls. When recording at a relatively lower speed, which is two to four frames per one acoustic driving period T, it is simpler to focus the camera on bubbles oscillating inside the channels. The recording area is large enough to differentiate between bubbles located inside the channel and those in the coupling liquid. However, when recording at higher frame rates to capture more stages of a bubble oscillation during one driving period, the recording area becomes much smaller, and bubbles oscillating outside the channels partly prevent clear imaging inside (see Fig. 4.17). It also becomes difficult to clearly distinguish which bubbles are inside the channels, as there may be a (too) small difference in focusing. This becomes particularly challenging when both inside and outside bubble clusters are approximately in the same 2D plane, meaning they have an equal distance from the microscope. Additionally, some bubble clusters are close or attached to the front side of the channel, while others are positioned behind. The different positions of bubble clusters along the focal axis also make focusing challenging. Looking for a reflection from a bubble wall becomes the only reference point for focusing. In some recordings, it still remains unclear whether the cluster in focus is oscillating inside or not. Therefore, analyzing bubble oscillations by extracting and tracking a nearly stationary and relatively isolated bubble, without being blocked by outside bubbles over several driving periods, becomes extremely difficult.

Additionally, the variability of bubble dynamics in or near a cluster of bubbles is high, as shown below.

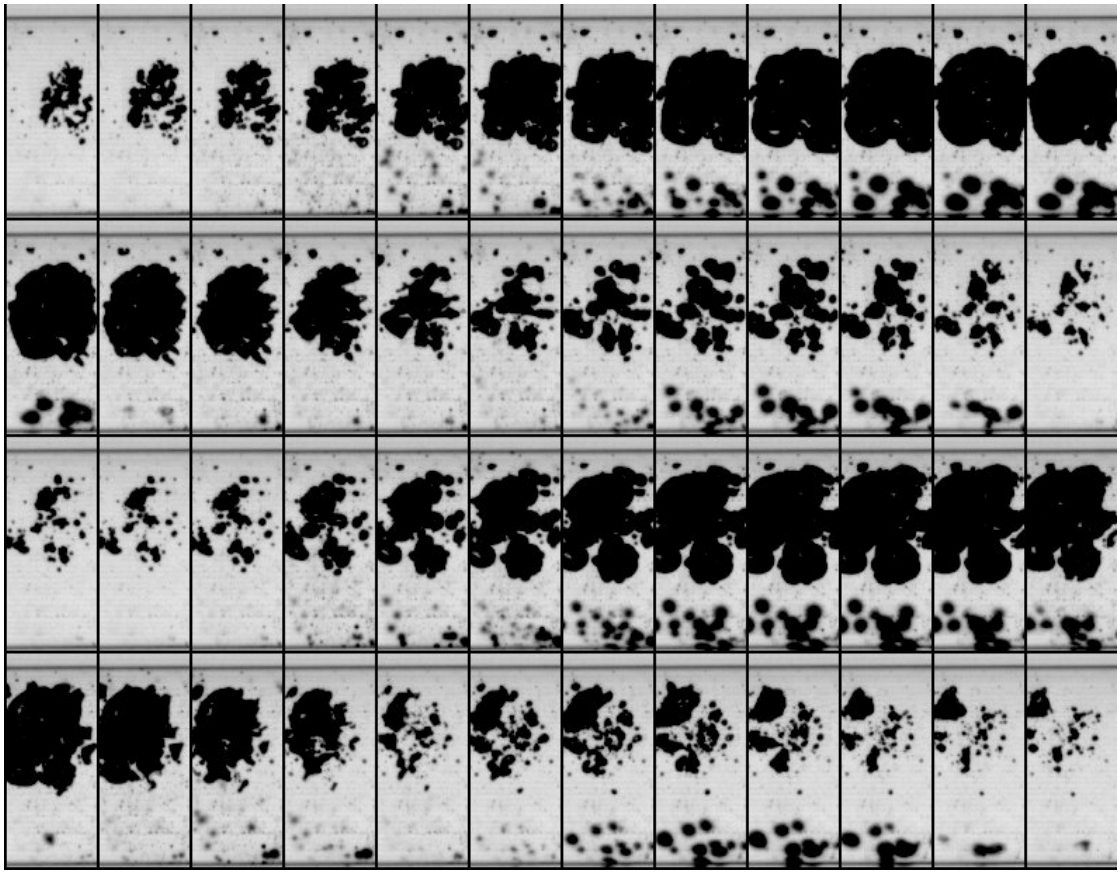

Figure 4.17. Consecutive image series of bubbles oscillating inside and outside the channel. The frame rate of the recording is 300k fps. The transducer is driven at 25.7 kHz with 500 mV. The channel diameter is 0.8 mm, the flow rate is approximately 10 μL/s (towards the right). The bubble cluster in the upper part of the channel is oscillating inside, whereas the bubbles in the lower part of the channel are outside ones. Each row corresponds to one driving period. Strong acoustic pressure excitation leads to nonlinear oscillations of bubbles inside and outside the channel, exhibiting period doubling sequences [182].

Thus, visualizing and high-speed imaging of cavitation bubbles and structures inside the flow tubes submerged in the ultrasonic bath is demanding due to cavitation activity in the coupling liquid, i.e. the liquid outside the tubes. Here, distilled water is used as the coupling liquid, and it has also been degassed to lower the nucleation probability and the resulting cavitation bubble density; compare Sec. 2.1.4. Increase of cavitation threshold or at least reduction of cavitation activity by degassing is well known, since dissolved gas can act as nuclei or support nuclei growth by rectified diffusion [183]. Thus, reducing the gas content of the liquid can restrict pathways of increased cavitation activity [184, 185] and achieve better imaging conditions for channels. However, since the bath reactor has an open top and accordingly a free surface in contact with air, a certain re-gassing rate cannot be avoided [186]. Consequently, for longer operation times, increasing cavitation activity in the coupling water in the ultrasonic bath can be observed.

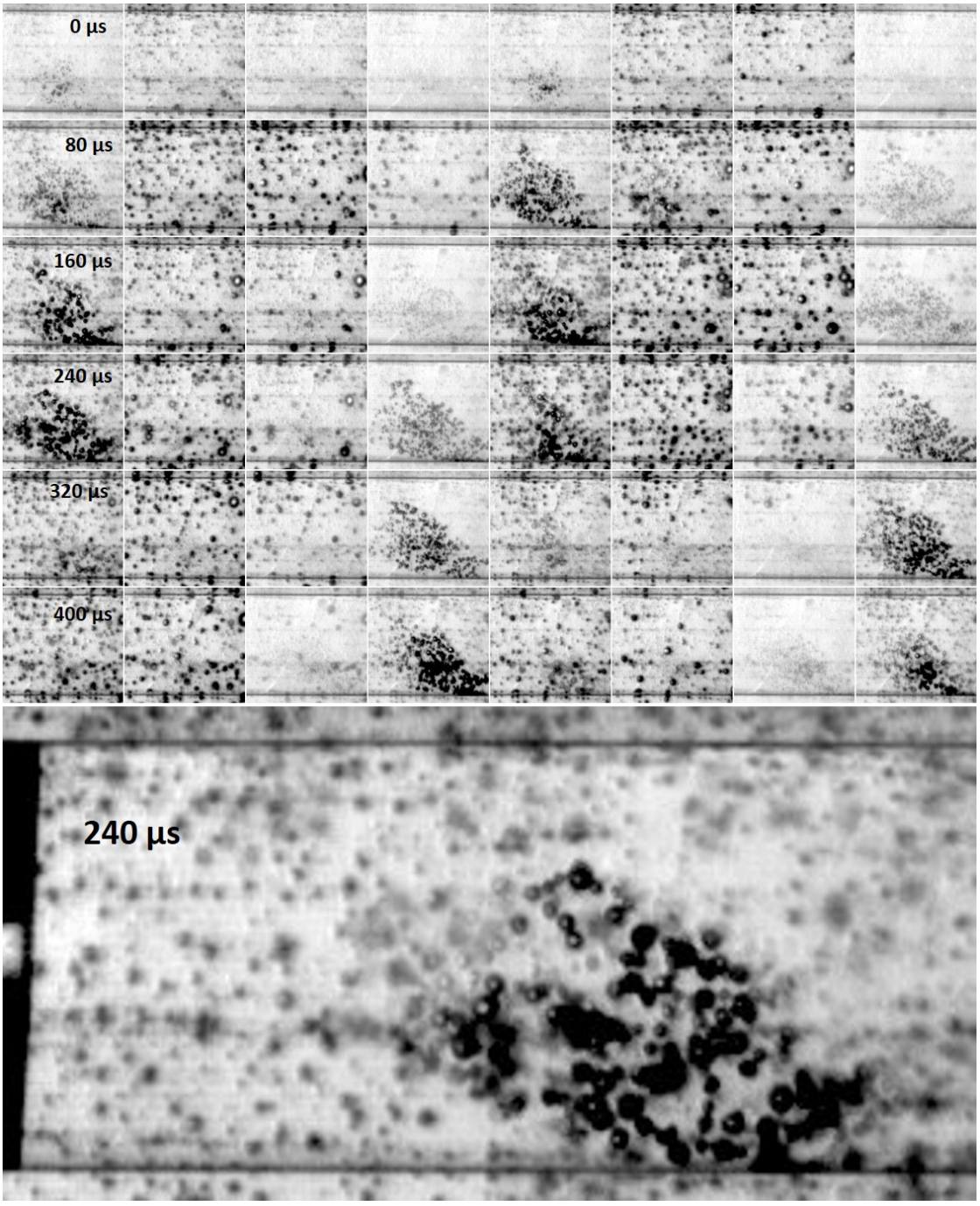

Figure 4.18. Plain high-speed image series of the tube under cavitation conditions. The image sequence starts from the top left and progresses towards the right, row by row. The recording is done at 100k fps, with an exposure time of 1 μs. Both cavitation bubbles inside a water slug in the channel, and bubbles outside in the water-filled ultrasonic bath are visible. The outside water has been distilled and degassed, but still cavitation occurs. The water-air slug flow in the tube runs at about 10 μL/s, which corresponds to a flow speed of about 20 mm/s. The frame height is about 1 mm, the inner diameter of the channel is 0.8 mm. The transducer is driven at 25.7 kHz with an electrical amplitude of 500 mV. The air-water interface is visible on the left in the lower image.

Apart from suppressing cavitation in the coupling liquid, another effect helps for visualizing the channel cavitation. Indeed, it turns out that bubbles within the channel and bubbles within the coupling water are oscillating with a certain phase shift. This is investigated closer in the following. High-speed recordings of cavitation bubbles that occur inside and outside of the flow channel are given as a consecutive image series in Fig. 4.18. The lumen of the channel can be easily distinguished in each frame as the region between the tube wall, appearing as darker lines near top and bottom. The oscillation of the bubble volumes leads to periodic appearance and vanishing of the bubble shades, well discernible at this recording speed and exposure time. Bubble shades visible "on" (actually in front of or behind) the tube wall region to top or bottom of the frames are without doubt outside bubbles, and bubbles gathering near the inner side of the tube wall are within the channel, since they are clearly stopping at the wall, not crossing this line. A magnified view of a recorded frame with the full width is given below the series, where also the next air-water interface can be seen to the left. Since recording is at 100k fps (frame-to-frame time $10\,\mu$s), and the transducer is driven at 25.7 kHz (acoustic period $T = 38.9\,\mu$s), each interval containing 4 frames corresponds to just a little bit more than one acoustic oscillation period (namely $1.1\,\mu$s, corresponding to $0.028T$) . Therefore, every 4^{th} frame looks quite similar, and one can see a rather small structural change over the interval of about 6 driving periods. In particular, there is a bubble cluster inside the tube and somehow more close to the lower wall. This cluster is well visible in the expanded state in the 5^{th} frame of the second row. Due to the repetition stability of the structure and the slight time shift after 4 frames, one can follow the expansion of the cluster "on a faster time scale as the camera frame rate" in frames 1, 5, 9, 13, 17 and 21, corresponding to time shifts of $0\,T, 0.028\,T, 0.056\,T, 0.084\,T, 0.112\,T$ and $0.140\,T$. A very close inspection, though, shows that the variability on the single bubble level is much higher than for the overall structure, and few individual bubbles within the cluster can be re-identified four frames later. This is illustrated a little bit later below.

The main message of Fig. 4.18 is, however, the obvious phase shift of the inside bubbles (represented by the cluster) and the outside bubbles that oscillate in the coupling liquid. This can be perceived already by looking at the bubbles expanding "on" the wall regions. These are large (expanded), for instance, on frames 10 and 11, when the cluster bubbles from frame 9 have already disappeared due to collapse. In particular, there exist "lucky phase shifts" like in frame 13 (!), where the inside bubbles are expanded and well visible, but the disturbing outside bubbles remain small or invisible. This fact has been employed in many recordings where only inside bubbles are of interest, and technically the "lucky phase" was fixed for the recordings by using an external trigger signal, derived from the acoustic driving via a delay generator.

To compare the expansion and collapse phases of bubbles in the channel and in the bath more quantitatively, an image processing analysis of regions of inside and outside bubbles has been carried out. For selected rectangular regions, the average grey scale is extracted from a sequential part of the movie. One rectangle (black) is located in a region where no inside bubbles had been detected, the other rectangle (red) includes the cluster of inside bubbles (this region, however, is additionally affected weakly by outside bubbles). Low level (darker) corresponds to more (expanded) bubbles, and higher level (brighter) indicates less or smaller or collapsed bubbles. A re-arranged image sequence according

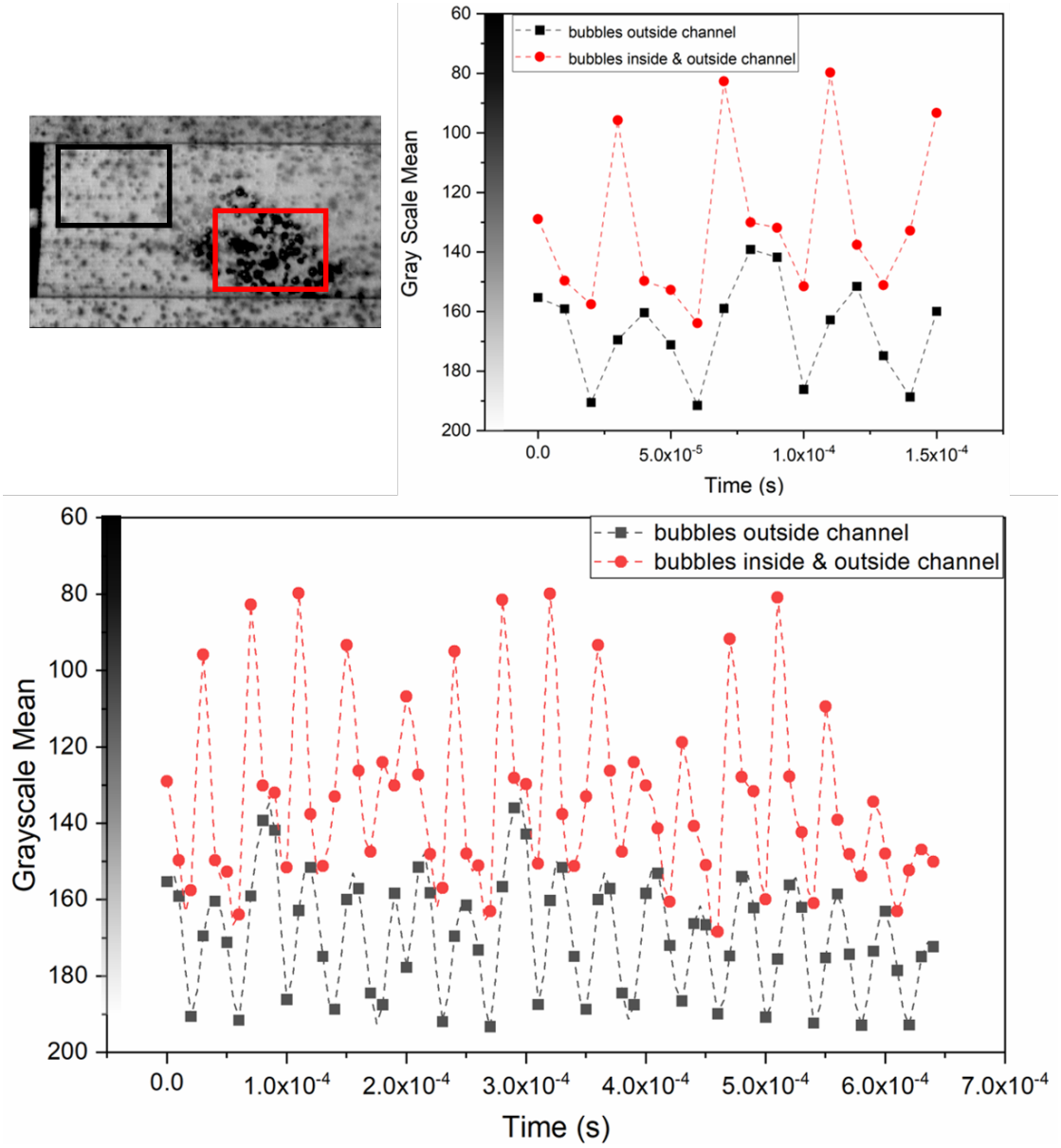

Figure 4.19. Grey scale analysis to compare oscillations of cavitation bubbles inside the channel and in the coupling liquid. On top, the last frame of Fig. 4.18 is presented, showing black and red identical rectangles (area of 300x240 pixels) representing the data collection regions. The red frame corresponds to the red data point in the graphs, indicating the mean brightness/contrast values from both the bubble cluster inside the channel and in the coupling liquid. On the other hand, the black frame corresponds to the black data points in the plots, where the brightness/contrast values primarily come from bubbles outside the channel. The upper graph displays the mean grey scale plot from both areas for 16 consecutive frames, while the lower graph shows the same analysis for 64 consecutive frames. The time interval between two data points is 10 μs.

to relative driving phase is shown in Fig. 4.20, and the result of the re-sorted grey scales is presented in Fig. 4.19. Note the inverted vertical axis, meaning that a higher point/curve corresponds to larger bubbles. One recognizes considerable oscillations of

the levels, indicating strong bubble volume oscillations with large expansion and high compression in the collapse phase. This relates well with the observations of chemical activity of the cavitation bubbles. When checking the phases of inside and outside bubbles, one can perceive a certain shift, but the temporal resolution is not really good. In an attempt to increase the resolution, subsequent frames have been resorted into a time interval of $2T$ be taking the absolute (known) time of each frame by modulo $2T$; see Fig. 4.21. Effectively, this way the relative phase to every second up-going zero crossing of the driving has been extracted. If the image sequence would be absolutely periodic, a clean curve of the grey levels vs time would appear for inside and for outside bubbles. However, since the system is noisy and of course only approximately periodic on the scale of several T, one gets somehow scattered grey scale levels. Still, certain "oscillation curves" of inside and outside bubbles can be seen in the figure. While the outer bubbles in the coupling liquid create a rather sinusoidal grey level curve (blue markers), the inner bubbles (green crosses) follow roughly an "expansion-collapse-afterbounce" curve like the radius-time curve given in Fig. 2.6. With respect to the expansion phase, the inside bubbles seem to expand earlier, and the collapse happens faster than for the neighboring bubbles in the coupling liquid.

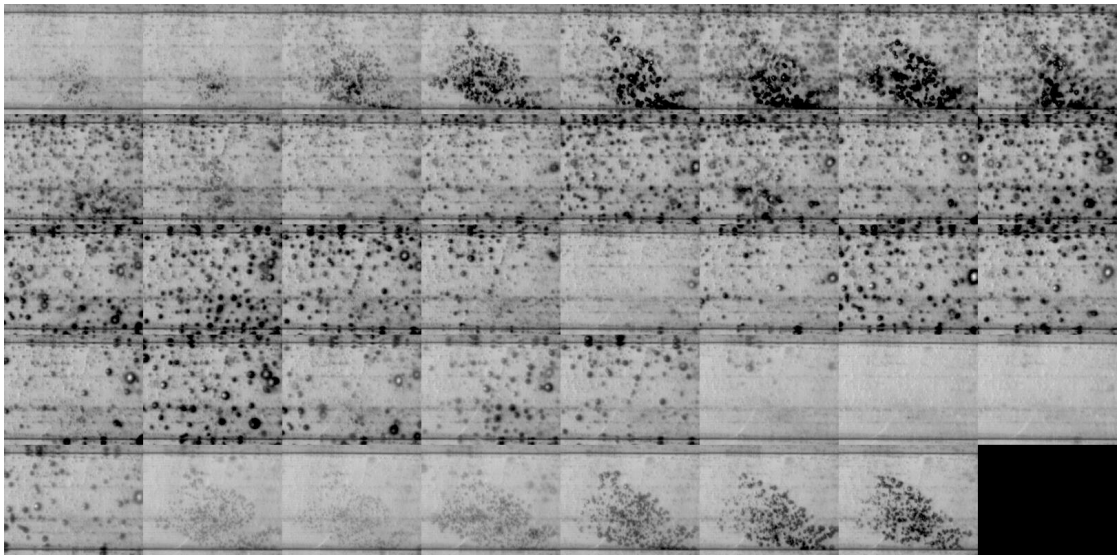

Figure 4.20. Several (39) frames from Fig. 4.18 sorted in an ascending relative phase to the acoustic driving phase over one acoustic period T. The expansion and collapse of the cluster inside the tube can be observed with apparent higher time resolution. Since the bubble dynamics and positions are not fully periodic, the sequence exhibits some "jumps".

A full explanation of the phase shift cannot be given yet. On one hand, the driving pressure between inside and outside the tube should be well in phase, because the spatial distance of the order of a mm is small compared to half of the acoustic wavelength ($\lambda \approx 54\,\mathrm{mm}$, $\lambda/2 \approx 27\,\mathrm{mm}$). This holds even if the wave amplitude is weakened inside the tube (some part will be scattered off because of slight impedance mismatch between PFA and water, some part might be attenuated by damping in the tube wall). On the other hand, if the inside bubbles feel less driving pressure, they should expand less and collapse earlier - at least, if the bubble equilibrium sizes are similar inside and outside. An earlier collapse fits with the observation, but an earlier expansion would not

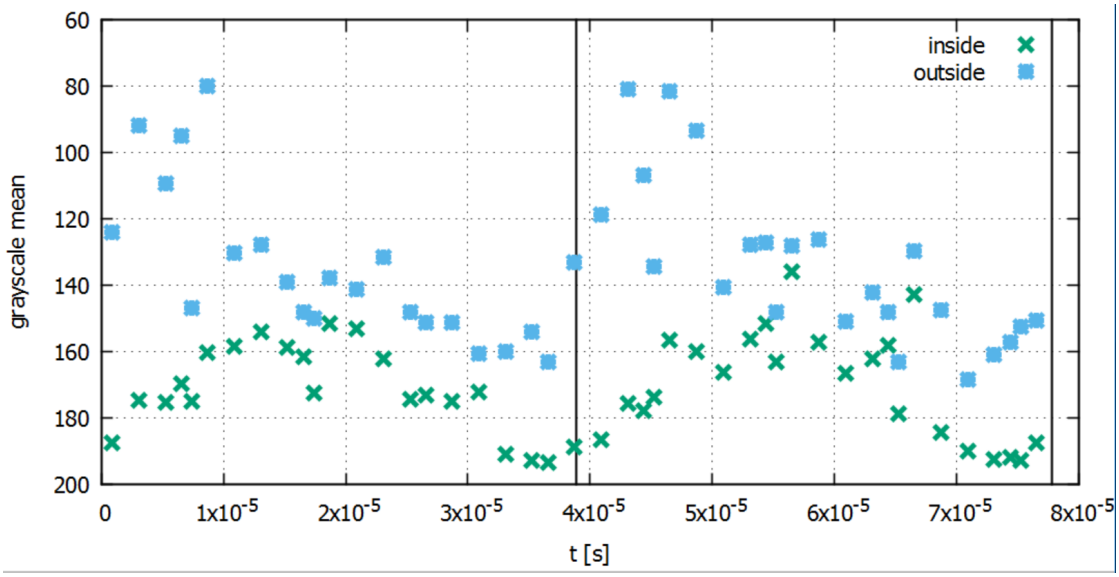

Figure 4.21. Grey levels of the indicated regions from Fig. 4.19, now resorted modulo $2T$ = two driving periods. A roughly coherent expansion-collapse oscillation can now be perceived for bubbles outside (green) and inside (blue) the channel.

really be predicted by solely reducing the pressure amplitude. Thus, additional factors might contribute. The equilibrium radii might be larger in the tube (and then the bubbles would be expanding somehow earlier). Further, the bubbles are inside the tube (restricted flow conditions, compare the modified bubble oscillation model for bubbles in a tube, Sec. 2.1.3 and Sec. 4.2.1.4. Additionally, the inside bubbles belong to a quite dense cluster of bubbles, and this might modify bubble dynamics even more by coupling to neighbor bubbles (compare, for instance, [187]). However, the influence of these factors on the phase shift would still need more exploration, which is beyond the scope of this work and left for the future.

An impression of the persistence of individual bubbles within the cluster in the tube is given in Fig. 4.22. Three frames with the time intervals of 40 μs in-between (which corresponds to about a full period $T = 38.9\,\mu$s) are shown in magnification, namely frames 28, 32 and 36 from the series in Fig. 4.18. From a rough impression, the cluster appears unchanged from frame 28 to frame 36, i.e. over the time of about $2T$. However, many bubbles change size and position, merge or split, and thus the detailed composition of the cluster is not stable. In an attempt to highlight such differences of the details, pixel-wise additive pictures have been constructed, where pixels of bubble positions (dark = low grey scale value) remain darker if a bubble is present in the second frame as well. Since the background has a higher grey level value, the addition leads to bright or saturated (white) colour if there is no bubble overlapping with the pixel in both frames. Identification of individual bubbles still persistent after one or two driving periods can be tried by eye in the indicated regions. In the violet region, this is partly possible, but in general, the impression is that bubble positions, oscillation states and also bubble numbers are perturbed from acoustic cycle to cycle due to the very close interaction, including merging and splitting, but also bubble dislocation during collapse "jumps" [172]. This finding is consistent with bubble behaviour in clusters in free liquid

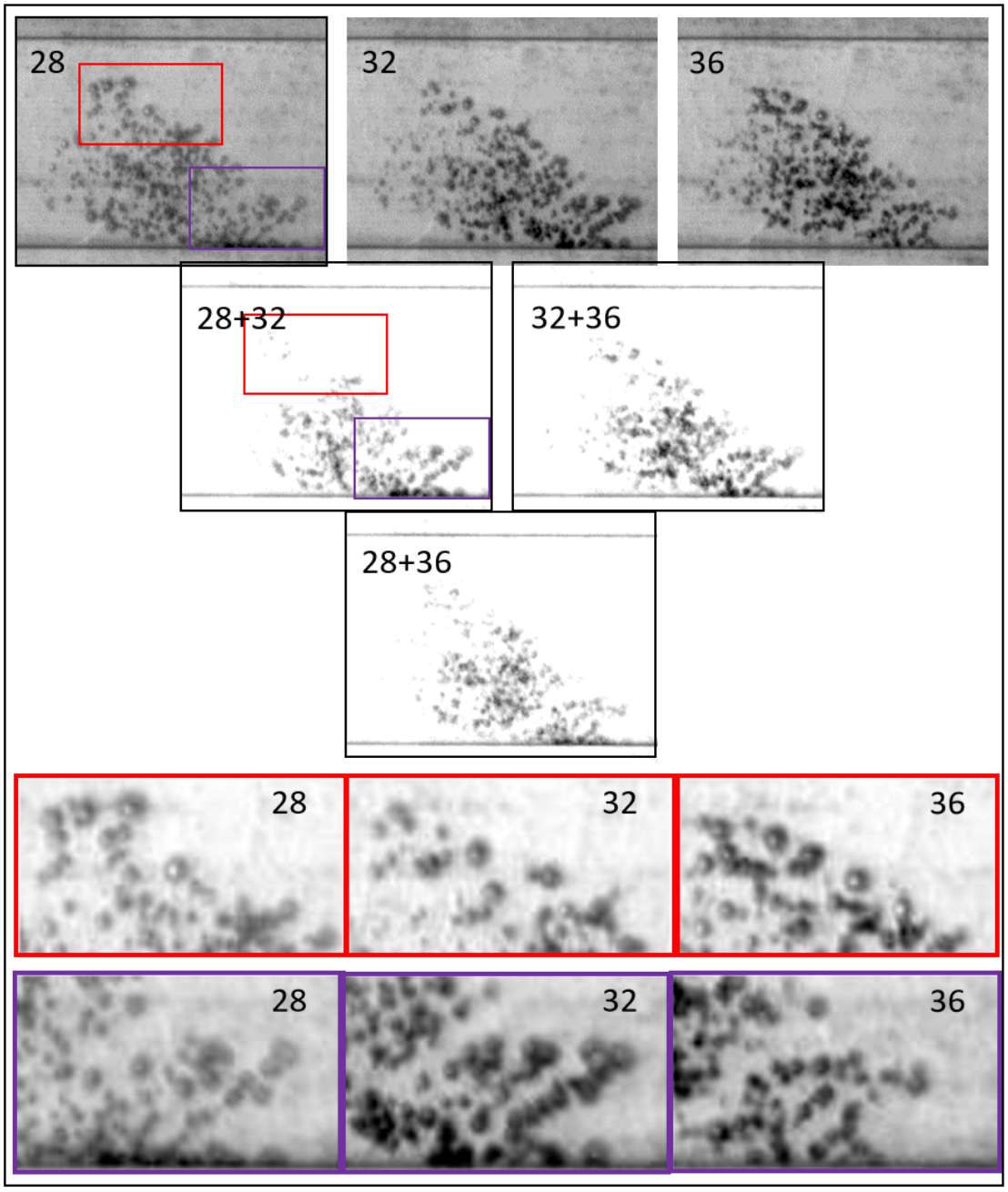

Figure 4.22. Three frames from Fig. 4.18 with nearly one driving period temporal distance (numbers 28, 32 and 36), top row. Inside bubbles in the cluster are in the expanded oscillation phase. The correlation between the images is analyzed by pixel-wise addition (with saturation) of the grey levels of two of the frames, respectively, shown in the middle rows. Dark regions correspond to bubbles at nearly the same positions in both frames. Thus the darker the cluster parts appear, the higher the one-to-one spatial correlation of individual bubbles in the cluster. The correlation is only moderate for a temporal distance of T (28+32 and 32+36), and it seems to decrease further for a temporal distance of $2T$ (28+36). The bottom rows show details in a region of lower correlation (red, brighter zone in the additive pictures) and higher correlation (violet, darker region in the additive pictures).

[188, 171].

To sum up, Fig. 4.17, 4.18 and 4.19 show that there is a phase shift between bubbles oscillating outside and inside channels, and the major reason might be the confinement of cavitation bubbles inside channels. Applied electrical amplitude, positioning of the channel in an ultrasonic bath, temperature and volume of dissolved gas in both liquids (in channel and bath), gas/liquid volume ratio in channels, slug lengths, density of bubble clusters inside channels and some resonance differences in slugs are some factors affecting the response of bubbles which in turn leads to differences in the phase shift between inside and outside bubbles.

4.2.2.5 Bubble structures inside flow tubes

The phase difference enables the visualization of internal bubbles without any disturbance from the coupling liquid, but it comes with the disadvantage of capturing a single time interval of bubble oscillation during one driving period. Bubble structures in channels are recorded by externally synchronizing the camera shutter and the sine wave delivered to the transducer with some constant phase shift to eliminate frames involving bubbles in the coupling liquid. Thus, the frame rate of the recordings presenting bubble structures in this section is referred to 25.7k fps (One frame per acoustic period).

Cavitation conditions are investigated with different function generator amplitudes within the slug flow of water and air. The transducer is driven at 25.7 kHz, and all recordings are obtained from the same channel which is at a fixed position in an ultrasonic bath. The flow rate of the water-air slug is approximately 10 μL/s, and the direction of the flow is from left to right. In silent conditions, the water-air slug length is kept constant where the length of the water slug is between 2.3-2.5 mm. However, lengths of the water slugs and the volume of air gaps show variation during sonication.

Bubble structures reported in this section are similar to the findings in Sec. 4.2.1.3. Electrical amplitude changes the cavitation density inside the channels, but bubble structures are usually in similar forms. In Fig. 4.23, cavitation bubbles in a flow channel and a two-phase boundary are given for driving amplitude of 300 mV. It is evident that although some are in different sizes, almost all bubbles are in a spherical shape. Wall-attached bubble clusters and dispersed bubble fields are typical bubble structures in channels. Both the upper and lower image in Fig. 4.23 show wall-attached clusters. These clusters usually are in roughly half spherical shape. Since the bubbles are close to each other, splitting and merging events are observed. The cluster has a more dense form where it sits on the channel wall. Hence bubbles are merged somewhere close to the wall and attracted to the channel surface. Smaller sized bubbles mostly surround larger bubbles attached to the wall. On the other hand, dispersed bubble structures have larger inter-bubble distances which result in less bubble-bubble interaction. From the first frame to the last frame, it is seen that dispersed bubbles are being attracted to the cluster attached to the surface of the channel. In the first frames, the average bubble size is about 0.031 μm. While bubbles move toward the cluster they interact with each other more and some merging events take place. The average bubble size increases to 0.042 μm and the number of relatively larger bubbles is also increased. It must be noted that since an external phase difference is applied to eliminate the outside bubbles, only the same single portion of the acoustic driving period can be observed. In lower image, bulge formation,

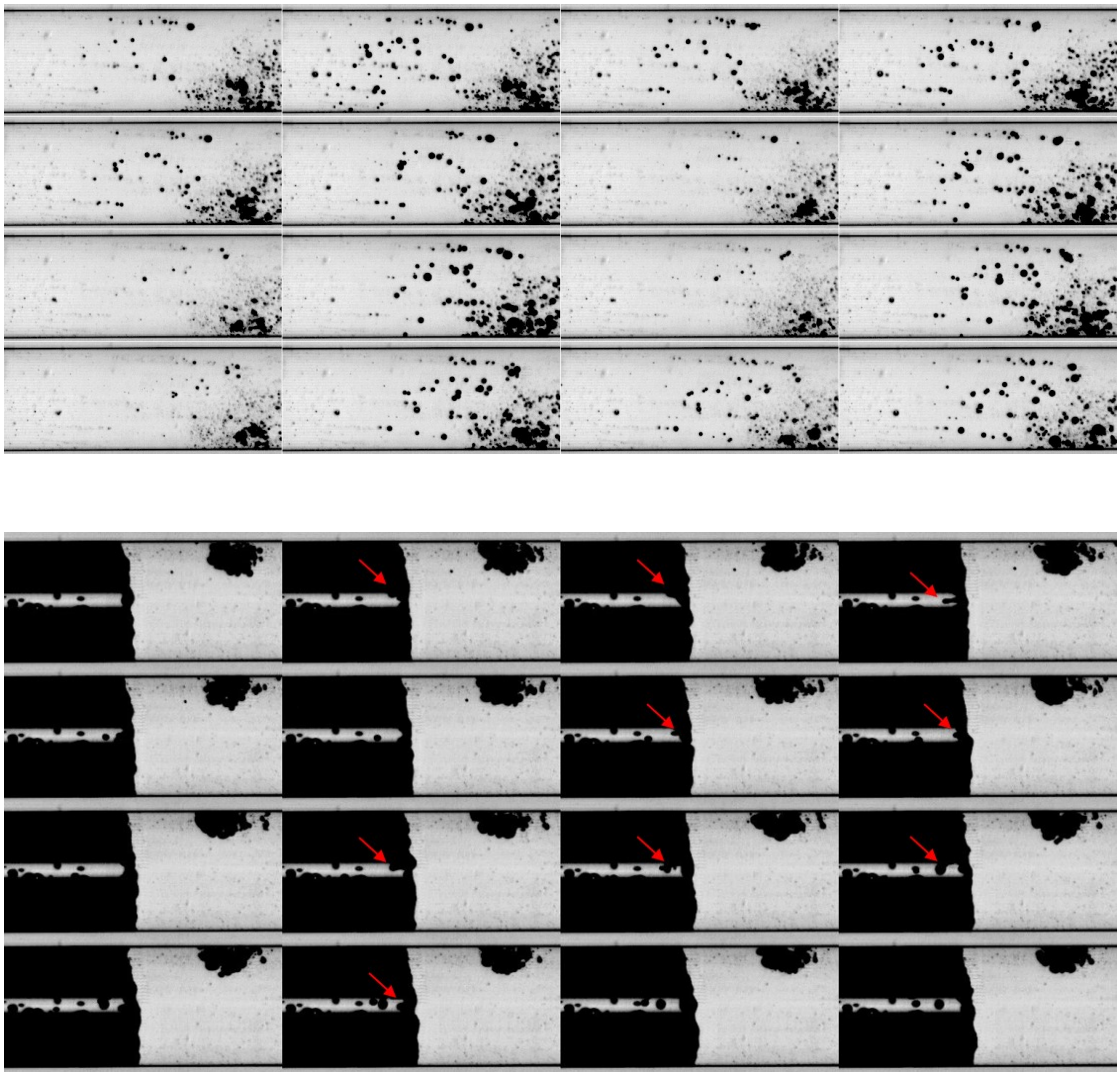

Figure 4.23. Top: Consecutive image series showing a wall-attached cluster aggregating at the bottom of the tube and less confined dispersed bubble structures in a water-air slug flow. **Bottom:** Droplet ejection at the water-air boundary and a wall-attached bubble cluster. [Channel diameter: 0.8 mm, water-air slug flow rate: approximately 10 μL/s (towards the right), transducer frequency: 25.7 kHz, electrical amplitude: 300 mV (corresponding to a delivered power of approximately 48 W), recording frame rate: 25.7k fps, exposure time: 1 μs.]

weak surface oscillations at the free interface and trajectories of ejected water droplets can be seen. Droplet ejection are correlated with bubble seeding (see Sec. 4.2.2.6). In this particular image series, another wall-attached bubble cluster is located next to the interface. As different than the upper cluster, it can be considered as a cluster of rather larger bubbles.

Fig. 4.24 represents consecutive frames of bubble structures (upper image) and droplet ejection at a two-phase boundary (lower image). A bubble cluster formed by similar-sized spherical bubbles is seen on the upper side channel. It is attracted and attached to the surface of the channel wall in the last frames. However, it is not certain that this cluster

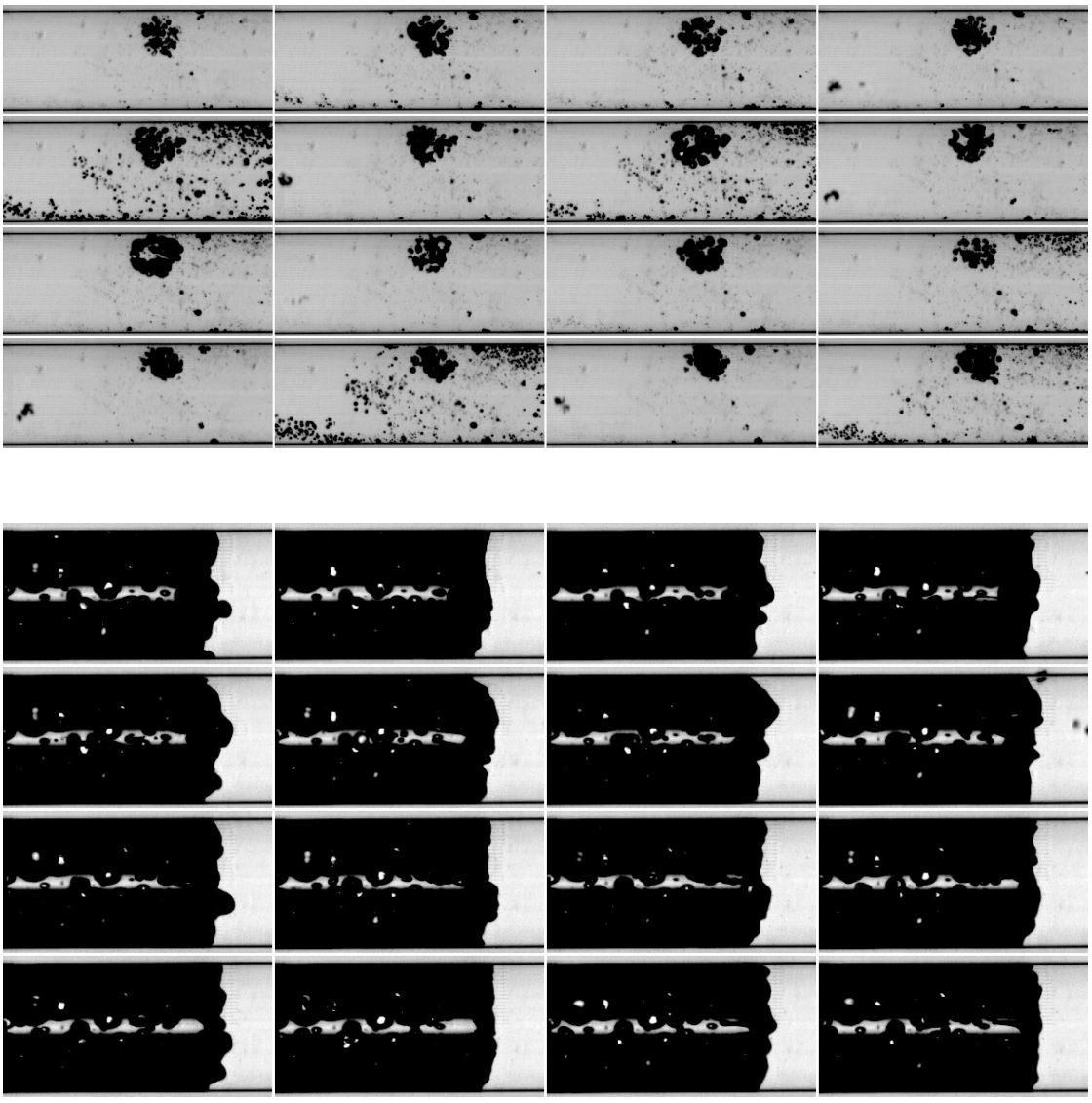

Figure 4.24. **Top:** Consecutive image series showing wall-attached bubble clusters of various sizes and streamers. **Bottom:** Bulge formation and droplet ejection at the water-air interface. Strong surface oscillations are observed at the free interface of the water-air boundary. A high number and volume of water droplets are ejected into the air gap. [Channel diameter: 0.8 mm, water-air slug flow rate: approximately 10 μL/s (towards the right), transducer frequency: 25.7 kHz, electrical amplitude: 400 mV (corresponding to a delivered power of approximately 75 W), recording frame rate: 25.7k fps, exposure time: 1 μs.]

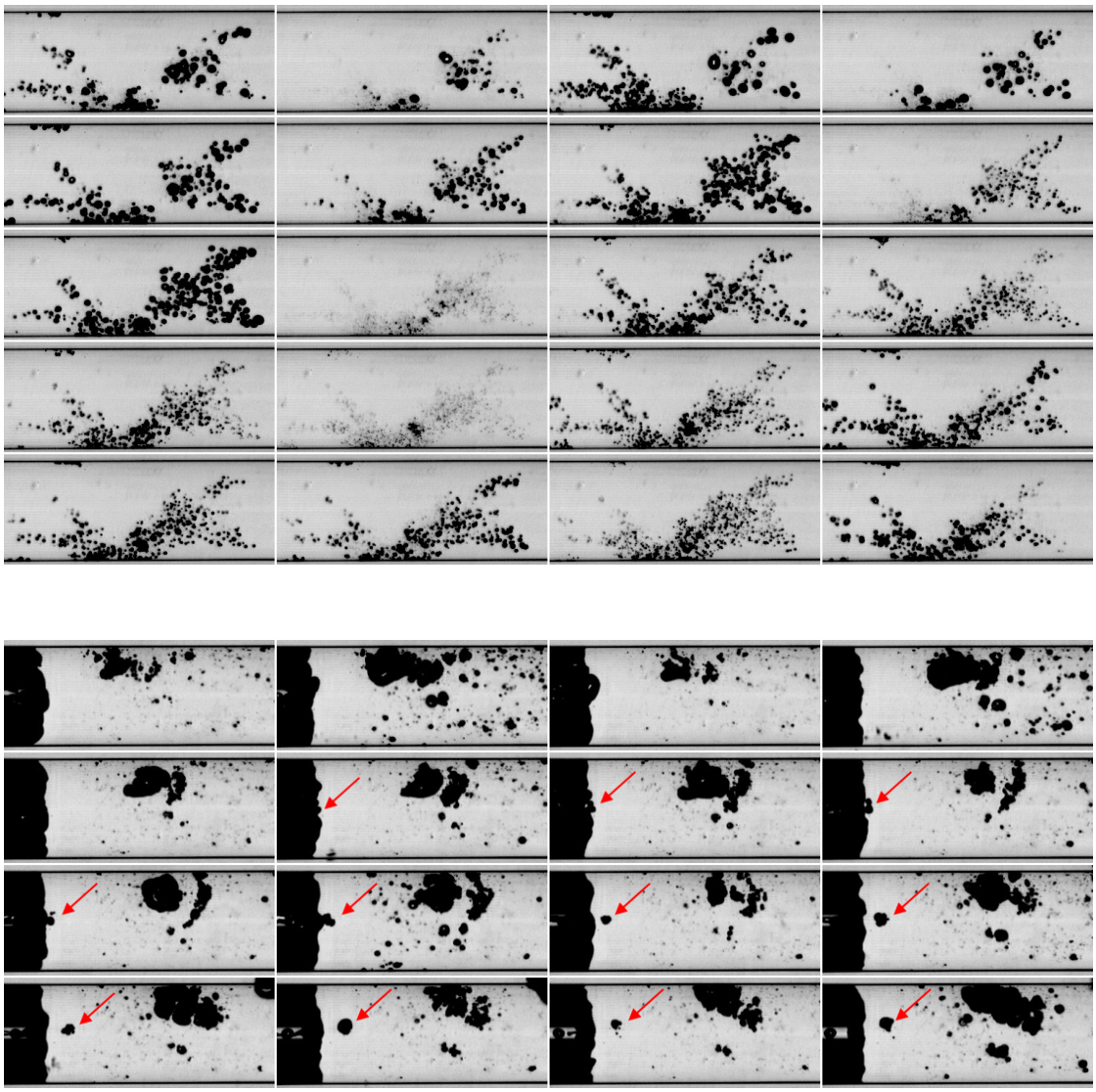

Figure 4.25. Top: Consecutive image series showing streamers that agglomerate at the channel wall. **Bottom:** Seeding of a large bubble from the water-air interface. Strong surface oscillations are observed at the free interface of the water-air boundary. The seeded large bubble moves towards the wall-attached bubble cluster. [Channel diameter: 0.8 mm, water-air slug flow rate: approximately 10 μL/s (towards the right), transducer frequency: 25.7 kHz, electrical amplitude: 500 mV (corresponding to a delivered power of approximately 93 W), recording frame rate: 25.7k fps, exposure time: 1 μs.]

is similar to wall-attached clusters observed in Fig. 4.23. Next to the cluster, there are also some smaller bubbles, they tend to sit on the wall and the ones being attracted to the wall merge. They are also surrounded by smaller bubbles. Although the density does not look the same, the structure is similar to the wall-attached cluster observed before in Fig. 4.23. The recording technique limits observing bubble oscillations in detail and gives only the same portion of the driving period. Regarding that, a bubble cluster is seen in different volumes which can hint to bubble collapse. One can say that bubbles collapse slightly harder with the increase in driving amplitude. Moreover, there are dispersed bubbles and streamers accompanying the cluster. At some frames, streamers have rather sharp longitudinal boundaries. One side of the sharp border can be nearly bubble free for some horizontal distances. This structure can be considered as a preliminary form of a "bubble plug" which is described before in Sec.4.2.1.3. The lower image in Fig. 4.24 shows the free interface between water and air. Boundary oscillations at this pressure amplitude are stronger than the ones obtained at a lower driving amplitude. Moreover, the number and volume of water droplets in air pockets are much higher. This might lead to more bubble centers and a higher bubble density in water slugs.

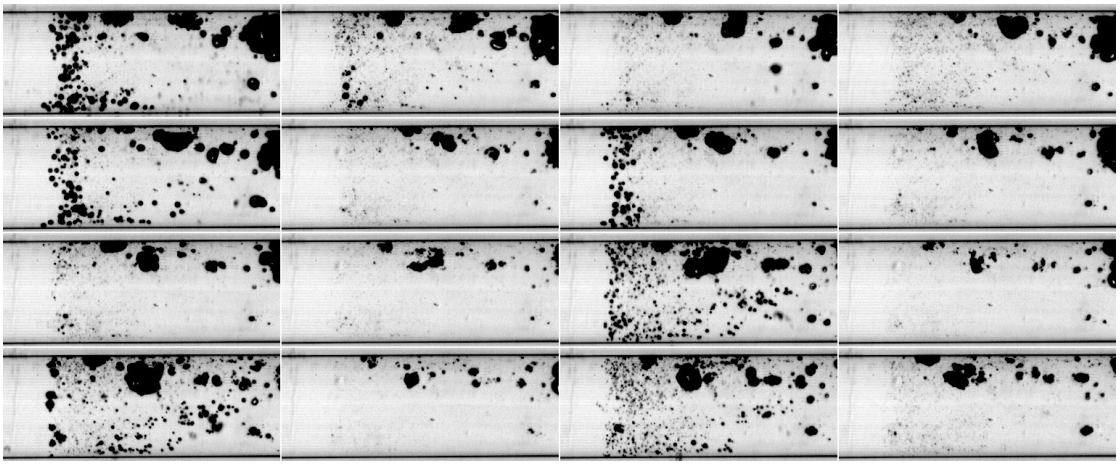

Figure 4.26. A bubble plug comprising of a roughly rectangular bubble field stretching from top to bottom. The first frame is the one at top left, and the sequential frames are followed row by row. One of the ends acts as a boundary between the bubble-free region and the bubble field. [Channel diameter: 0.8 mm, water-air slug flow rate: approximately 10 μL/s (towards the right), transducer frequency: 25.7 kHz, electrical amplitude: 400 mV (corresponding to a delivered power of approximately 93 W), recording frame rate: 25.7k fps, exposure time: 1 μs.]

The frames shown in Fig. 4.25 are recorded with the highest electrical amplitude (500 mV, delivered power is about 93 W). In the upper frame series, it is seen that clusters of spherical bubbles merge and agglomerate at some certain point on the tube wall. Bubbles can be attracted to that location due to the force acting on them in the acoustic field, or it may be a random event related to the tendency of bubbles to be attracted to surfaces. In the first frames, one can say that bubble clusters are first in different configurations. The cluster on the right side consists of more individual and spherical bubbles. On the other hand, the clusters which are already merged/ merging on the left side can be considered as streamers. It is not clear that the agglomeration and the attachment of bubble clusters on the wall are related to the wall-attached clusters. The lower frame

series present the bubble seeding at the free interface between the water slug and the air gap. A large bubble cluster can be seen close to a two-phase boundary with some dispersed bubbles around it. Unlike the wall-attached clusters, it has surface instabilities and it does not exhibit a spherical form. It undergoes some splitting and merging events, and it attaches to the channel wall. The free interface has also strong oscillations and it leads to the shooting of water droplets into the air gap. At the same time, a surface bulge is detached and turned into an injection of a large bubble into a water slug. Another common bubble structure is the "bubble plug." The bubble structures depicted in Fig. 4.23 can be considered as an early stage of the bubble plug formation. As the sound pressure amplitude increases, more bubble centers are generated, resulting in clearer bubble plugs. A sequence showing a bubble plug is presented in Fig. 4.26. It is observed that a bubble field, consisting of bubbles and clusters of different sizes, has a distinct boundary on the left side. This boundary separates the bubble-free region from the field of cavitation bubbles. One can associate this structure with the acoustic resonance effect in channels [176]. However, the bubble plugs are not stationary and do not remain fixed in the same positions within the channels; instead, they move within the liquid slug. The size and shape of the bubbles forming the sharp border are very similar, and they are different from the other cavitation bubble structures inside. The difference is very noticeable for some frames where the bubbles located at the border appear as an attached slice (*e.g.* 5^{th} and 7^{th} frame). Thus, it can be considered that the bubbles stretching between the bottom and top wall of the channel and forming the border are a bubble cluster of their own. This border is possibly a streamer formed by sources attached to the top and bottom wall. In some frames, the bubble density is higher next to the walls, which makes the border cluster look wider at the top and bottom of the channel. On the other hand, the number of bubbles decreases around the middle of the border, which leads the center of the cluster to be narrower. However, it is not very clear whether wall-attached bubble clusters are related to this structure. The streamers agglomerating at the same point on the channel wall shown in Fig. 4.25 might also be linked to the sharp border structure. The bubbles might be like a river from one wall source to another and form the sharp boundary. Moreover, the bubble plug consists of some bubble clusters and a dispersed bubble field. Small individual bubbles are mostly in a spherical shape, while larger bubbles and bubble clusters oscillate with strong volume changes and undergo surface instabilities. For lower sound pressure amplitudes, the bubble plugs mostly consist of dispersed bubbles, resulting in a large inter-bubble distance and smaller bubble clusters, if any.

4.2.2.6 Bubble nucleation and two phase boundary

Cavitation bubble structures inside the PFA tube originate from the events taking place at the interface between liquid and air slugs since no cavitation is detected without gas pockets inside the tube. An example of a nucleation event of bubble entrainment from a gas pocket into a liquid slug is given in Fig. 4.27. The boundary layer forms indentations and bulges, probably in connection to acoustically driven capillary waves [10]. Once seeding takes place, a formed single bubble travels away from the interface, which multiplies the bubble number by splitting events, and translates into a cluster. The wavelength $\lambda_c \approx \sqrt[3]{\frac{2\pi\sigma}{\rho {f_c}^2}}$ can be calculated as $\lambda \approx 135\mu$m, with the parameters

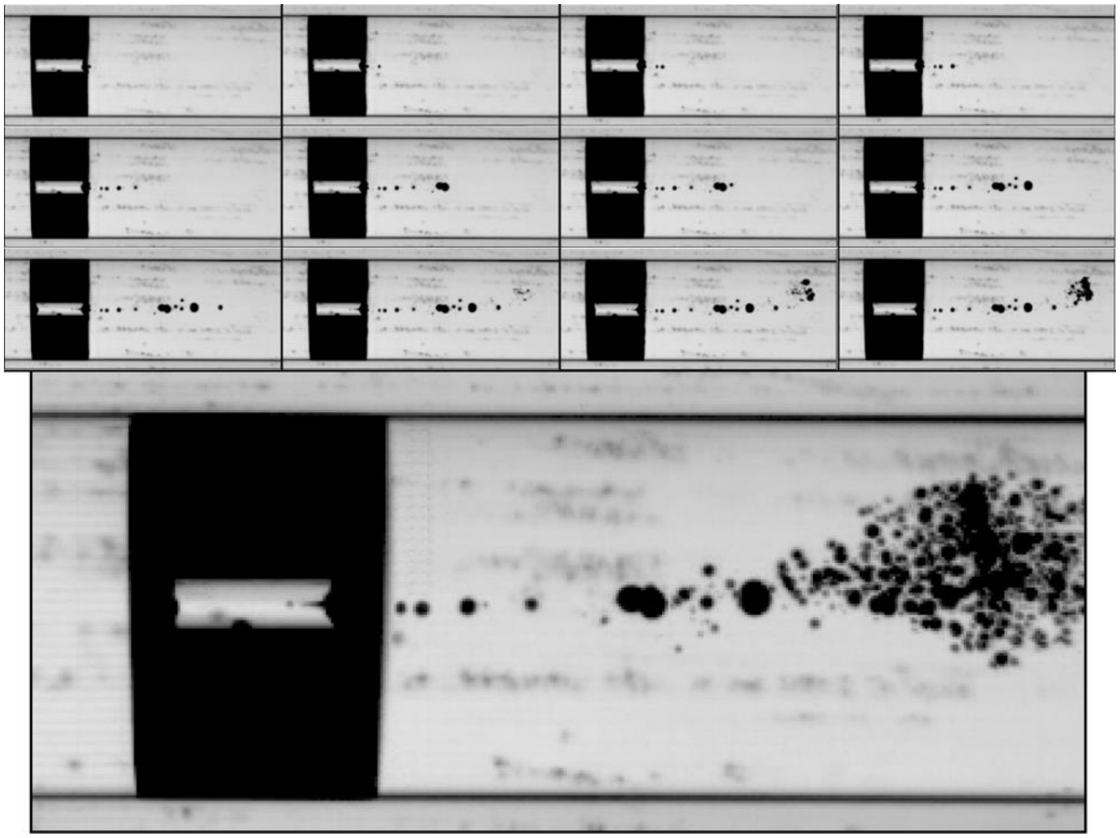

Figure 4.27. Bubble nucleation at the free interface of a liquid-air slug. The upper images depict a bubble entering the liquid slug and multiplying itself frame by frame. The lower image shows the bubble cluster formed at a later stage. The frames were recorded at 25.7k fps, with an exposure time of 1 μs, and a frame height of 1 μs.

for water, and a Faraday capillary wave frequency being half of the driving frequency $f_c = f/2$. In Fig. 4.27, the bulge formed in the middle of the interface has a width of approximately 85 μm, which is somewhat larger than the calculated $\lambda_c/2 \approx 67.5\,\mu$m. The spherical boundary conditions might affect the free surface inside the tube, which gives rise to different surface oscillation modes of wavelength other than that of an infinite interface. The formation of the bulge positioned at the very center of the tube axis also indicates a symmetric mode oscillation of the interface. The same capillary waves at the free interface also leads to water droplets being ejected into the gas pocket. In Fig. 4.28, the evolution of the liquid jet at the center of the two-phase boundary turning into water droplets in the gas slug is shown. The formed water droplet has a volume of around 5.7 pl (droplet radius is $\sim$ 11 μm) and speeds up to 9 m/s. There is also a subsequent train of droplets following it with a velocity of approximately 3 m/s into the gas volume. Liquid drops can move freely, collide, agglomerate, or hit the tube walls, or the subsequent liquid slug interface. The mechanism of droplet ejection from the capillary wave peak observed here is very similar to the ultrasonic atomization at open liquid surfaces [189]. Due to the mass transfer via droplet ejection and bubble seeding, slug lengths and as well as the liquid-air slug ratio changes by longer ultrasonic irradiation time.

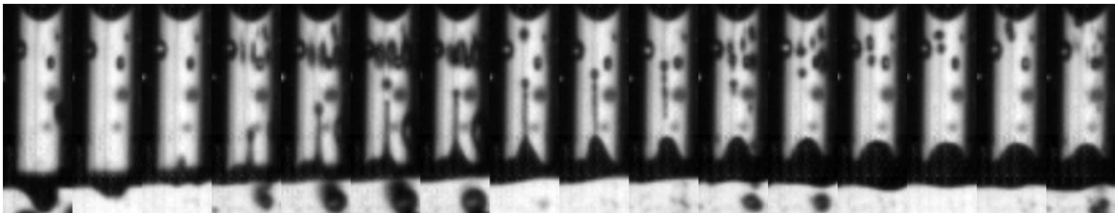

Figure 4.28. Droplet ejection occurs at the center of the free interface of a liquid-air slug. Frames are presented by rotating the images 90 degrees clockwise compared to Fig. 4.27; in this representation, water is located at the bottom, and the air is at the top. The recording was done at 150k fps, with a frame width of about 200 μm, and an exposure time of 2 μs. A bulge forms from a peak of a capillary wave, which then disintegrates into the gas slug as a droplet. After the third frame, a newly formed bubble, appearing as a dark spot in the liquid at the bottom, oscillates under the influence of ultrasonic irradiation.

Fig.4.28 represents a case of droplet ejection accompanied by bubble seeding or creation, although this is not always the case. However, there is still a connection between bubble nucleation and droplet ejection in some cavitation events. Experimentally, it is challenging to track fresh bubbles entering the liquid and liquid droplets being ejected towards the gas pocket, and establish the connection between these two events due to cavitation in the coupling liquid. Figure 4.29 illustrates four columns, each corresponding to a series of images at different times of sonication. The recording is conducted at a frame rate of 100k fps with an exposure time of 1 μs resulting in 10 μs between the frames of each column. The width of the images in the first three columns is approximately 0.85 mm, while the images in the fourth column are 2.42 mm wide, whereas the channel diameter is 0.8 mm. In each image, the bright areas represent the water slug, while the black regions represent gas pockets in the channels. Prior to sonication, no air gaps in the liquid or water droplets in the gas pockets are observed. The total duration of sonication is 0.4055 s. It should be noted that a complete slug of liquid and air pocket cannot be observed due to the limited frame length (approximately 3.21 mm). Therefore, the lengths of the air and liquid slugs, as well as the events occurring within those slugs, are unknown. As sonication commences (function generator amplitude of 400 mV, the difference between delivered and reflected power is around 60 W), water droplets begin to be ejected from the boundary.

The first droplet ejection occurs around the middle of the boundary approximately 0.00051 s after the start of sonication, as shown in the first column of Figure 4.29. No other water droplets besides the freshly created one are observed in the air gap, and no cavitation bubble is observed in the channels. The bubbles seen as cavitating in the images are not inside the channels but in the coupling liquid surrounding the channel. The second column of frames shows the condition inside the channel approximately 0.00681 s after the start of sonication. In the middle of the boundary, a trace of a jetting liquid droplet can be observed. As the droplets are free to move in the air gaps, this particular droplet follows a curved upward trajectory. There are also other water droplets in the air gap that exhibit surface oscillations due to ultrasound. Among them, eight droplets can be reasonably distinguished and counted. The largest droplet has a diameter of about 0.12 mm, while the others have approximately 0.08 mm, and the smallest ones have around 0.03 mm. These larger droplets result from the agglomeration

or clustering of ejected water droplets. The positioning of the water droplets in the first frame of the column differs from that in the last frame, indicating that they are also moving and changing location as ultrasound is applied. It is also observed in these images that the cavitating bubbles outside the channel obstruct a clear view from inside the channel. Although there is cavitation inside the channel, it is not possible to observe the nucleation event initiating cavitation.

The third column represents the frames recorded 0.21014 s after the start of sonication. It is observed that the boundary layer forms a clear indentation and bulges, probably in connection to acoustically driven capillary waves [10]. Liquid droplet ejection continues to take place. There is a large bulk water droplet attached to the wall, resulting from the agglomeration of water droplets ejected from the boundary. The diameter of the droplet is roughly 0.32 mm. There is a time interval of about 0.20333 s between the second and third column of frames. During this time, water droplets somewhat merge to form a bulk droplet, and the total volume of droplets in the second column increases by about 32 times. It should be noted that the frames provide a limited length of the liquid slug, so the number of droplets might be greater than observed. However, it is evident that more water droplets are ejected as sonication continues and they move through the air gap. Moreover, since the frame length is limited, it is not clear whether the accumulated water volume in the air pocket solely comes from the observed liquid slug. Neighboring liquid slugs likely also contribute to the water content in the air gap. Therefore, comparing the volume of water content and void fraction could be misleading. However, it is clear that cavitation bubble clusters grow, and the volume of water droplets in the air gap increases with sonication. The frames obtained 0.34171 s after the start of sonication are shown in the last column. In these frames, the bulk water droplet becomes even larger, with a diameter of about 0.51 mm, which is very close to the diameter of the channel itself. Additionally, these frames clearly show that bubbles cavitating in the coupling liquid block the view inside the channels. There are two cavitation bubble clusters attached to the upper and lower walls of the channels (first and last frames). It is not possible to analyze the relationship between these two clusters, but one can claim that particularly the top one has a connection to the boundary. It is attached to the wall from one end, but the other end has a tail that extends towards the middle of the boundary between air and water. The boundary layer is linked to the droplet ejection due to capillary waves, which can contribute to bubble seeding. It is not possible to track each liquid jet and correlate it with bubble seeding events due to cavitation in the coupling liquid, but the clusters attached to the wall might be growing over time with the seeded bubbles from the boundary.

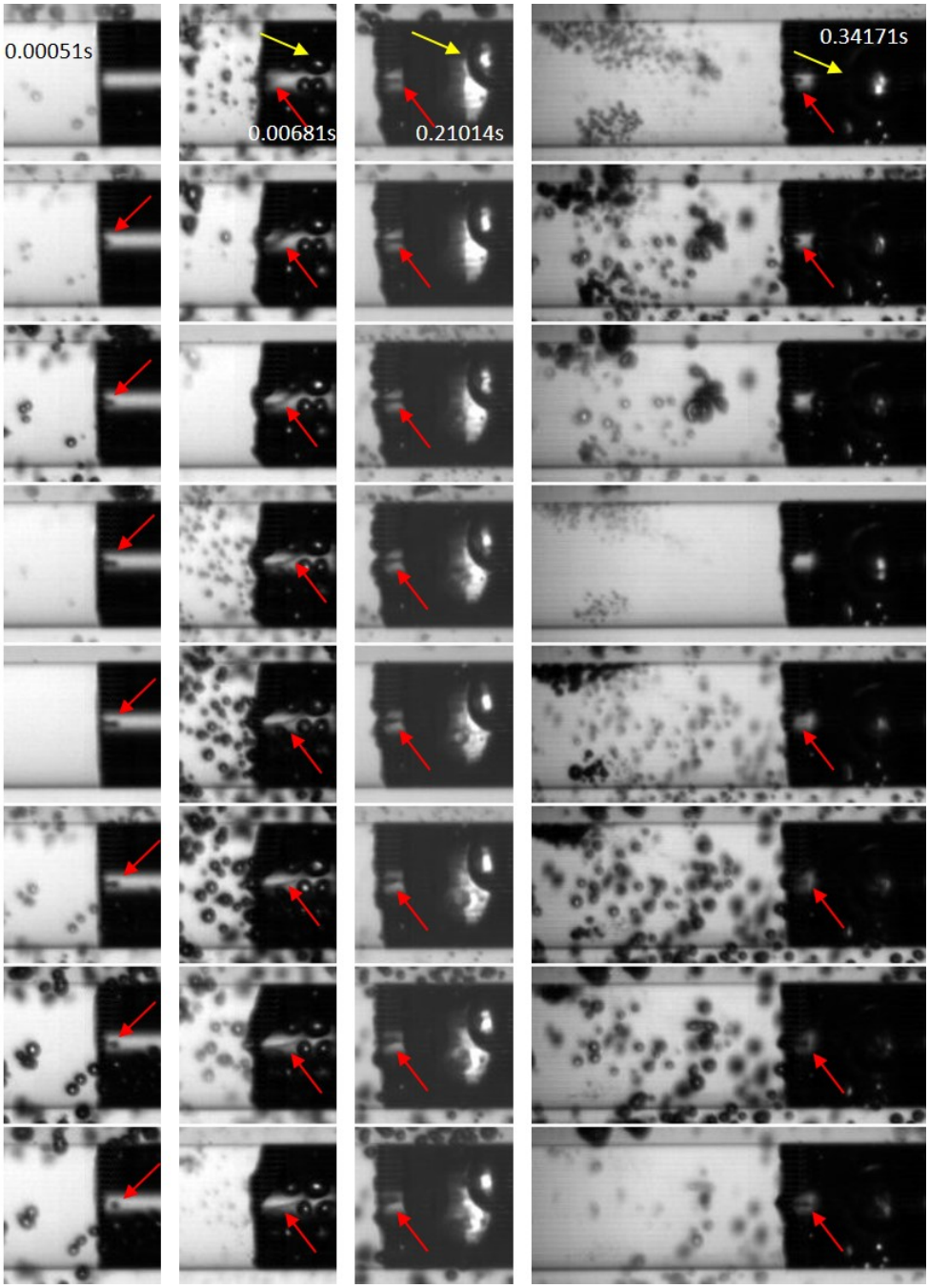

Figure 4.29. Droplet ejection events occur at the free interface of a water-air slug. The ejection of water droplets is pointed out via red arrows and yellow arrows show water droplets. Each column represents consecutive frames from a recording performed at 100k fps, with exposure time of 1 μs. The tube diameter is 0.8 mm. The channels are filled with water-air slugs, and then the flow is stopped. The sonication is performed at 25.7 kHz with an applied electrical power of approximately 60 W (the difference between delivered and reflected power). In each frame, the liquid is on the left (white) and the air gap is on the right side (black). The total time of sonication is 0.4055 s. From left to right, the columns depict the consecutive frames extracted from the recording 0.00051, 0.00681, 0.21014, and 0.34171 s after the start of sonication, respectively.

Chapter 5

Conclusion

The overall aim of this research was to investigate the relationship between physical and chemical effects in small, sonicated flow channels and contribute to the better understanding of the working principles of milli-flow-reactors that work with ultrasound. Among a certain variety of reactor and channel geometries, finally a "tube-in-bath" setup was chosen as a generic platform that is easy to install, but also represents many general aspects of such systems in an accessible manner. Based on ample experience within the sonochemistry community with bath batch reactors, the immersion of a flow channel into such a bath is straightforward and relatively cheap. This geometry further suggests a "simple" transfer of cavitation activity from larger bath volumes into the confined flow channels. The present study, however, has shown that this transfer is not trivially given, and that several aspects have to be taken into account for a successfully working sonicated flow channel in submerged geometry.

In a first design, the flow channels had been arranged between an aluminum plate and a polycarbonate top, and they were subjected to ultrasound by direct contact with a Langevin transducer, without the presence of a liquid medium. While similar geometries are frequently found for test setups in other studies, here it turned out not to be suitable, and has been discarded. Reasons were the low effectivity in creating cavitation, difficult imaging of bubbles due to the non-transparent bottom, and finally material failure. Channel connections from tubes to the channels could not be sealed reliably, and furthermore, overheating and melting of plastics material occurred – apparently an effect from "hot spots" of the sound field directly at the transducer plate. Nevertheless, as an outcome from these experiments, a decreasing nucleation threshold and higher cavitation activity in the channels for increasing acoustic driving frequency could be confirmed. In the second type of geometry, a water-filled bath was used as a coupling medium. The flow channels in form of PFA tubings were submerged into the bath which was sonicated via bottom-mounted Langevin transducers. Although cavitation in the coupling liquid (water) could not be fully suppressed, a quite reasonable transfer of acoustic energy into the tubes could be achieved, i.e., intense and chemically active cavitation has been generated inside the flow channels. An initial trial design with several submerged loops of the tube has been improved by a meandering arrangement fixed by a frame holder. This could increase the submerged tube length and also led the flow through a larger volume of the bath. In particular, the tube was now passing all the region above one transducer, sampling high and low pressure regions of the standing wave in the bath.

For initiation of cavitation within the tube, it was found necessary to feed gas additionally to the liquid flow, which then formed a Taylor flow of alternating gas and liquid slugs. Nucleation of cavitation bubbles has been identified to take place via gas entrainment from the gas-liquid boundary that developed intense capillary waves during sonication. Next to bubble formation on the liquid side of the boundary, drops were ejected into the gas slugs. This liquid transfer or "spraying" by "internal atomization" had been observed before in the context of wetting of blind holes in cavitating liquids [190], and in a quite intriguing resonant fashion in miniature Taylor flows sonicated at higher frequencies [176]: there, intense spraying is observed if the liquid slug length fits to an integer multiple of half the acoustic wavelength (longitudinal resonance). In the present experiments, however, the acoustic wavelength (about 5.7 cm at 25.7 kHz) is somehow larger than the liquid slug length (about 1 cm), and direct resonances along the slug are not likely here. However, since the slug length proportions are observed to show a certain variation during the running experiment (apparently caused by the drop ejection and an according fill-up of the gas slugs), resonant conditions can neither be ruled out.

Once nucleated, the cavitation inside the tube develops various features, including streamer figures, dense bubble clusters, and peculiar "walls" that separate highly bubble populated parts of the liquid from apparently non-cavitating zones. Several examples of structures have been discussed in the present work, and many details remain to be evaluated. Among the results obtained, it could be shown that the bubbles in the tubes tend to oscillate in phase shift to the external cavitation bubbles in the coupling liquid next to the tubes. This allowed to image bubbles structure evolution in the channels without optical disturbance from outer bubbles. The phase shift cannot be fully explained yet, but potentially the bubble dynamics in the tubes is influenced by the tube wall that acts as a restriction for the liquid volume displacement during the bubble oscillations. From a modified radial bubble oscillation model after Zudin [57], in comparison to a bubble in free liquid, it follows that the bubble expansion can start earlier, and at the same time the maximum bubble expansion is reduced. However, further factors might differ inside and outside the tube and influence the bubble dynamics, for instance the effective sound pressure (slightly damped by the tube walls), the bubble equilibrium sizes, interaction of the interior bubbles within a dense cluster, or close interaction with the tube walls.

Although the bubble dynamics is somehow altered inside the channels as compared to the outside, the inside bubbles are well chemically active. This has been demonstrated by sono-chemiluminescence (luminol) measurements. As a peculiar and interesting fact, the spatial distribution of luminol emission patterns in the bulk liquid and in the tube can differ: While in the bulk liquid, the highest pressure zones (antinodes) in the standing wave are de-populated from bubbles for increased driving power (due to Bjerknes force inversion), this effect cannot happen for the confined bubbles within the tubes (since bubbles cannot "escape" the tubes). At least for horizontal arrangement of the tubes (perpendicular to the emitted wave front from the transducer), maximum luminol emission seems to agree with maximum pressure amplitude, while in the bulk liquid, high pressure zones at the antinodes and right in front of the transducer do not emit much SCL light. This suggests that the sound field might be exploited with higher efficiency via cavitation in confined geometry (channels), as compared to a batch reactor.

The studies presented can only be seen as a first step towards a full understanding and

optimization of small sonicated flow channels. Many parameters come into play, and apart from the physics of cavitation, several aspects occur with respect to a real application in chemical processing. In the present geometry of submerged sub-millimeter diameter tubes, different flow paths could be probed, for instance vertical channels (parallel to the emitted wave from the bottom transducer). Preliminary test have shown that the behavior in vertical tubes differs somehow with respect to cavitation activity and bubble structures, since the vertical confinement is different (now by the phase boundary of the Taylor flow, not by the tube wall), but details have to be explored in the future. Further extensions of the current design concern multiple tube stacks next to each other, either in series (longer residence time) or in parallel (higher throughput). The limits of energy transfer in relation to channel density should be explored, since the introduction of the gas phase by the Taylor flow, and also the multiple tube walls, might shield the acoustic field at some level and reduce the effective volume treated. Further, the influence of the flow speed is a nearly unexplored region yet, since only slow flows have been used. For much higher flow velocities, residence times go down, but also laminarity might be changed an Taylor flow conditions overcome – which might be beneficial or not. Preliminary results show further interesting effects regarding the flow if cavitation sets in. Additionally, the effect of dissolved gas (type and concentration) has not been explored yet, apart from the well-know positive effect of argon on luminescence brightness. Considering an expansion of potential parameter changes, one could change the driving frequency (potentially enter more easily resonant slug conditions at higher frequencies), change the tube diameter or material (potentially changing nucleation conditions due to larger/smaller liquid volumes and/or wetting properties of the walls), or change the outer (coupling liquid container) geometries. For instance, one might consider focused transducers, with the flow in the focal region to increase local pressure amplitudes (and potentially facilitate nucleation).

Finally, an overall assessment of efficacy in terms of energetic balance, processing throughput, material cost, operation life times, as well as comparison to competing processing methods, would be needed as a further step towards real application of small sonicated flow channels in process intensification. Future demands of effective processes will continue stimulating further studies in these directions.

Bibliography

[1] C. Rawshaw, "Process intensification: a game for n players," *Chemical Engineering*, vol. 416, 1985.

[2] A. I. Stankiewic and J. A. Moulijn, "Process intensification: transforming chemical engineering," *Chemical Engineering Progress*, vol. 96, no. 1, pp. 22–34, 2000. ISSN: 0360-7275.

[3] T. Van Gerven and A. Stankiewicz, "Structure, energy, synergy, time—the fundamentals of process intensification," *Industrial & Engineering Chemistry Research*, vol. 48, no. 5, pp. 2465–2474, 2009.

[4] D. Fernandez Rivas and S. Kuhn, "Synergy of microfluidics and ultrasound," *Topics in Current Chemistry*, vol. 374, no. 5, 2016.

[5] D. Fernandez Rivas, P. Cintas, and H. J. G. E. Gardeniers, "Merging microfluidics and sonochemistry: towards greener and more efficient micro-sono-reactors," *Chem. Commun.*, vol. 48, pp. 10935–10947, 2012.

[6] Z. Dong, Z. Wen, F. Zhao, S. Kuhn, and T. Noël, "Scale-up of micro- and milli-reactors: An overview of strategies, design principles and applications," *Chemical Engineering Science: X*, vol. 10, p. 100097, 2021.

[7] S. Kuhn, T. Noël, L. Gu, P. L. Heider, and K. F. Jensen, "A teflon microreactor with integrated piezoelectric actuator to handle solid forming reactions," *Lab on a chip*, vol. 11, p. 2488—2492, August 2011.

[8] V. Hessel, "Novel process windows – gate to maximizing process intensification via flow chemistry," *Chemical Engineering & Technology*, vol. 32, no. 11, pp. 1655–1681, 2009.

[9] K. S. F. Lew, E. Klaseboer, and B. C. Khoo, "A collapsing bubble-induced micropump: An experimental study," *Sensors and Actuators A: Physical*, vol. 133, no. 1, pp. 161–172, 2007.

[10] Tandiono, S.-W. Ohl, D. S.-W. Ow, E. Klaseboer, V. V. T. Wong, A. Camattari, and C.-D. Ohl, "Creation of cavitation activity in a microfluidic device through acoustically driven capillary waves," *Lab Chip*, vol. 10, pp. 1848–1855, 2010.

[11] O. S. W. Tandiono, D. S. Ow, E. Klaseboer, V. V. Wong, R. Dumke, and C. D. Ohl, "Sonochemistry and sonoluminescence in microfluidics," *Proc Natl Acad Sci*, vol. 108, no. 15, pp. 5996–8, 2011.

[12] S.-W. Ohl and C.-D. Ohl, "Acoustic cavitation in a microchannel," in *Handbook of Ultrasonics and Sonochemistry* (M. Ashokkumar, ed.), pp. 1–37, Singapore: Springer Singapore, 2016.

[13] J. J. John, S. Kuhn, L. Braeken, and T. Van Gerven, "Ultrasound assisted liquid–liquid extraction in microchannels—a direct contact method," *Chemical Engineering and Processing: Process Intensification*, vol. 102, pp. 37–46, 2016.

[14] Z. Dong, C. Yao, X. Zhang, J. Xu, G. Chen, Y. Zhao, and Q. Yuan, "A high-power ultrasonic microreactor and its application in gas-liquid mass transfer intensification," *Lab on a chip*, vol. 15, p. 1145—1152, February 2015.

[15] C. Delacour, C. Lutz, and S. Kuhn, "Pulsed ultrasound for temperature control and clogging prevention in micro-reactors," *Ultrasonics Sonochemistry*, vol. 55, pp. 67–74, 2019.

[16] R. Jamshidi, D. Rossi, N. Saffari, A. Gavriilidis, and L. Mazzei, "Investigation of the effect of ultrasound parameters on continuous sonocrystallization in a millifluidic device," *Crystal Growth & Design*, vol. 16, no. 8, pp. 4607–4619, 2016.

[17] H. Chen, J. Li, W. Zhou, E. G. Pelan, S. D. Stoyanov, L. N. Arnaudov, and H. A. Stone, "Sonication–microfluidics for fabrication of nanoparticle-stabilized microbubbles," *Langmuir*, vol. 30, no. 15, pp. 4262–4266, 2014.

[18] G. Valitov, R. Jamshidi, D. Rossi, A. Gavriilidis, and L. Mazzei, "Effect of acoustic streaming on continuous flow sonocrystallization in millifluidic channels," *Chemical Engineering Journal*, vol. 379, p. 122221, 2020.

[19] Q. Tseng, A. M. Lomonosov, E. E. M. Furlong, and C. A. Merten, "Fragmentation of DNA in a sub-microliter microfluidic sonication device," *Lab Chip*, vol. 12, pp. 4677–4682, 2012.

[20] C. E. Brennen, "A review of the dynamics of cavitating pumps," *IOP Conference Series: Earth and Environmental Science*, vol. 15, p. 012001, nov 2012.

[21] T. van Terwisga, E. van Wijngaarden, J. Bosschers, and G. Kuiper, "Achievements and challenges in cavitation research on ship propellers," *International Shipbuilding Progress*, vol. 54, no. 2-3, pp. 165–187, 2007.

[22] K. Kim, K. Hwang, K. Lee, and K. Lee, "Investigation of coolant flow distribution and the effects of cavitation on water pump performance in an automotive cooling system," *International Journal of Energy Research*, vol. 33, no. 3, pp. 224–234, 2009.

[23] T. J. Mason, "Ultrasonic cleaning: An historical perspective," *Ultrasonics Sonochemistry*, vol. 29, pp. 519–523, 2016.

[24] J. J. Hinman and K. S. Suslick, "Nanostructured materials synthesis using ultrasound," *Topics in Current Chemistry*, vol. 375, no. 1, p. 12, 2017.

[25] G. Mancuso, M. Langone, and G. Andreottola, "A critical review of the current technologies in wastewater treatment plants by using hydrodynamic cavitation process: principles and applications," *Journal of Environmental Health Science and Engineering*, vol. 18, no. 1, pp. 311–333, 2020.

[26] C. E. Brennen, "Cavitation in medicine," *Interface focus*, vol. 5, pp. 20150022–20150022, 10 2015.

[27] L. Rayleigh, "Viii. on the pressure developed in a liquid during the collapse of a spherical cavity," *The London, Edinburgh, and Dublin Philosophical Magazine and Journal of Science*, vol. 34, no. 200, pp. 94–98, 1917.

[28] S. Putterman, "Sonoluminescence: Sound into light," *Scientific American*, vol. 272, no. 2, pp. 33–37, 1995.

[29] C. D. Gibb, "Stanley Smith Cook 1875-1952," *Obituary Notices of Fellows of the Royal Society*, vol. 8, pp. 118–127, 01 November 1952.

[30] R.W.Wood and A. L. Loomis, "XXXVIII. The physical and biological effects of high-frequency sound-waves of great intensity," *The London, Edinburgh, and Dublin Philosophical Magazine and Journal of Science*, vol. 4, no. 22, pp. 417–436, 1927.

[31] K. Yasui, *Acoustic Cavitation and Bubble Dynamics, Briefs in Molecular Science*, ch. Acoustic Cavitation. Li, S.C., Ed.; London: Springer, Cham, 2018.

[32] C. E. Brennen, *Cavitation and Bubble Dynamics*. New York: Oxford University Press, 1995.

[33] A. J. Acosta, *Cavitation of Hydraulic Machinery*, ch. Cavitation and cavitation types, pp. 9–46. Li, S.C., Ed.; London: Imperial College Press, 2000.

[34] Z. Izadifar, P. Babyn, and D. Chapman, "Ultrasound cavitation/microbubble detection and medical applications," *Journal of Medical and Biological Engineering*, vol. 39, no. 3, pp. 259–276, 2019.

[35] M. Ashokkumar, *Ultrasonic Synthesis of Functional Materials*, ch. Ultrasonic Synthesis of Functional Materials. Springer International Publishing, 2016.

[36] E. Neppiras, "Acoustic cavitation," *Physics Reports*, vol. 61, no. 3, pp. 159–251, 1980.

[37] L. D. Landau and E. M. Lifshitz, *Course of Theoretical Physics*. Pergamon Press, 1987.

[38] M. Minnaert, "XVI. On musical air-bubbles and the sounds of running water," *The London, Edinburgh, and Dublin Philosophical Magazine and Journal of Science*, vol. 16, no. 104, pp. 235–248, 1933.

[39] W. Lauterborn and T. Kurz, "Physics of bubble oscillations," *Reports on Progress in Physics*, vol. 73, p. 106501, sep 2010.

[40] U. Parlitz, V. Englisch, C. Scheffczyk, and W. Lauterborn, "Bifurcation structure of bubble oscillators," *The Journal of the Acoustical Society of America*, vol. 88, no. 2, pp. 1061–1077, 1990.

[41] G. K. Batchelor, *An Introduction to Fluid Dynamics*. Cambridge Mathematical Library, Cambridge University Press, 2000.

[42] M. P. Brenner, S. Hilgenfeldt, and D. Lohse, "Single-bubble sonoluminescence," *Reviews of Modern Physics*, vol. 74, p. 425–484, may 2002.

[43] A. Prosperetti, "Thermal effects and damping mechanisms in the forced radial oscillations of gas bubbles in liquids," *Journal of the Acoustical Society of America*, vol. 61, pp. 17–27, 1977.

[44] R. Löstedt, B. P. Barber, and S. J. Putterman, "Toward a hydrodynamic theory of sonoluminescence," *Physics of Fluids A: Fluid Dynamics*, vol. 5, may 1993.

[45] H. Poritsky, "The collapse or growth of a spherical bubble or cavity in a viscous fluid," *Proceedings of the 1st U.S. National Congress of Applied Mechanics*, no. 813, 1952.

[46] E. Neppiras and B. E. Noltingk, "Cavitation produced by ultrasonics: Theoretical conditions for the onset of cavitation," *Proceedings of the Physical Society. Section B*, vol. 64, no. 12, 1951.

[47] B. E. Noltingk and E. A. Neppiras, "Cavitation produced by ultrasonics," *Proceedings of the Physical Society. Section B*, vol. 63, pp. 674–685, sep 1950.

[48] T. G. Leighton, *The Acoustic Bubble*. Academic Press, 1994.

[49] J. B. Keller and M. Miksis, "Bubble oscillations of large amplitude," *The Journal of the Acoustical Society of America*, vol. 68, no. 2, pp. 628–633, 1980.

[50] A. Prosperetti and A. Lezzi, "Bubble dynamics in a compressible liquid. part 1. first-order theory," *Journal of Fluid Mechanics*, vol. 168, p. 457–478, 1986.

[51] K. Yasui, "Effect of liquid temperature on sonoluminescence," *Phys. Rev. E*, vol. 64, p. 016310, Jun 2001.

[52] S. Fujikawa and T. Akamatsu, "Effects of the non-equilibrium condensation of vapour on the pressure wave produced by the collapse of a bubble in a liquid," *Journal of Fluid Mechanics*, vol. 97, no. 3, p. 481–512, 1980.

[53] F. R. Gilmore, "The growth or collapse of a spherical bubble in a viscous compressible liquid," *California Institute of Technology, Pasadena, CA*, vol. Report No. 26-4, p. 1–40, 1952.

[54] V. A. Akulichev, "Pulsations of cavitation voids," in *High-Intensity Ultrasonic Fields* (L. D. Rozenberg, ed.), p. 203–259, Plenum, New York, 1971.

[55] H. N. Oguz and A. Prosperetti, "The natural frequency of oscillation of gas bubbles in tubes," *The Journal of the Acoustical Society of America*, vol. 103, p. 3301, 1998.

[56] T. G. Leighton, "The inertial terms in equations of motion for bubbles in tubular vessels or between plates," *The Journal of the Acoustical Society of America*, vol. 130, p. 3333, 2011.

[57] Y. B. Zudin, "Analog of the rayleigh equation for the problem of bubble dynamics in a tube," *Moskow Power Engineering Institute*, vol. 63, pp. 28–31, 1992.

[58] A. R. Klotz and K. Hynynen, "Simulations of the devin and zudin modified rayleigh- plesset equations to model bubble dynamics in a tube," *Technical Acoustics/Tekhnicheskaya Akustika*, pp. 1–15, 2010.

[59] M. Tervo, *Numerical study of non-spherical bubble dynamics in a confined geometry.* Master thesis: Georg-August-University Göttingen, 2022.

[60] F. Reuter, S. Lesnik, K. Ayaz-Bustami, G. Brenner, and R. Mettin, "Bubble size measurements in different acoustic cavitation structures: Filaments, clusters, and the acoustically cavitated jet," *Ultrasonics Sonochemistry*, vol. 55, pp. 383–394, 2019.

[61] F. Blake, *The Tensile Strength of Liquids: A Review of the Literature.* Technical memorandum, Acoustics Research Laboratory, Department of Engineering Sciences and Applied Physics, Harvard University, 1949.

[62] S. Hilgenfeldt, M. P. Brenner, S. Grossmann, and D. Lohse, "Analysis of Rayleigh–Plesset dynamics for sonoluminescing bubbles," *Journal of Fluid Mechanics*, vol. 365, p. 171–204, 1998.

[63] W. Lauterborn and R. Mettin, "Nonlinear bubble dynamics – response curves and more," in *Sonochemistry and Sonoluminescence* (L. Crum, T. Mason, J. Reisse, and K. Suslick, eds.), pp. 63–72, Kluwer Academic Publishers, Dordrecht, 1999.

[64] H. M. H. Mitome, "Micro bubble and sonoluminescence," *Japanese Journal of Applied Physics*, vol. 40, p. 3484, may 2001.

[65] L. V. King, "On the acoustic radiation pressure on spheres," *Proceedings of the Royal Society of London. Series A - Mathematical and Physical Sciences*, vol. 147, no. 861, pp. 212–240, 1934.

[66] K. Yosioka and Y. Kawasima, "Acoustic radiation pressure on a compressible sphere," *Acustica*, vol. 5, no. 3, pp. 167–173, 1955.

[67] R. Mettin, "From a single bubble to bubble structures in acoustic cavitation," in *Oscillations, Waves and Interactions* (T. Kurz, U. Parlitz, and U. Kaatze, eds.), pp. 171–198, Universitätsverlag Göttingen, 2007.

[68] R. Mettin, I. Akhatov, U. Parlitz, C. D. Ohl, and W. Lauterborn, "Bjerknes forces between small cavitation bubbles in a strong acoustic field," *Phys. Rev. E*, vol. 56, pp. 2924–2931, Sep 1997.

[69] M. Korn, P. Machado Primo, and C. Santos de Sousa, "Influence of ultrasonic waves on phosphate determination by the molybdenum blue method," *Microchemical Journal*, vol. 73, no. 3, pp. 273–277, 2002.

[70] F. Priego-Capote and M. Luque de Castro, "Ultrasound-assisted continuous liquid–liquid extraction without phase separation and hydrolysis of paracetamol in suppositories," *Analytica Chimica Acta*, vol. 489, no. 2, pp. 223–232, 2003.

[71] Y. C. Fiamegos, C. G. Nanos, J. Vervoort, and C. D. Stalikas, "Analytical procedure for the in-vial derivatization—extraction of phenolic acids and flavonoids in methanolic and aqueous plant extracts followed by gas chromatography with mass-selective detection," *Journal of Chromatography A*, vol. 1041, no. 1, pp. 11–18, 2004.

[72] Q. Tu, J. Qian, and W. Frech, "Rapid determination of methylmercury in biological materials by gc-mip-aes or gc-icp-ms following simultaneous ultrasonic-assisted in situ ethylation and solvent extraction," *J. Anal. At. Spectrom.*, vol. 15, pp. 1583–1588, 2000.

[73] E. Priego-Lpezó and M. Luque de Castro, "Ultrasound-assisted extraction of nitropolycyclic aromatic hydrocarbons from soil prior to gas chromatography-mass detection," *Journal of Chromatography A*, vol. 1018, no. 1, pp. 1–6, 2003.

[74] K. S. Suslick and D. J. Flannigan, "Inside a collapsing bubble: sonoluminescence and the conditions during cavitation," *Annual Review of Physical Chemistry*, vol. 59, pp. 659–83, 2008.

[75] L. Hiremath, S. Nipun, O. Sruti, N. Kala, and B. Aishwarya, "Sonochemistry: Applications in biotechnology," in *Sonochemical Reactions* (S. Karakuş, ed.), ch. 5, Rijeka: IntechOpen, 2020.

[76] B. Savun-Hekimoğlu, "A review on sonochemistry and its environmental applications," *Acoustics*, vol. 2, no. 4, pp. 766–775, 2020.

[77] H. McMurray and B. P. Wilson, "Mechanistic and spatial study of ultrasonically induced luminol chemiluminescence," *Journal of Physical Chemistry A*, vol. 103, no. 20, pp. 3955–3962, 1999.

[78] C. Kalmár, T. Turányi, I. G. Zsély, M. Papp, and F. Hegedűs, "The importance of chemical mechanisms in sonochemical modelling," *Ultrasonics Sonochemistry*, vol. 83, p. 105925, 2022.

[79] J. Weiss, "Radiochemistry of aqueous solutions," *Nature*, no. 3894, pp. 748–750, 1944/06/01.

[80] A. Weissler, H. W. Cooper, and S. Snyder, "Chemical effect of ultrasonic waves: Oxidation of potassium iodide solution by carbon tetrachloride," *Journal of the American Chemical Society*, vol. 72, no. 4, pp. 1769–1775, 1950.

[81] E. J. Hart and A. Henglein, "Free radical and free atom reactions in the sonolysis of aqueous iodide and formate solutions," *Journal of Physical Chemistry*, vol. 89, pp. 4342–4347, 1985.

[82] N. Marinesco and J. Trillat, "Action des ultrasons sur les plaques photographiques," *C. R. Acad. Sci*, vol. 196, p. 858–861, 1933.

[83] H. Frenzel and H. Schultes, "Luminescenz im ultraschallbeschickten wasser," *Z. Phys. Chem. B.*, vol. 27, p. 421–427, 1935.

[84] M. S. Kyuichi Yasui, Toru Tuziuti and Y. Iida, "Sonoluminescence," *Applied Spectroscopy Reviews*, vol. 39, no. 3, pp. 399–436, 2004.

[85] S. Putterman, "Sonoluminescence: The star in a jar," *Physics World*, vol. 11, no. 5, pp. 38–42, 1998.

[86] J. Glanz, "The spell of sonoluminescence," *Science*, vol. 274, no. 5288, pp. 718–719, 1996.

[87] L. Crum and D. Gaitan, "Observation of sonoluminescence from a single stable cavitation bubble in a water/glycerine mixture," in *Frontiers of Nonlinear Acoustics, 12th ISNA* (M. F. Hamilton and D. T. Blackstock, eds.), (New York), pp. 459–463, Elsevier Applied Science, 1990.

[88] L. A. Crum, "Sonoluminescence," *Physics Today*, vol. 47, 1994.

[89] A. J. Walton and G. T. Reynolds, "Sonoluminescence," *Advances in Physics*, vol. 33, no. 6, pp. 595–660, 1984.

[90] E. Meyer and H. Kuttruff, "Zur phasenbeziehung zwischen Lumineszenz und Kavitationsvorgang bei periodischer Schallanregung," in *3rd International Congress on Acoustics (ICA)*, vol. 11, (Stuttgart), pp. 325–333, September 1-8 1959.

[91] K. Negishi, "Phase relation between sonoluminescence and cavitating bubbles," *Acoustica*, no. 10, p. 124, 1960.

[92] L. A. Chambers, "The emission of visible light from pure liquids during acoustic excitation," *Physical Review*, no. 49, p. 881, 1936.

[93] W. A. Weyl and E. C. Marboe, "Mechano chemistry of the dispersion of mercury in liquids in an ultrasonic field," *Journal of Applied Physics*, vol. 21, p. 937, 1950.

[94] T. K. Saksena and W. L. Nyborg, "Sonoluminescence from stable cavitation," *The Journal of Chemical Physics*, vol. 53, no. 5, pp. 1722–1734, 1970.

[95] P. Jarman, "Sonoluminescence: A discussion," *The Journal of the Acoustical Society of America*, vol. 32, no. 11, pp. 1459–1462, 1960.

[96] P. Lenard, "Über die Electricität der Wasserfälle," *Annalen der Physik*, vol. 282, no. 8, pp. 584–636, 1892.

[97] E. N. Harvey, "Sonoluminescence and sonic chemiluminescence," *Journal of the American Chemical Society*, vol. 61, no. 9, pp. 2392–2398, 1939.

[98] Y. I. Frenkel, "Electrical phenomena connected with cavitation caused by ultrasonic oscillations in a liquid," *Russ. J. Phys. Chem.*, vol. 14, pp. 305–308, 1940.

[99] G. L. Nathanson, "Value of electric field in cavities produced by ultrasonic cavitation in a liquid.," *Russ. J. Phys. Chem.*, vol. 55, pp. 154–158, 1981.

[100] M. Degrois and P. Baldo, "A new electrical hypothesis explaining sonoluminescence, chemical actions and other effects produced in gaseous cavitation," *Ultrasonics*, vol. 12, no. 1, pp. 25–28, 1974.

[101] C. M. Sehgal and R. E. Verrall, "A review of the electrical hypothesis of sonoluminescence," *Ultrasonics*, vol. 20, pp. 37–39, 1982.

[102] K. Suslick, S. Doktycz, and E. Flint, "On the origin of sonoluminescence and sonochemistry," *Ultrasonics*, vol. 28, no. 5, pp. 280–290, 1990.

[103] K. Livingtson, "Ultrasound: Its chemical, physical, and biological effects. kenneth s. suslick, ed. vch, new york, 1988 xiv," *Science*, vol. 243, no. 4897, pp. 1499–1499, 1989.

[104] M. Margulis, "Sonoluminescence and sonochemical reactions in cavitation fields. a review," *Ultrasonics*, vol. 23, no. 4, pp. 157–169, 1985.

[105] M. A. Margulis, "Investigation of electrical phenomena connected ith cavitation. ii. on theory of appearance of sonoluminescence and sonochemical reactions," *Russ. J. Phys. Chem.*, vol. 58, p. 1450, 1984.

[106] M. A. Margulis and I. M. Margulis, "Contemporary review on nature of sonoluminescence and sonochemical reactions," *Ultrasonics Sonochemistry*, vol. 9, no. 1, pp. 1–10, 2002.

[107] F. Lepoint-Mullie, D. D. Pauw, and T. Lepoint, "Analysis of the 'new electrical model' of sonoluminescence," *Ultrasonics Sonochemistry*, vol. 3, pp. 73–76, 1996.

[108] K. S. Suslick, "Sonochemistry," *Science*, vol. 247, no. 4949, pp. 1439–1445, 1990.

[109] C. C. Wu and P. H. Roberts, "Shock-wave propagation in a sonoluminescing gas bubble," *Phys. Rev. Lett.*, vol. 70, pp. 3424–3427, May 1993.

[110] B. P. Barber, R. Hiller, K. Arisaka, H. Fetterman, and S. Putterman, "Resolving the picosecond characteristics of synchronous sonoluminescence," *The Journal of the Acoustical Society of America*, vol. 91, pp. 3061–3063, 1998.

[111] B. Gompf, R. Günther, G. Nick, R. Pecha, and W. Eisenmenger, "Resolving sonoluminescence pulse width with time-correlated single photon counting," *Phys. Rev. Lett.*, vol. 79, pp. 1405–1408, Aug 1997.

[112] L. Frommhold, "Electron-atom bremsstrahlung and the sonoluminescence of rare gas bubbles," *Phys. Rev. E*, vol. 58, pp. 1899–1905, Aug 1998.

[113] B. P. Barber, R. A. Hiller, R. Löfstedt, S. J. Putterman, and K. R. Weninger, "Defining the unknowns of sonoluminescence," *Physics Reports*, vol. 281, no. 2, pp. 65–143, 1997.

[114] N. Xu, L. Wang, and X. Hu, "Numerical study of electronic impact and radiation in sonoluminescence," *Phys. Rev. E*, vol. 57, pp. 1615–1620, Feb 1998.

[115] W. C. Moss, D. B. Clarke, J. W. White, and D. A. Young, "Hydrodynamic simulations of bubble collapse and picosecond sonoluminescence," *Physics of Fluids*, vol. 6, no. 9, pp. 2979–2985, 1994.

[116] D. Hammer and L. Frommhold, "Sonoluminescence: How bubbles glow," *Journal of Modern Optics*, vol. 48, no. 2, pp. 239–277, 2001.

[117] F. R. Young, *Sonoluminescence / F. Ronald Young.* Boca Raton, FL: CRC Press, 2005 - 2005.

[118] V. Griffing, "The chemical effects of ultrasonics," *The Journal of Chemical Physics*, vol. 20, no. 6, pp. 939–942, 1952.

[119] L. A. Crum, "Measurements of the growth of air bubbles by rectified diffusion," *The Journal of the Acoustical Society of America*, vol. 68, no. 1, pp. 203–211, 1980.

[120] R. G. Holt and D. F. Gaitan, "Observation of stability boundaries in the parameter space of single bubble sonoluminescence," *Phys. Rev. Lett.*, vol. 77, pp. 3791–3794, Oct 1996.

[121] T. J. Matula, "Inertial cavitation and single-bubble sonoluminescence," *Philosophical Transactions: Mathematical, Physical and Engineering Sciences*, vol. 357, no. 1751, pp. 225–249, 1999.

[122] W. Lauterborn and C.-D. Ohl, "Cavitation bubble dynamics," *Ultrasonics Sonochemistry*, vol. 4, no. 2, pp. 65–75, 1997. Fifth Meeting of the European Society of Sonochemistry.

[123] B. P. Barber, C. C. Wu, R. Löfstedt, P. H. Roberts, and S. J. Putterman, "Sensitivity of sonoluminescence to experimental parameters," *Phys. Rev. Lett.*, vol. 72, pp. 1380–1383, Feb 1994.

[124] S. Hilgenfeldt, S. Grossmann, and D. Lohse, "A simple explanation of light emission in sonoluminescence," *Nature*, vol. 398, pp. 402–405, April 1999.

[125] R. Hiller, S. J. Putterman, and B. P. Barber, "Spectrum of synchronous picosecond sonoluminescence," *Phys. Rev. Lett.*, vol. 69, pp. 1182–1184, Aug 1992.

[126] K. Yasui, "Single-bubble and multibubble sonoluminescence," *Phys. Rev. Lett.*, vol. 83, pp. 4297–4300, Nov 1999.

[127] W. B. McNamara, Y. T. Didenko, and K. S. Suslick, "Sonoluminescence temperatures during multi-bubble cavitation," *Nature*, vol. 401, no. 6755, pp. 772–775, 1999.

[128] Y. T. Didenko, W. B. McNamara, and K. S. Suslick, "Molecular emission from single-bubble sonoluminescence," *Nature*, vol. 407, no. 6806, pp. 877–879, 2000.

[129] H. Xu, N. C. Eddingsaas, and K. S. Suslick, "Spatial separation of cavitating bubble populations: the nanodroplet injection model," *Journal of the American Chemical Society*, vol. 131, May 2009.

[130] N. Dezhkunov, A. Francescutto, P. Ciuti, T. Mason, G. Iernetti, and A. Kulak, "Enhancement of sonoluminescence emission from a multibubble cavitation zone," *Ultrasonics Sonochemistry*, vol. 7, no. 1, pp. 19–24, 2000.

[131] D. F. Gaitan, R. A. Tessien, R. A. Hiller, J. Gutierrez, C. Scott, H. Tardif, B. Callahan, T. J. Matula, L. A. Crum, R. G. Holt, C. C. Church, and J. L. Raymond, "Transient cavitation in high-quality-factor resonators at high static pressures," *The Journal of the Acoustical Society of America*, vol. 127, no. 6, pp. 3456–3465, 2010.

[132] F. R. Young, "Sonoluminescence from water containing dissolved gases," *The Journal of the Acoustical Society of America*, vol. 60, no. 1, pp. 100–104, 1976.

[133] T. Tuziuti, K. Yasui, T. Kozuka, A. Towata, and Y. Iida, "Enhancement of sonochemical reaction rate by addition of micrometer-sized air bubbles," *The Journal of Physical Chemistry A*, vol. 110, no. 37, pp. 10720–10724, 2006. PMID: 16970362.

[134] D. Meroni, R. Djellabi, M. Ashokkumar, C. L. Bianchi, and D. C. Boffito, "Sonoprocessing: From concepts to large-scale reactors," *Chemical Reviews*, vol. 122, no. 3, pp. 3219–3258, 2022. PMID: 34818504.

[135] L. M. Bryson, D. Fernandez Rivas, and C. Boutsioukis, "Cleaning of used rotary nickel-titanium files in an ultrasonic bath by locally intensified acoustic cavitation," *International Endodontic Journal*, vol. 51, no. 4, pp. 457–468, 2018.

[136] J. M. Costa and A. F. de Almeida Neto, "Ultrasound-assisted electrodeposition and synthesis of alloys and composite materials: A review," *Ultrasonics Sonochemistry*, vol. 68, p. 105193, 2020.

[137] P. R. Gogate, S. Mujumdar, and A. B. Pandit, "Sonochemical reactors for waste water treatment: comparison using formic acid degradation as a model reaction," *Advances in Environmental Research*, vol. 7, no. 2, pp. 283–299, 2003.

[138] J.-H. Lee, S. U. S. Choi, S. P. Jang, and S. Y. Lee, "Production of aqueous spherical gold nanoparticles using conventional ultrasonic bath," *Nanoscale Research Letters*, vol. 7, no. 420, 2012.

[139] Y. Tian, Z. Liu, X. Li, L. Zhang, R. Li, R. Jiang, and F. Dong, "The cavitation erosion of ultrasonic sonotrode during large-scale metallic casting: Experiment and simulation," *Ultrasonics Sonochemistry*, vol. 43, pp. 29–37, 2018.

[140] T. Rosett, "Cooling device for use with a sonic oscillator," *Applied Microbiology*, vol. 13, no. 2, pp. 254–256, 1965.

[141] C. A. Bizzi, R. C. Zanatta, D. Santos, K. Giacobe, R. M. Dallago, P. A. Mello, and E. M. Flores, "Ultrasound-assisted extraction of chromium from residual tanned leather: An innovative strategy for the reuse of waste in tanning industry," *Ultrasonics Sonochemistry*, vol. 64, p. 104682, 2020.

[142] L. S. Teixeira, H. P. Vieira, C. C. Windmöller, and C. C. Nascentes, "Fast determination of trace elements in organic fertilizers using a cup-horn reactor for

ultrasound-assisted extraction and fast sequential flame atomic absorption spectrometry," *Talanta*, vol. 119, pp. 232–239, 2014.

[143] U. Neis, "The use of power ultrasound for waste and biomass treatment," in *Applications of High-intensity Ultrasound* (A. Gallego-Juarez, Juan and K. F. Graff, eds.), ch. 32, UK: Woodhead Publishing, 2015.

[144] G. Cravotto, S. Di Carlo, M. Curini, V. Tumiatti, and C. Roggero, "A new flow reactor for the treatment of polluted water with microwave and ultrasound," *Journal of Chemical Technology & Biotechnology*, vol. 82, no. 2, pp. 205–208, 2007.

[145] A. I. Stankiewicz, "Energy matters: Alternative sources and forms of energy for intensification of chemical and biochemical processes," *Chemical Engineering Research & Design*, vol. 84, pp. 511–521, 2006.

[146] S. Freitas, G. Hielscher, H. P. Merkle, and B. Gander, "Continuous contact- and contamination-free ultrasonic emulsification—a useful tool for pharmaceutical development and production," *Ultrasonics Sonochemistry*, vol. 13, no. 1, pp. 76–85, 2006.

[147] J.-L. Dion, "Contamination-free high capacity converging waves sonoreactors for the chemical industry," *Ultrasonics Sonochemistry*, vol. 16, no. 2, pp. 212–220, 2009.

[148] P. R. Gogate, V. S. Sutkar, and A. B. Pandit, "Sonochemical reactors: Important design and scale up considerations with a special emphasis on heterogeneous systems," *Chemical Engineering Journal*, vol. 166, no. 3, pp. 1066–1082, 2011.

[149] Y. Cengel and J. Cimbala, *Fluid Mechanics: Fundamentals and Applications*. New York, NY10020: The McGraw-Hill Companies, Inc., 4 ed., 2018.

[150] H. Stone, A. Stroock, and A. Ajdari, "Engineering flows in small devices: Microfluidics toward a lab-on-a-chip," *Annual Review of Fluid Mechanics*, vol. 36, no. 1, pp. 381–411, 2004.

[151] A. Etminan, Y. S. Muzychka, and K. Pope, "A review on the hydrodynamics of taylor flow in microchannels: Experimental and computational studies," *Processes*, vol. 9, no. 5, 2021.

[152] M. T. Kreutzer, F. Kapteijn, J. A. Moulijn, and J. J. Heiszwolf, "Multiphase monolith reactors: Chemical reaction engineering of segmented flow in microchannels," *Chemical Engineering Science*, vol. 60, no. 22, pp. 5895–5916, 2005. 7th International Conference on Gas-Liquid and Gas-Liquid-Solid Reactor Engineering.

[153] R. Gupta, D. Fletcher, and B. Haynes, "Taylor flow in microchannels: A review of experimental and computational work," *The Journal of Computational Multiphase Flows*, vol. 2, no. 1, pp. 1–31, 2010.

[154] D. Tsaoulidis, V. Dore, P. Angeli, and N. V. P. anad K. R. Seddon, "Flow patterns and pressure drop of ionic liquid-water two-phase flows in microchannels," *International Journal of Multiphase Flow*, vol. 54, pp. 1–10, 2013.

[155] A. Ozcelik, D. Ahmed, Y. Xie, N. Nama, Z. Qu, A. A. Nawaz, and T. J. Huang, "An acoustofluidic micromixer via bubble inception and cavitation from microchannel sidewalls," *Analytical Chemistry*, vol. 86, no. 10, pp. 5083–5088, 2014. PMID: 24754496.

[156] T.-H. Wu, L. Gao, Y. Chen, K. Wei, and P.-Y. Chiou, "Pulsed laser triggered high speed microfluidic switch," *Applied Physics Letters*, vol. 93, no. 14, p. 144102, 2008.

[157] T.-H. Wu, Y. Chen, S.-Y. Park, J. Hong, T. Teslaa, J. F. Zhong, D. Di Carlo, M. A. Teitell, and P.-Y. Chiou, "Pulsed laser triggered high speed microfluidic fluorescence activated cell sorter," *Lab Chip*, vol. 12, pp. 1378–1383, 2012.

[158] R. Dijkink and C.-D. Ohl, "Laser-induced cavitation based micropump," *Lab Chip*, vol. 8, pp. 1676–1681, 2008.

[159] R. H. Liu, J. Yang, M. Z. Pindera, M. Athavale, and P. Grodzinski, "Bubble-induced acoustic micromixing," *Lab Chip*, vol. 2, pp. 151–157, 2002.

[160] A. N. Hellman, K. R. Rau, H. H. Yoon, S. Bae, J. F. Palmer, K. S. Phillips, N. L. Allbritton, and V. Venugopalan, "Laser-induced mixing in microfluidic channels," *Analytical Chemistry*, vol. 79, no. 12, pp. 4484–4492, 2007. PMID: 17508715.

[161] M. Riahi and E. Alizadeh, "Fabrication of a 3 d active mixer based on deformable fe-doped PDMS cones with magnetic actuation," *Journal of Micromechanics and Microengineering*, vol. 22, p. 115001, sep 2012.

[162] H. Y. Park, X. Qiu, E. Rhoades, J. Korlach, L. W. Kwok, W. R. Zipfel, W. W. Webb, and L. Pollack, "Achieving uniform mixing in a microfluidic device: Hydrodynamic focusing prior to mixing," *Analytical Chemistry*, vol. 78, no. 13, pp. 4465–4473, 2006.

[163] C. K. Harnett, J. Templeton, K. A. Dunphy-Guzman, Y. M. Senousy, and M. P. Kanouff, "Model based design of a microfluidic mixer driven by induced charge electroosmosis.," *Lab Chip*, vol. 8, no. 4, pp. 565–72, 2008.

[164] A. N. Hellman, K. R. Rau, H. H. Yoon, S. Bae, J. F. Palmer, K. S. Phillips, N. L. Allbritton, and V. Venugopalan, "Laser-induced mixing in microfluidic channels," *Analytical Chemistry*, vol. 79, no. 12, pp. 4484–4492, 2007.

[165] X. Zhu and E. S. Kim, "Microfluidic motion generation with acoustic waves," *Sensors and Actuators A: Physical*, vol. 66, no. 1, pp. 355–360, 1998.

[166] J. J. John, *Ultrasound assisted liquid-liquid extraction in microchannels*. PhD thesis, Katholieke Universiteit Leuven, 2017.

[167] J. J. John, S. Kuhn, L. Braeken, and T. Van Gerven, "Temperature controlled interval contact design for ultrasound assisted liquid–liquid extraction," *Chemical Engineering Research and Design*, vol. 125, pp. 146–155, 2017.

[168] O. Louisnard, "A simple model of ultrasound propagation in a cavitating liquid. part i: Theory, nonlinear attenuation and traveling wave generation," *Ultrasonics Sonochemistry*, vol. 19, pp. 56–65, jan 2012.

[169] B. E. Sarac, D. S. Stephens, J. Eisener, J. M. Rosselló, and R. Mettin, "Cavitation bubble dynamics and sonochemiluminescence activity inside sonicated submerged flow tubes," *Chemical Engineering and Processing*, vol. 150, p. 107872, 2020.

[170] T. Tuziuti, K. Yasui, Y. Iida, and A. Sivakumar, "Correlation in spatial intensity distribution between volumetric bubble oscillations and sonochemiluminescence in a multibubble system," *Research on Chemical Intermediates*, vol. 30, no. 7-8, pp. 755–762, 2004.

[171] R. Mettin, "Bubble structures in acoustic cavitation," in *Bubble and particle dynamics in acoustic fields: modern trends and applications* (A. A. Doinikov, ed.), Kerala: Research Signpost, 2005.

[172] T. Nowak and R. Mettin, "Unsteady translation and repetitive jetting of acoustic cavitation bubbles," *Phys Rev E Stat Nonlin Soft Matter Phys*, vol. 90, 2014.

[173] H. Mitome, "Relationship among sound field, bubble behavior and sonoluminescence," *Proc. World Congress on Ultrasonics 2003, 9*, 2003.

[174] S. ichi Hatanaka, K. Yasui, T. Tuziuti, T. Kozuka, and H. Mitome, "Quenching mechanism of multibubble sonoluminescence at excessive sound pressure," *Japanese Journal of Applied Physics*, vol. 40, p. 3856, may 2001.

[175] H. Mitome, "Micro bubble and sonoluminescence," *Japanese Journal of Applied Physics*, vol. 40, p. 3484, may 2001.

[176] K. Mc Carogher, Z. Dong, D. S. Stephens, M. E. Leblebici, R. Mettin, and S. Kuhn, "Acoustic resonance and atomization for gas-liquid systems in microreactors," *Ultrasonics Sonochemistry*, vol. 75, p. 105611, 2021.

[177] R. Mettin, C. Cairós, and A. Troia, "Sonochemistry and bubble dynamics," *Ultrasonics Sonochemistry*, vol. 25, pp. 24–30, 2015. Selected papers from the 14th Meeting of the European Society of Sonochemistry, Avignon, France, June 2014.

[178] M. M. van Iersel, N. E. Benes, and J. T. Keurentjes, "Importance of acoustic shielding in sonochemistry," *Ultrasonics Sonochemistry*, vol. 15, no. 4, pp. 294–300, 2008.

[179] S. ichi Hatanaka, K. Yasui, T. Tuziuti, and H. Mitome, "Difference in threshold between sono- and sonochemical luminescence," *Japanese Journal of Applied Physics*, vol. 39, p. 2962, may 2000.

[180] R. Mettin, J. Appel, D. Krefting, R. Geisler, P. Koch, and W. Lauterborn, "Bubble structures in acoustic cavitation: Observation and modeling of a "jellyfish"streamer," in *Special Issue of the Revista de Acustica*, vol. XXXIII, 2002.

[181] Y. T. Didenko, W. B. McNamara, and K. S. Suslick, "Effect of noble gases on sonoluminescence temperatures during multibubble cavitation," *Phys. Rev. Lett.*, vol. 84, pp. 777–780, Jan 2000.

[182] J. Gukenheimer and P. Holmes, *Nonlinear oscillations, dynamical systems, and bifurcations*, vol. 42 of *Applied mathematical sciences*. Springer, New York, 1982.

[183] A. Mahulkar, C. Riedel, P. Gogate, U. Neis, and A. Pandit, "Effect of dissolved gas on efficacy of sonochemical reactors for microbial cell disruption: Experimental and numerical analysis," *Ultrasonics Sonochemistry*, vol. 16, no. 5, pp. 635–643, 2009.

[184] J. Choi, H. Lee, and Y. Son, "Effects of gas sparging and mechanical mixing on sonochemical oxidation activity," *Ultrasonics Sonochemistry*, vol. 70, p. 105334, 2021.

[185] Y. Son, Y. No, and J. Kim, "Geometric and operational optimization of 20-khz probe-type sonoreactor for enhancing sonochemical activity," *Ultrasonics Sonochemistry*, vol. 65, p. 105065, 2020.

[186] O. Kapustina, "Degassing of liquids," in *Physical Principles of Ultrasonic Technology, Vol. I* (L. Rozenberg, ed.), pp. 377–509, Plenum Press, New York, 1973.

[187] D. S. Stephens, *Characterization and modeling of ultrasound propagation and cavitation in confined flow geometries*. PhD thesis, Georg-August-Universität Göttingen, expected 2023.

[188] J. T. Tervo, R. Mettin, and W. Lauterborn, "Bubble cluster dynamics in acoustic cavitation," *Acta Acustica united with Acustica*, vol. 92, pp. 178–180, 2006.

[189] R. J. Lang, "Ultrasonic atomization of liquids," *The Journal of the Acoustical Society of America*, vol. 34, no. 1, pp. 6–8, 1962.

[190] M. Kauer, V. Belova-Magri, C. Cairós, G. Linka, and R. Mettin, "High-speed imaging of ultrasound driven cavitation bubbles in blind and through holes," *Ultrasonics Sonochemistry*, vol. 48, pp. 39–50, 2018.

List of Figures

2.1 Sound wave [31] 8

2.2 Schematic image of acoustic cavitation process [34] 9

2.3 Bubble parameters 13

2.4 Transition to strong collapse oscillation around the Blake threshold (calculated with the Keller-Miksis model). Top: Bubble radius vs time curve for a bubble sinusoidally driven by 25 kHz, and with rest radius of 5 µm. The bubble oscillation remains nearly sinusoidal up to about 90 kPa. At 110 kPa, first collapse oscillations take place with a typical peak around the minimum radius. As the pressure increases to 130 kPa, the bubble expands up to nearly ten-fold of its rest size, and one very strong collapse follows (here at 22.5 µs). Such collapse profiles result in extreme heat and temperature conditions which facilitate chemical reactions (see Section 2.2). Bottom: Translation of the same bubble as it is driven by a plane travelling wave in +x direction. For lower driven pressures (90 and 110 kPa), the bubble merely moves back and forth with a small displacement in the direction of wave propagation. As the driving pressure is increased to 130 kPa, the bubble moves and jumps in +x direction during the collapse phase around 22.5 µs. The displacement is of the order of the fully expanded bubble size (R_{max}). 14

2.5 Radius vs time (normalized by the driving period) for two bubbles which are sinusoidally driven with a driving pressure amplitude of p_a=1.5 atm. One period of the oscillation is shown, and in the lower part, the net pressure (includig static pressure of 1 bar) is depicted. The bubbles have the equilibrium radii $R_0 = 0.85\,\mu m$ (dashed) and $R_0 = 0.90\,\mu m$ (solid). The smaller bubble oscillates only weakly, whereas the larger bubble expands to about tenfold equilibrium radius, and afterwards collapses strongly. . . 18

2.6 Bubble response curves: Normalized maximum expansion ratio $(R_{max} - R_n)/R_n$ vs bubble equilibrium radius (here named R_n, on logarithmic scale). The "jump" at the Blake threshold between about 1 and 2 μm is apparent. Images from [63]. 19

2.7 The compression ratio R_{min}/R_0 of the minimum radius as a function of P_a and R_0. For smaller R_0 and P_a, bubbles oscillate weakly, and for larger R_0 and P_a, bubbles undergo strong collapse. Retrieved from [62]. 20

2.8 Bubbles larger and smaller than their resonant sizes in standing wave field. Retrieved from [64]. 21

2.9 Bubbles smaller (left) and larger (right) than the resonant bubble size in a standing wave field during one oscillation cycle [64]. The arrows indicate direction and strength of the "momentary buoyancy" forces on the bubbles. By time averaging, the larger arrow "wins". 22

2.10 Primary Bjerknes force on bubbles in a standing wave of 20 kHz (left) and 1 MHz (right). The effect of the force is given in the plane of bubble equilibrium radius and driving pressure amplitude: white regions correspond to forces in direction of higher pressure amplitude (attractive antinodes), while dark regions indicate forces to lower amplitudes (repulsive antinodes). Figure from [67]. 23

2.11 Secondary Bjerknes forces between bubbles of different size for driving frequencies of 20 kHz (top) and 1 MHz (bottom); increasing pressures are indicated from left to right. The direction of forces is marked by the colour: white regions show attraction between bubbles, dark regions repulsion. Figure from [67]. 24

2.12 Possible mechanisms leading to excited metal atom emission from cavitation bubble: **a)** The heated shell model **b)** The injected droplet model . . 31

2.13 Ultrasonic transducers are attached to **a)** the bottom walls, and **b)** both bottom and side walls. **c)** Lab-scale ultrasound bath. (source: [134]) . . . 34

2.14 Ultrasonic transducers are attached to **a, b, c)** different possible positioning of immersed transducers, **d)** stack of transducers, **e)** large scale industrial bath with immersed ultrasound transducers on side walls (source: [134]) 35

2.15 **a)** A simple schematic of a cup-horn based batch reactor with direct and indirect sonication, **b)** Indirect cup-horn sonotrode reactor with multiple sample vessels 35

2.16 A simple schematic of emission walls **a**) without cooling system, **b**) with cooling system. **c**) A diagram of cross-sectional, cylindrical and hexagonal tubular emission walls **d**) Design of a flow reactor with emitting walls with 6 transducers (BANDELIN Electronic GmbH & Co. KG, Berlin, Germany) **e**) Hexagonal tubular emitting walls with 5 transducers in each surface with an adjustable frequencies of 20 kHz and 40 kHz (KLN Ultraschall AG, Germany). 36

2.17 Industrial continuous sonoreactors employed with sonotrode: **a**) Continuous sonoreactor with a single sonotrode in a closed system (Hielscher Ultrasonics GmbH), **b**) Industrial continous reactor employed with 7 identical sonotrodes, which can provide power between 1000 and 16000 W for waste-solid water treatment., **c**,d) Schematic drawing and the image of full scale continous sonoreactor (ULTRAWAVES Water and Environmental Technologies, Hamburg, Germany). [134] 38

2.18 Industrial continuous micro-sonoreactors employed with different type of transducers: **a**) An ultrasonic flow cell and it's schematic drawing on the right, **b**) Cross-section and the core/reaction chamber of SonerTec sonoreactor, **c**) Reaction channels on top of an ultrasonic transducer for liquid-liquid extraction. [134] 39

2.19 Development of velocity boundary layer in a circular pipe. The average velocity for laminar flow exhibits a parabolic profile [149]. 41

2.20 The schematic of GL flow regimes in the vertical channels. **a,b)** bubbly flow, **c,d)** Taylor, or segmented flow **e)** transitional flow slug to churn **f)** churn flow **g)** annular-film flow **h)** mist-annular, or wispy- annular flow. Retrieved from [152] 43

2.21 Working principle of micropumping via a single bubble. A configuration consists of a single bubble in a microfluidic chamber *below* and a channel *on top* where the liquid is pushed into. The frames captured during pumping are given on top, and the corresponding sketches are depicted below. The arrows show the velocity vectors of the flow field. From the first to the last frame, respectively: Inception of a bubble, bubble expansion, bubble at maximum radius, jet formation, vanishing of the bubble [158]. 44

3.1 **a)** Cross-sectional configuration of PFA channels with an inner diameter of d_i=1/16" (∼0.8mm). **b)** Photograph from the top view of the reactor plate showing the slug flow of liquid and air. 48

3.2 Schematic representation and photo of the experimental setup for the direct contact reactor. Liquid-air segmented flow is formed by alternating pumping in the channels. Sonication is performed at different frequencies ranging from 25 kHz to 52 kHz. The channels are illuminated by an intense light source to collect the reflected light from the aluminum plate on which the channels are placed. Visualization of bubbles inside the channels is achieved using a high-speed camera with a long-distance microscope. . . . 49

3.3 Schematic drawing of the loop channels submerged into ultrasonic bath. The PFA channels are filled with alternating air and luminol solution using pumps, and the flow is then stopped. The ultrasonic transducer is driven at a frequency of 27.2 kHz. The cavitation bubbles inside the tubes are recorded using a high-speed camera with a long-distance microscope attachment, while the luminescence emission is captured by a digital SLR camera. 50

3.4 Schematic drawing of channels submerged into ultrasonic bath via polycarbonate holder. The U-shaped polycarbonate holder is submerged into the bath in an inverted position, with its open end facing downwards, along the center of the transducer. The transducer is operated at a frequency of 25.7 kHz. A high-speed camera equipped with a long-distance microscope is used to record the cavitation bubbles inside the channels, while a digital SLR camera is employed to capture the luminescence emission. 51

3.5 Stacked channels configuration. PFA tubing is arranged horizontally in lines using a polycarbonate holder with holes on each side. The stacked channels are positioned in the ultrasonic bath along the center of the transducer surface. The bath is filled with degassed water up to a height of 11 cm. The channels directly face the bottom of the bath without any medium in between. 52

3.6 Testing the SCL intensity. A glass cuvette with the dimensions of 30 x 30 x 70 mm^3 is submerged into an ultrasonic bath. The cuvette is filled with an aqueous luminol solution. 53

3.7 SCL emission from a glass cuvette filled with 0.1 mM luminol solution at different pH values.**a)** pH=12.2, **b)** pH=11.4. **c)** Enhancement of SCL intensity by Ar gas. Images obtained in dark room conditions with a 30-second exposure time using an SLR camera. The water-filled ultrasonic bath is sonicated at 25.7 kHz with an applied power of ∼80 W. 53

3.8 The configuration of closed system for **a)**degassing, and **b)** Ar-gassing . . 54

4.1 **a)** Image of the water-air flow through channel obtained in silent condition. The image is extracted from a 50 fps recording. The inner diameter of the channel is 0.8 mm and the flow rate is $\sim 7\,\mu$L/s in the direction from right to left. The round illuminated area on the background is the reflected light from the surface of the aluminium plate underneath. The water slug is seen as a white rectangle in the middle of the tube. Black regions on each side of the water slug refers to the air pockets. The channel thickness (0.8 mm, same as inner diameter) can also be distinguished around the boundary between water and air pocket. **b)** The image of the water slug extracted from a 100k fps in order to observe the cavitation activity inside the channel during sonication at 13 kHz, and the function generator is driven at amplitude of 270 mV. No cavitation is detected. . . 56

4.2 Images of cavitation activity inside channels sonicated at different frequencies. Images obtained with a high-speed camera at 100k fps. Rate of water-air slug flow is $\sim 7\,\mu$L/s towards to the left. The transducer is driven at **a,b)** 25 kHz, with 270 mV; **c,d)** 36 kHz, with 360 mV; **e,f)** 48 kHz, with 580 mV; **g, h,i)** 52 kHz, with 580 mV 57

4.3 Interface between water (left) and air (right) slugs, obtained at a frequency of 52 kHz with the electrical input of 580 mV. The capillary waves and droplet/bubble ejection at the two-phase boundary seem to play a crucial role for the cavitation bubble seeding in the liquid. A higher number of ejected water droplets into the gas (arrows) were observed at higher frequencies, in correlation to higher cavitation bubble numbers at the higher frequencies. 58

4.4 Deformation in PFA tubing and polycarbonate top cover caused by overheating of aluminum plate. 58

4.5 Mini-ultrasonic-bath reactor assembly and a top-view of reactor [166] . . . 59

4.6 Oscillating bubble cluster in water slug and ejected water droplets in air gap. The yellow arrow show the bubble luster in the channel, while the red arrows point the droplet ejection. Consecutive frames are obtained by recording with 100k fps and an exposure time of 10 μs. The frame height is approximately the same with the channel diameter which is 0.8 mm. The transducer is operated at 40 kHz with a delivered power of 19 W (the difference between the forward and reflected power). The water-air slug flow rate is about 9 μL/s and flow direction is from left to right. 60

4.7 **a)** Measured pressure amplitude in the central plane above the transducer which is at the bottom right. The hydrophone-scanned rectangular area is positioned on the background of the numerical mapped sound field. **b)** Colour codded sound pressure amplitude on the central, vertical plane above the transducer (calculated with Comsol applying Louisnard's model [168] with a gas void fraction of $\beta = 4.10^{-7}$ and a radiated power of 65 W). The colour code for the corresponding pressure values of both images are identical. For a better contrast, the value of the pressure is limited by 2.5 bar, and the higher pressure areas (right above the transducer) appear in white colour. **c)** SCL emission of sonicated aqueous 0.1 mM luminol solution (filling height of the bath 6 cm; exposure time 30 seconds; 27.2 kHz, 65 W.) 63

4.8 **a)** Daylight image of the loops in the ultrasonic bath filled with water. The white horizontal line over the loops is the water level in the bath, the spikes at the bottom of the cuvette are the screws joining the polycarbonate walls and aluminum bottom plate of the bath. **b)** SCL emission from luminol-air slugs along tube (27.2 kHz, 65 W, water height 6 cm, exposure time 30 s). **c, d)** Two different emission recordings of luminescence from the loops, overlaid to the measured sound field (units see colour coding bar). The arrow shows the approximate position of the channels in which high speed recordings of Fig. 4.9 have been obtained from. 64

4.9 Different cavitation bubble structures in the tube, at the nearly collapse phase and subsequent phase of maximum expansion. Recorded with 20k fps, exposure time of 50μ s. Frame height is approximately 1.5 mm from a to k, and 0.8 mm for l and m. **a, b)** Wall-attached cluster, **c, d)** Narrow plug, **e, f)** Wider plug, **g, h)** Streamer, **i, k)** Disperse, **l, m)** Displacement and jetting of bubbles. 66

4.10 A single bubble at the edge of a "plug structured" cluster in a flow tube exhibits nearly stationary dynamics. **Top:** A sequence of 24 frames of a bubble corresponding to 6 driving periods from left to right in the direction of the arrow. Recording is at 100k fps, exposure time is 10 μs, and the frame width is 192 μm. **Bottom:** Reconstructed bubble radius-time curves. The experimental bubble radius is given with error bars and back-folded onto a single acoustic period $T = 1/f$. Different colors of lines represent different cases of the bubble dynamics model as mentioned in the text. The best fit is given as a thick black line, obtained for the pressure amplitude of p_a=2 bar, with $R_0 = 0.7\,\mu$m and L=16 cm. 68

4.11 **a)** The measured sound field map with the color-coded pressure amplitude. The map is observed as a rectangular pattern on the background of the numerical simulation according to the exact measurement coordinates. The transducer is operated at 25.7 kHz. The applied voltage is maintained at an electrical power of 10 mV during mapping. **b)** Numerical simulation of the sound field inside the ultrasonic bath. The void fraction is $\beta = 5.10^{-6}$, with monodisperse nuclei of equilibrium size $R_0 = 5\,\mu$m. 70

4.12 Ar-gassed luminol filled container is sonicated at 25.7 kHz with varying electrical power input. Each column refers to set of images captured with a digital SLR camera, with the exposure time of 30 s. Each row corresponds to different function generator amplitudes from 500 mV to 100 mV with the steps of 50 mV (from **i)** to **ix)** ; corresponding to the delivered electrical power (the difference between forward and reflected power) of approximately 93, 84, 75, 62, 48, 33, 24, 13, and 5 W. Since the exposure time is 30 s, each column is recorded in 4.5 minutes, and performed one after another consecutively as column **a)**, **b)** and **c)**. . . . 75

4.13 SCL signals obtained from a luminol-filled ultrasonic bath for three different power inputs. The bath is filled up to 11 cm, and the transducer is operated at 25.7 kHz with the electrical power of (the difference between forward and reflected power) **a)** 75,W, **b)** 62 W, and **c)** 5 W. Luminescence emissions are captured with a digital SLR camera with an exposure time of 30 s. **d)** The sound pressure map obtained via a hydrophone (Figure 4.12.a) is superimposed onto the luminescence emission image captured with a power input of 62 W. The numerically simulated pressure map (Figure 4.12.b) is overlaid onto the **e)** SCL image captured with an electrical power 62 W and **f)** 5 W. 76

4.14 Photo of stacked channels before sonication. PFA tubing is placed horizontally as lines by a polycarbonate holder which has holes on each side. The stacked channels are placed into an ultrasonic bath along the center of the transducer surface and the bath is filled with water up to 11 cm. Channels directly face the bottom of the bath without any medium in between, and the polycarbonate holder does not have any contact with the bottom plate of the bath. Channels are filled with a luminol-air slug flow, with about the same volume ratio of both phases. Dark and bright pockets in channels correspond to luminol pockets and air gaps, respectively. 77

4.15 SCL from luminol-air-filled channels submerged into an ultrasonic bath filled with water up to a height of 11 cm. SCL images are obtained in dark conditions. After merging all images into a single figure, overall brightness/contrast is adjusted in order to distinguish the differences between each image. Luminol and air slugs are formed, then the pumps are stopped. Luminescence emissions are recorded with an exposure time of 30 s. Channels are sonicated at 27.5 kHz with different amplitudes. From **a)** to **i)**, the applied electrical amplitude changes from 500 mV to 100 mV with a decrease of 50 mV, respectively. Corresponding applied power (the difference between forward and reflected power) is about 93, 84, 75, 62, 48, 33, 24, 13, and 5 W. 78

4.16 Cutline through SCL images obtained from a luminol-filled bath, luminol-air slug-filled channels, and a sound pressure map. The red line indicates the exact position of the cutline. The images are captured via an SLR camera with an exposure time of 30 s. **a)** The bath is filled up to 11 cm with a luminol solution and sonicated at 25.7 kHz with an electrical amplitude of 350 mV. **b)** The channels are filled with a luminol-air slug flow and submerged in an ultrasonic bath filled with 11 cm of water. The transducer is driven at 25.7 kHz with 500 mV. **c)** A simulated sound pressure map for the ultrasonic bath filled up to 11 cm (see Fig. 4.11). **d, e)** Changes in RGB intensity above the transducer obtained from the SCL image given in a) and b), respectively. **f)** Acoustic pressure above the transducer obtained from the simulated map in c). 82

4.17 Consecutive image series of bubbles oscillating inside and outside the channel. The frame rate of the recording is 300k fps. The transducer is driven at 25.7 kHz with 500 mV. The channel diameter is 0.8 mm, the flow rate is approximately 10 μL/s (towards the right). The bubble cluster in the upper part of the channel is oscillating inside, whereas the bubbles in the lower part of the channel are outside ones. Each row corresponds to one driving period. Strong acoustic pressure excitation leads to nonlinear oscillations of bubbles inside and outside the channel, exhibiting period doubling sequences [182]. 83

4.18 Plain high-speed image series of the tube under cavitation conditions. The image sequence starts from the top left and progresses towards the right, row by row. The recording is done at 100k fps, with an exposure time of 1 μs. Both cavitation bubbles inside a water slug in the channel, and bubbles outside in the water-filled ultrasonic bath are visible. The outside water has been distilled and degassed, but still cavitation occurs. The water-air slug flow in the tube runs at about 10 μL/s, which corresponds to a flow speed of about 20 mm/s. The frame height is about 1 mm, the inner diameter of the channel is 0.8 mm. The transducer is driven at 25.7 kHz with an electrical amplitude of 500 mV. The air-water interface is visible on the left in the lower image. 84

4.19 Grey scale analysis to compare oscillations of cavitation bubbles inside the channel and in the coupling liquid. On top, the last frame of Fig. 4.18 is presented, showing black and red identical rectangles (area of 300x240 pixels) representing the data collection regions. The red frame corresponds to the red data point in the graphs, indicating the mean brightness/contrast values from both the bubble cluster inside the channel and in the coupling liquid. On the other hand, the black frame corresponds to the black data points in the plots, where the brightness/contrast values primarily come from bubbles outside the channel. The upper graph displays the mean grey scale plot from both areas for 16 consecutive frames, while the lower graph shows the same analysis for 64 consecutive frames. The time interval between two data points is 10 μs. 86

4.20 Several (39) frames from Fig. 4.18 sorted in an ascending relative phase to the acoustic driving phase over one acoustic period T. The expansion and collapse of the cluster inside the tube can be observed with apparent higher time resolution. Since the bubble dynamics and positions are not fully periodic, the sequence exhibits some "jumps". 87

4.21 Grey levels of the indicated regions from Fig. 4.19, now resorted modulo $2T$ = two driving periods. A roughly coherent expansion-collapse oscillation can now be perceived for bubbles outside (green) and inside (blue) the channel. 88

4.22 Three frames from Fig. 4.18 with nearly one driving period temporal distance (numbers 28, 32 and 36), top row. Inside bubbles in the cluster are in the expanded oscillation phase. The correlation between the images is analyzed by pixel-wise addition (with saturation) of the grey levels of two of the frames, respectively, shown in the middle rows. Dark regions correspond to bubbles at nearly the same positions in both frames. Thus the darker the cluster parts appear, the higher the one-to-one spatial correlation of individual bubbles in the cluster. The correlation is only moderate for a temporal distance of T (28+32 and 32+36), and it seems to decrease further for a temporal distance of $2T$ (28+36). The bottom rows show details in a region of lower correlation (red, brighter zone in the additive pictures) and higher correlation (violet, darker region in the additive pictures). 89

4.23 **Top:** Consecutive image series showing a wall-attached cluster aggregating at the bottom of the tube and less confined dispersed bubble structures in a water-air slug flow. **Bottom:** Droplet ejection at the water-air boundary and a wall-attached bubble cluster. [Channel diameter: 0.8 mm, water-air slug flow rate: approximately 10 μL/s (towards the right), transducer frequency: 25.7 kHz, electrical amplitude: 300 mV (corresponding to a delivered power of approximately 48 W), recording frame rate: 25.7k fps, exposure time: 1 μs.] 91

4.24 **Top:** Consecutive image series showing wall-attached bubble clusters of various sizes and streamers. **Bottom:** Bulge formation and droplet ejection at the water-air interface. Strong surface oscillations are observed at the free interface of the water-air boundary. A high number and volume of water droplets are ejected into the air gap. [Channel diameter: 0.8 mm, water-air slug flow rate: approximately 10 μL/s (towards the right), transducer frequency: 25.7 kHz, electrical amplitude: 400 mV (corresponding to a delivered power of approximately 75 W), recording frame rate: 25.7k fps, exposure time: 1 μs.] 92

4.25 **Top:** Consecutive image series showing streamers that agglomerate at the channel wall. **Bottom:** Seeding of a large bubble from the water-air interface. Strong surface oscillations are observed at the free interface of the water-air boundary. The seeded large bubble moves towards the wall-attached bubble cluster. [Channel diameter: 0.8 mm, water-air slug flow rate: approximately 10 μL/s (towards the right), transducer frequency: 25.7 kHz, electrical amplitude: 500 mV (corresponding to a delivered power of approximately 93 W), recording frame rate: 25.7k fps, exposure time: 1 μs.] 93

4.26 A bubble plug comprising of a roughly rectangular bubble field stretching from top to bottom. The first frame is the one at top left, and the sequential frames are followed row by row. One of the ends acts as a boundary between the bubble-free region and the bubble field. [Channel diameter: 0.8 mm, water-air slug flow rate: approximately 10 μL/s (towards the right), transducer frequency: 25.7 kHz, electrical amplitude: 400 mV (corresponding to a delivered power of approximately 93 W), recording frame rate: 25.7k fps, exposure time: 1 μs.] 94

4.27 Bubble nucleation at the free interface of a liquid-air slug. The upper images depict a bubble entering the liquid slug and multiplying itself frame by frame. The lower image shows the bubble cluster formed at a later stage. The frames were recorded at 25.7k fps, with an exposure time of 1 μs, and a frame height of 1 μs. 96

4.28 Droplet ejection occurs at the center of the free interface of a liquid-air slug. Frames are presented by rotating the images 90 degrees clockwise compared to Fig. 4.27; in this representation, water is located at the bottom, and the air is at the top. The recording was done at 150k fps, with a frame width of about 200 μm, and an exposure time of 2 μs. A bulge forms from a peak of a capillary wave, which then disintegrates into the gas slug as a droplet. After the third frame, a newly formed bubble, appearing as a dark spot in the liquid at the bottom, oscillates under the influence of ultrasonic irradiation. 97

4.29 Droplet ejection events occur at the free interface of a water-air slug. The ejection of water droplets is pointed out via red arrows and yellow arrows show water droplets. Each column represents consecutive frames from a recording performed at 100k fps, with exposure time of 1 μs. The tube diameter is 0.8 mm. The channels are filled with water-air slugs, and then the flow is stopped. The sonication is performed at 25.7 kHz with an applied electrical power of approximately 60 W (the difference between delivered and reflected power). In each frame, the liquid is on the left (white) and the air gap is on the right side (black). The total time of sonication is 0.4055 s. From left to right, the columns depict the consecutive frames extracted from the recording 0.00051, 0.00681, 0.21014, and 0.34171 s after the start of sonication, respectively. 99

Acknowledgements

First and foremost, I would like to express my sincere gratitude to my supervisor Dr. Robert Mettin for his guidance and support throughout my Ph.D. study and in writing this thesis. Apart from his extensive knowledge and remarkable expertise in the field, I very much appreciate his sense of humor, which lightens the academic atmosphere and fosters a positive and enjoyable working relationship.

I would like to acknowledge the funding received from the EU Horizon 2020 Research and Innovation Programme under the Marie Skłodowska-Curie grant agreement No 721290. I am truly fortunate to have had the opportunity to work on the COSMIC project and I sincerely thank each and every member of the team for all the joyful moments we had in different countries. I appreciate the valuable insights and perspective of each supervisor during our network wide meetings which have greatly enriched my research. I also would like to thank Prof. Dr. Tom Van Gerven from KU Leuven, Prof. Dr. Asterios Gavriilidis from University College London, and Dr. Thomas Dreyer from Weber Ultrasonic AG for hosting me as a visiting researcher and sharing their knowledge and expertise. In this context, I would also like to thank each member of their research groups for the friendships we made and the joyful moments we had during my visits. I also appreciate the support of Dr. Jinu J. John from KU Leuven for sharing his knowledge in flow-reactor design.

My heartfelt appreciation first goes to Prof. Dr. Werner Lauterborn, and then to the other "bubble" people Dwayne Stephens, Julian Eisener, Max Shir, Atiyeh Aghelmaleki, Matti Tervo, Juan Rosselló, Ferenc Hegedűs, and Fabian Reuter. I also appreciate Dr. Kevin Lüdemann's assistance. I would like to thank our secretaries Nicole Rehbein, Ursula Hahn-Wörgöter, and especially Regina Wunderlich for her friendship and support. I am very thankful for the great technical support of Dieter Hille and the team in workshop, and IT support of Thomas Geiling.

To all my friends, I would like to thank you for not leaving me alone in the roller-coaster of my Ph.D. journey. To the ones I got to know in Göttingen, thank you for the laughter, encouragement, and shared moments of joy that we have experienced together. From those friends, I deeply thank Dr. Emir Öngüner, and Oğuzhan Kızmaz, LL.M. who massively supported me while writing my thesis. I would like to thank my close friends back home in Ankara; Dr. Kerem Çağatay İçli, Burcu Taş and Berk Akbay.

My special thanks go to Johan Ekstrand and my second close family in Sweden. Tack för allt ert stöd under min doktorand och för att ni fått mig att känna mig som hemma trots att jag har varit så långt hemifrån.

My enormous thanks go to my parents for their continuous support and encouragement throughout all my studies. Eğitim hayatım boyunca gösterdiğiniz her türlü destek

için, ve her şartta her zaman yanımda olduğunuz için sonsuz teşekkür ederim. Ve son olarak, Modern Türkiye'nin kurucusu Mustafa Kemal Atatürk'e, bağımsız ve özgür bir bilim kadını olarak eğitim görme ve yurtdışında doktora yapma imkanı sağladığı için şükranlarımı sunuyorum.